The Effect of Star-Planet Interactions on Planetary Climate

Aomawa L. Shields

A dissertation submitted in partial fulfillment of the
requirements for the degree of

Doctor of Philosophy

University of Washington

2014

Reading Committee:

Victoria Meadows, Chair

Cecilia Bitz

Rory Barnes

Program Authorized to Offer Degree:
Astronomy

University of Washington

Abstract

The Effect of Star-Planet Interactions on Planetary Climate

Aomawa L. Shields

Chair of the Supervisory Committee:
Professor Victoria Meadows
Astronomy

The goal of the work presented here is to explore the unique interactions between a host star, an orbiting planet, and additional planets in a stellar system, and to develop and test methods that include both radiative and gravitational effects on planetary climate and habitability. These methods can then be used to identify and assess the possible climates of potentially habitable planets in observed planetary systems.

In this work I explored key star-planet interactions using a hierarchy of models, which I modified to incorporate the spectrum of stars of different spectral types. Using a 1-D energy-balance climate model, a 1-D line-by-line, radiative-transfer model, and a 3-D general circulation model, I simulated planets covered by ocean, land, and water ice of varying grain size, with incident radiation from stars of different spectral types. I find that terrestrial planets orbiting stars with higher near-UV radiation exhibit a stronger ice-albedo feedback. Ice extent is much greater on a planet orbiting an F-dwarf star than on a planet orbiting a G-dwarf star at an equivalent flux distance, and ice-covered conditions occur on an F-dwarf planet with only a 2% reduction in instellation (incident stellar radiation) relative to the present instellation on Earth, assuming fixed CO_2 (present atmospheric level on Earth). A similar planet orbiting the Sun at an equivalent flux distance requires an 8% reduction in instellation, while a planet orbiting an M-dwarf star requires an additional 19% reduction in instellation to become ice-covered, equivalent to 73% of the modern solar constant. The reduction in instellation must be larger for planets orbiting cooler stars due in large part to the stronger absorption of longer-wavelength radiation by icy surfaces on these planets, in addition to stronger absorption by water vapor, CO_2, and clouds in their atmospheres,

providing increased downwelling longwave radiation. The surface ice-albedo feedback effect becomes less important at the outer edge of the habitable zone, where atmospheric CO_2 can be expected to be high. I show that ∼3-10 bars of CO_2 will entirely mask the climatic effect of ice and snow, leaving the traditional outer limit of the habitable zone unaffected by the spectral dependence of water ice and snow albedo.

Simulations of the equilibrium climate response of a planet to increasing instellation from an F-, G-, or M-dwarf star indicate that the exit out of global ice cover is also sensitive to host star spectral energy distribution. Under fixed CO_2 conditions, a planet orbiting an M-dwarf star exhibits a smaller resistance to melting out of a frozen state, requiring a smaller instellation to initiate deglaciation than planets orbiting hotter, brighter stars. This is due to the combined effects of surface ice and snow absorption of the large fraction of near-IR radiation emitted by M-dwarfs, and atmospheric near-IR absorption, which weakens the Hadley circulation, reducing the climate hysteresis (the range over which multiple stable equilibia are possible) of M-dwarf planets. Given their greater climatic stability, planets orbiting cooler, lower-mass stars may be the best candidates for long-term habitability and life beyond the Solar System.

As lower-mass stars are likely candidates to host multiple rocky planets, it is important to consider whether gravitational interactions among planets may have significant effects on climate and habitability over long timescales. Using an n-body integrator with inputs from a method I developed to determine the locations of all planets in a given system at the same epoch using transit timing data, a specific case is explored—that of Kepler-62f (Borucki et al. 2013), a potentially habitable planet in a five-planet system orbiting a K-dwarf star. The maximum stable initial eccentricity possible for Kepler-62f is identified as $e = 0.32$. Simulations using a 3-D GCM indicate that Kepler-62f would have areas of the planet with surface temperatures above the freezing point of water with 1 bar or more of CO_2 in its atmosphere. If it has an active carbon cycle, Kepler-62f could have ample amounts of greenhouse gases in its atmosphere to maintain atmospheric stability and habitable surface conditions while staying well below the maximum CO_2 greenhouse limit. In a low-CO_2 case (Earth-like levels), increases in planetary obliquity and orbital eccentricity coupled with an orbital configuration that places the summer solstice at or near pericenter generate regions

of the planet with above-freezing surface temperatures, which may cause surface melting of an ice sheet formed during an annual cycle. If Kepler-62f is synchronously rotating and has an ocean, significant cloud cover could develop at the substellar point, increasing planetary albedo and reducing surface temperatures. The methods presented here serve as tested tools that can be used to assess the possible climates of potentially habitable planets in systems with a wide range of orbital architectures as they are discovered.

TABLE OF CONTENTS

Page

LIST OF FIGURES

LIST OF TABLES

ACKNOWLEDGMENTS

This dissertation and all that has led to its completion would not have been possible without the University of Washington Astronomy Department, particularly its 2009 graduate student admissions committee, and its graduate student body, which has been more supportive and generous than I ever could have imagined. I have been fortunate to have had an incredible advisor in Victoria Meadows, whose time, encouragement, support, professional mentorship and critical eye (this will be a paragraph-long sentence, because she knows I love those and will surely catch it) have been invaluable, and crucial to my success in graduate school. I am also grateful to my co-advisor Cecilia Bitz, for teaching me how to use climate models, for her patience as I learned and asked all manner of questions (and still do), and for the ease with which she welcomed an astronomer with predilections towards icy exoplanets into her climate and sea ice research group. Thank you as well to the rest of my committee–Rory Barnes, Raymond Pierrehumbert, Suzanne Hawley, and Valerie Curtis-Newton, for their time and counsel, and for their support of my research interests. I am also grateful for my wonderful officemates Yusra AlSayyad and Amit Misra, who struck the perfect balance of respectful quiet, humorous conversation, and emotional and mental support. Thanks as well to Eric Agol, Dave Crisp, Tyler Robinson, and Benjamin Charnay for their generosity of time and teaching.

This material is based upon work supported by the National Science Foundation (NSF) Graduate Research Fellowship Program under Grant Nos. DGE-0718124 and DGE-1256082, and I am grateful to NSF for its investment in and continued commitment to my career. This work was also performed as part of the NASA Astrobiology Institute's Virtual Planetary Laboratory Lead Team, supported by the National Aeronautics and Space Administration through the NASA Astrobiology Institute under Cooperative Agreement solicitation NNH05ZDA001C. Computer modeling work was done on the Challenger computer cluster at the University of Washington, and was also facilitated through the use of advanced com-

putational, storage, and networking infrastructure provided by the Hyak supercomputer system at the University of Washington, and made use of the Yellowstone high-performance computer cluster. I would like to acknowledge Marc Michelsen for Challenger computing support, Pramod Gupta for Hyak computing support, and high-performance computing support from Yellowstone (ark:/85065/d7wd3xhc) provided by NCAR's Computational and Information Systems Laboratory, sponsored by the National Science Foundation.

I am forever grateful for: Dr. Michael Kane and his process group for graduate women of color, of which I was privileged to be a part from 2009 to 2012; the Minorities Striving and Pursuing Higher Degrees of Success in Earth System Science (MS PHD'S) program, for its mentorship and consistent support; the June 2014 dissertation writing retreat facilitated by the UW Odegaard Writing and Research Center, which contributed highly to the completion of my dissertation. Additional thanks to those who walked this path before me and helped me to follow in their footsteps: Sarah Loebman, Jillian Bellovary, Amy Kimball, and Daryl Haggard. Thanks as well to Nancy Finelli and the UW Women's Re-entry program, which provided vital guidance for me as an older, returning student. I am grateful to dear friends Susan Allison, Maggie Tennessen, Yvonne Lopez, Kara Revel, Catherine Shiao, Denise Tarr, Raina Paris, and Allen Zadoff, David Chittick and Catherine Worth for their unwaivering support over these last five years. Thank you to my parents—my mother, who showed me that a PhD was possible, and my father, who showed me that a fully supported, creative life was possible—and my phenomenal brother John-Samuel and sister Kayla. I am also lucky to have the most eerily drama-free in-laws, who actually attempted to read my papers when they came out, and the most incredible mother-in-law, Mom Shields, for whom I'm so grateful. Thank you also to Dad Shields, whose smile and warm voice I will always remember and cherish. And finally, I'm especially grateful for my husband Steven, without whom the world would be a very unenjoyable place. Thank you for the gift of your love and support over the past 15+ years. You are my everything.

DEDICATION

For my grandmother, Delphine Simmons, who majored in Mathematics at Tennessee State University in the late 1930s. Thank you.

Chapter 1

INTRODUCTION

The last twenty years have marked a new era of astrophysical research: The study of planets orbiting stars other than our Sun. In the years since the very first planetary-mass companion was discovered orbiting another main-sequence parent star (Mayor & Queloz, 1995), close to two thousand extrasolar planets or "exoplanets" have been confirmed. These planets were discovered primarily using either the radial velocity (R/V) technique (Marcy et al., 1997), or with NASA's *Kepler* mission (Borucki et al., 2006), which uses the transit method to detect planets that pass in front of their parent stars from the vantage point of Earth. At the time of this writing, *Kepler* has nearly doubled the number of known exoplanets, and identified thousands more candidate planets awaiting confirmation, thus widely expanding opportunities for comparative planetology within the field of exoplanet astronomy. As observational instrumentation reaches higher levels of sensitivity, the astronomy community moves closer to the "holy grail" in the field of exoplanet research: The discovery of a habitable planet like the Earth, capable of supporting and maintaining life over long timescales, and perhaps currently hosting life. Habitable planets are of high interest to the field of astrobiology, which addresses fundamental questions about the origin of life on Earth, how it has evolved and will continue to evolve over time, and how prevalent and widely distributed life might be throughout the universe (Des Marais et al., 2008). The field was born from a single question posed by scientists, philosophers, and many throughout the world since the emergence of conscious thought: Are we alone in the universe?

To answer this question we need to understand life's requirements and the factors that determine whether a planet is able to support life. The fundamental requirements for planetary habitability include: (1) The presence of regions of liquid water, (2) a suitable environment for the formation of complex organic molecules, and (3) an energy source (Des Marais et al., 2008). A terrestrial planet, by nature, has an energy source, be it stellar or

chemical, along with the basic building blocks (in some form) that are needed for life, such as sulfur, phosphorous, oxygen, nitrogen, carbon, and hydrogen ("SPONCH", Hoehler, 2007). What isn't as common is liquid water, because it requires a particular climate capable of maintaining the requisite range of temperatures and pressures to keep water in its liquid form. Life on Earth uses a diversity of metabolisms, and every one of them requires liquid water for chemical bonding and as a solvent for chemical reactions (Mazur, 1980; Kushner, 1981; McKay, 1991). Therefore, liquid water drives our search for life elsewhere.

For extrasolar planets the presence of surface liquid water is the most important indicator of a habitable planet. While ice-covered planets may still have habitable sub-surface water environments (Tajika, 2008), global ice cover would make remote detection of sub-surface life difficult. A planet with a climate that supports the maintenance of water in liquid form on the surface would allow any life within such an aqueous environment to make its presence known in ways that may be observable spectroscopically within the planet's atmosphere. As climate is described by the elements of temperature, precipitation/evaporation, atmospheric humidity, and pressure (Thornthwaite, 1948), these elements contribute to whether or not liquid water can be sustained on a planet's surface. At Earth's present surface pressure (1 bar), surface liquid water requires planetary surface temperatures between the freezing and boiling points of water, 273° K and 373° K, respectively.

What determines whether an exoplanet that we discover falls within or outside of the temperature range required to maintain surface liquid water? The locus of orbits around a star where a planet with an Earth-like atmosphere (CO_2-H_2O-N_2) can support liquid water on its surface is referred to as the star's habitable zone (Hart, 1979; Kasting et al., 1993). Too close in to a star, and a planet's atmosphere becomes saturated with water vapor. Water is more easily lost to space in this "moist greenhouse" state, due to its high concentration in the upper atmosphere (Kasting, 1988). At closer distances to the star the inner edge of the habitable zone is reached. Called the "runaway greenhouse" limit, this is where the entirety of a planet's water inventory is lost to space (Ingersoll, 1969). At the outer edge of a star's habitable zone lies the maximum CO_2 greenhouse limit–the planetary orbital distance beyond which an increase in atmospheric CO_2 concentration is no longer sufficient to maintain surface temperatures above the freezing point of water (Kasting et al.,

1993; Underwood et al., 2003; Pierrehumbert, 2010; Kane & Gelino, 2012; Kopparapu et al., 2013a,b). The identification of an exoplanet receiving the amount of incident radiation from its host star (hereafter "instellation") to lie within the star's habitable zone has been the primary step taken by observers in classifying a planet as potentially habitable. However, recent research and the history of our own planet has shown that many factors and processes can affect climate and planetary habitability. Determining whether a planet is in fact habitable for surface life requires an understanding of these many factors, which include both stellar and planetary influences. The Earth itself has undergone extreme climate events that may have had important consequences for life even while lying comfortably within the boundaries of its parent star's habitable zone.

1.1 Lessons from Earth's History: Snowball Earth

The Earth is believed to have experienced multiple climate changes over its 4.5 billion year lifetime, including glacial episodes. Geologic and paleomagnetic evidence (Hoffman & Schrag, 2002; Hoffman & Li, 2009) indicates that three of these glacial periods extended to low-latitudes, and are termed "Snowball Earth" events (Kirschvink, 1992). Initiation of the Neoproterozoic Snowball Earth events of $\sim$ 635 and 720 million years ago has been attributed to a breakdown in the carbonate-silicate cycle mechanism (Pierrehumbert et al., 2011), which stabilizes Earth's climate at present through an inverse relationship between atmospheric CO_2 concentration and planetary surface temperature (Walker et al., 1981). The excessive drawing down of CO_2 via weathering of large amounts of exposed continent, coupled with a lower solar flux from the Sun during this time (94% of the present solar luminosity, Pierrehumbert et al., 2011), led to steadily decreasing surface temperatures on the planet. As temperatures decreased, the albedo (reflectivity) of the Earth's surface increased due to an advancing ice layer. Most of the incident sunlight was reflected back to space, further reducing surface temperatures, and creating more ice and snow in a loop of positive ice-albedo feedback that led to continental ice sheets advancing all the way to the equator, and the oceans freezing over (Pierrehumbert et al., 2011). An artistic rendering of what Snowball Earth might have looked like from space is depicted in Figure 1.1.

However, land and suberial volcanic outgassing continued, allowing CO_2 to build up in

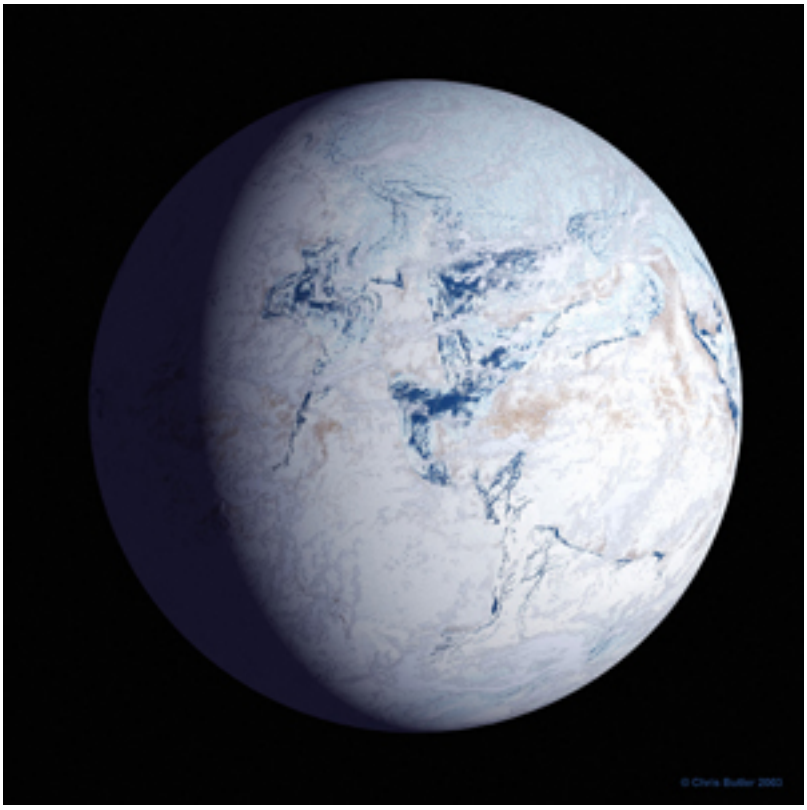

Figure 1.1 An artist's impression of Snowball Earth.

the atmosphere over a period of ∼ten million years. Constraints based on oxygen isotopic anomalies in sulfate minerals indicate that the highest atmospheric concentration of CO_2 at the end of the last Snowball episode reached ∼0.08 bar (Bao et al., 2009). Assuming a lower surface albedo due to dust accumulation during Snowball episodes, deglaciation under these CO_2 constraints is plausible (Abbot & Pierrehumbert, 2010). Once surface temperatures exceeded the freezing point of water, deglaciation was fast, perhaps taking less than a few thousand years (Pierrehumbert et al., 2011), as indicated by the presence of rapidly-deposited cap carbonate formations found globally (Hoffman et al., 1998).

While most studies have focused on the entrance into and exit out of snowball states on Earth, such extreme events of global ice cover may represent a relatively long-lived climate condition possible on exoplanets, and therefore one that may be observed in the

exoplanet population. The Neoproterozoic Snowball Earth episodes have been linked to the emergence of multicellular life on Earth, by enhancing the flux of dissolved phosphates into the ocean, causing increased primary productivity and organic carbon burial, and leading to the rise of oxygen in the ocean and atmosphere (Planavsky et al., 2010). Planets less likely to experience such global-scale glaciations may therefore be dependent on alternate pathways to serve as catalysts for biological evolution. However, snowball episodes and their aftermaths may pose significant challenges for photosynthetic life, and any marine or land life with narrow temperature constraints (Pierrehumbert et al., 2011). Snowball episodes could have important consequences, whether positive or negative, for life and the habitability of a planet. It is therefore crucial to quantify the degree of ice coverage, the likelihood of snowball states, and the processes that might trigger them on exoplanets with varied characteristics. Given the diverse population of observed planets orbiting stars different from our Sun, identifying planets that may be more likely to exhibit stable climates over long timescales will serve as a critical step towards developing the short list of exoplanet targets that will be probed remotely for signs of life by future exoplanet characterization missions.

1.2 Stars and habitability

The visual differences in color between stars disclose the most fundamental property governing their nature and evolution: Mass. Stars that appear redder have cooler photospheric temperatures (the photosphere is the deepest region of the star that is still transparent to photons), due to their relatively small masses (0.08-0.5 $M_{\odot}$) compared to the Sun. This smaller mass causes these stars to burn their nuclear fuel (converting hydrogen to helium as main-sequence, "dwarf" stars) at a much slower rate (Iben, 1967; Tarter et al., 2007). The slower the fuel-burning rate, the lower the star's luminosity, and the cooler the stellar photospheric temperature. These small, cool, red-dwarf stars are generally referred to as M dwarfs. K-dwarf stars, with intermediate masses between M-dwarf stars and G-dwarf stars like the Sun, have temperatures and luminosities between the two stellar types. F-dwarf stars, with higher masses than the Sun, burn their fuel more rapidly, and therefore generate higher luminosities and photospheric temperatures, with a whitish appearance to the eye.

A-, B-, and O-dwarf stars, which are more massive and fast-burning than F-dwarf stars, are the hottest and most luminous stars in the galaxy. While any type of star could host a planet, certain types of stars offer clear advantages for planetary habitability.

Habitable zone planets are more likely to be found around M-dwarf stars. M-dwarfs are believed to comprise ∼70% of all stars (Bochanski et al., 2010), therefore they offer the best chance to find orbiting habitable planets through sheer numbers alone. Statistical surveys have identified a factor of 3 higher occurrence rate of planets orbiting M-dwarf stars than earlier-type stars (Swift et al., 2013). Recent research has also shown that smaller planets are more abundant around lower-mass stars (Howard et al., 2012), and the smallest potentially habitable world to date was discovered orbiting in a closely-packed M-dwarf system (Quintana et al., 2014). Estimates suggest that half of all M-dwarf stars have at least one Earth-like planet (0.5-1.4 $R_{\oplus}$) orbiting in their habitable zones (Dressing & Charbonneau, 2013; Kopparapu, 2013). These results indicate that M dwarfs are the likeliest hosts for rocky planets in their stellar habitable zones, and that these planets also reside in systems with multiple worlds.

Earth-sized planets around M-dwarf stars are also easier to detect with existing techniques. Both stellar radial velocity and photometric transit depths are larger given the lower star-to-planet mass and size ratios (Tarter et al., 2007). Because of the lower luminosities of M-dwarfs, their habitable zones will be much closer to the star (0.24-0.44 AU for an early-type M-dwarf, assuming a photospheric temperature of 3800 K and luminosity of 0.05 $L_{\odot}$, Kopparapu et al., 2013a,b) than for Sun-like stars (0.99-1.67 AU, Kopparapu et al., 2013a,b), as shown in Figure 1.2. This increases the geometric probability of observing a transit, which scales inversely with a planet's orbital distance from its host star (Borucki & Summers, 1984).

The enhancement in detectability of planets orbiting M-dwarf stars (henceforth called "M-dwarf planets"), and their more likely role as habitable planet hosts means that these planets will likely be the first that we characterize in the search for habitability and life beyond our Solar System. Additionally, their small masses and slower fuel-burning rates compared to the Sun make them extremely long-lived, offering lengthy timescales for planetary and biological evolution. However, when it comes to the spectral energy distributions

of stars, M-dwarf stars have unique radiative properties among all stellar types, and this makes the star-planet interaction unique as well. The effect of this interaction on climate and habitability makes M-dwarf planets scientifically interesting targets in particular, and their analysis has important implications for prioritizing planets for closer study by future missions such as the Transiting Exoplanet Survey Satellite (*TESS*, Ricker et al., 2009, 2014).

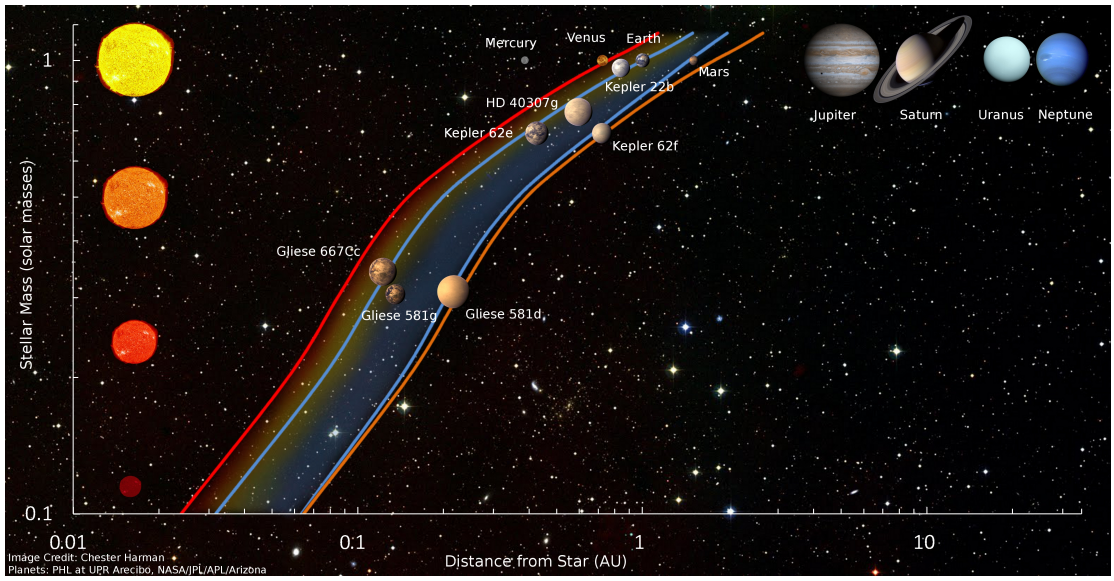

Figure 1.2 The Habitable Zone as a function of stellar mass. The conservative estimate of the inner (moist greenhouse) and outer (maximum CO_2 greenhouse) limits are plotted as blue lines. The optimistic inner (recent Venus) and outer (recent Mars) limits are plotted as red and orange lines, respectively. The location of planets in our Solar System, as well as select exoplanets such as Kepler-62e and f are also plotted relative to these boundaries. Figure credit: Sonny Harman.

1.3 The star-planet interaction

The interaction between a host star and its orbiting planet can generate both radiative and gravitational effects on planetary climate (Budyko, 1969; Barnes et al., 2008, 2009, 2013; Kopparapu et al., 2013a,b; Yang et al., 2013; Shields et al., 2013, 2014). While these effects on climate are largely constrained and understood for the Earth, exoplanets fill a much more diverse range of planetary and stellar properties. To identify habitable exoplanets,

it is important to understand the basic factors and processes affecting the Earth's climate, and how the climatic effects of these processes might change for different host stars and planetary and orbital characteristics. Quantifying the most significant effects of the star-planet interaction on planetary climate and ice coverage is the purpose of the work presented here.

1.3.1 Radiative mechanisms

Planetary climate is governed by incoming stellar radiation, and the response of a planet's atmosphere and surface to that radiation, given the planet's physical and orbital properties. Earth's temperature and ice cover extent have been shown to be greatly influenced by variations in solar radiation (Budyko, 1969). The relationship between a planet's surface temperature and the amount of stellar radiation it receives is based on an energy balance between the incoming radiation from the host star, and the outgoing thermal emission from the planet. This balance of energy can be expressed quantitatively in the following way:

$$\frac{1}{4}S \times (1 - A) = \epsilon\sigma T_e^4 \tag{1.1}$$

$$\text{energy absorbed} = \text{energy emitted}$$

where S is the solar constant (in the case of the Earth), or amount of incoming solar radiation per unit area incident on the planet at the mean Sun-Earth distance; A is the broadband or "Bond" albedo, defined as the ratio of the total amount of flux reflected by the planet, divided by the total flux incident on the planet, integrated over the entire wavelength spectrum (typically 0.3 for the Earth); ϵ is the mean emissivity of the surface at thermal wavelengths (approximately equal to 1); σ is the Stefan-Boltzmann constant; and T_e is the equilibrium temperature of the planet without an atmosphere (Sagan & Mullen, 1972). The factor of $\frac{1}{4}$ derives from the ratio between the circular area of the planet over which incoming sunlight is received (πr^2), and the spherical area over which thermal radiation is emitted ($4\pi r^2$).

The equilibrium temperature is the temperature of the layer of the atmosphere from which the majority of the radiation from a planet is emitted. Given that the atmosphere

is thicker and more opaque to radiation at the surface where the pressure is greater, the emitting layer where radiation can escape to space is at a much higher altitude in the atmosphere, where temperatures are colder. The equilibrium temperature therefore gives almost no information about the surface temperature of a planet, which depends on the planet's atmospheric composition. Depending on the strength of the greenhouse effect, a planet's surface temperature can be tens of degrees warmer than its equilibrium temperature, as in the case of the Earth (Sagan & Mullen, 1972), or hundreds of degrees warmer, as is the case on Venus (Seiff, 1987; Bougher et al., 1997). Additionally, we often don't know the values for A and ϵ for exoplanets, making the calculated equilibrium temperature even less representative of a planet's climate.

Quantifying the effect on planetary surface temperature and climate of the interaction between incoming radiation from a host star and its orbiting planets requires an understanding of the unique spectral energy distribution (SED) of the radiation from the host star. The interaction between the stellar SED and the planet's atmosphere and surface will affect the amount of shortwave (downwelling stellar) radiation absorbed by the atmosphere and surface, the downwelling longwave radiation emitted by the atmosphere, and their combined contributions to the overall energy balance of the planet. Changes in atmospheric circulation, surface temperature, and ice extent that are induced by this changing energy balance will therefore differ for planets orbiting stars with different SEDs.

The SEDs of stars of different spectral types are shown in Figure 1.3. The cooler the star, the longer the wavelength of radiation at which the star emits its peak flux. M-dwarf stars emit a large fraction of their radiation at near-IR wavelengths. About 95% of the radiation emitted by the M-dwarf star AD Leo is at wavelengths longer than 0.7 μm, compared with $\sim$53% for the Sun. Given that surfaces such as ice and snow as well as atmospheric gases exhibit their own wavelength-dependent optical properties, the interaction between the SEDs of M-dwarf stars and their orbiting planets will differ greatly from those between the Sun and the Earth, or between other types of host stars and their planets. An understanding of how this interaction changes for different host stars is necessary to provide the best possible assessment of the habitability of an observed planet.

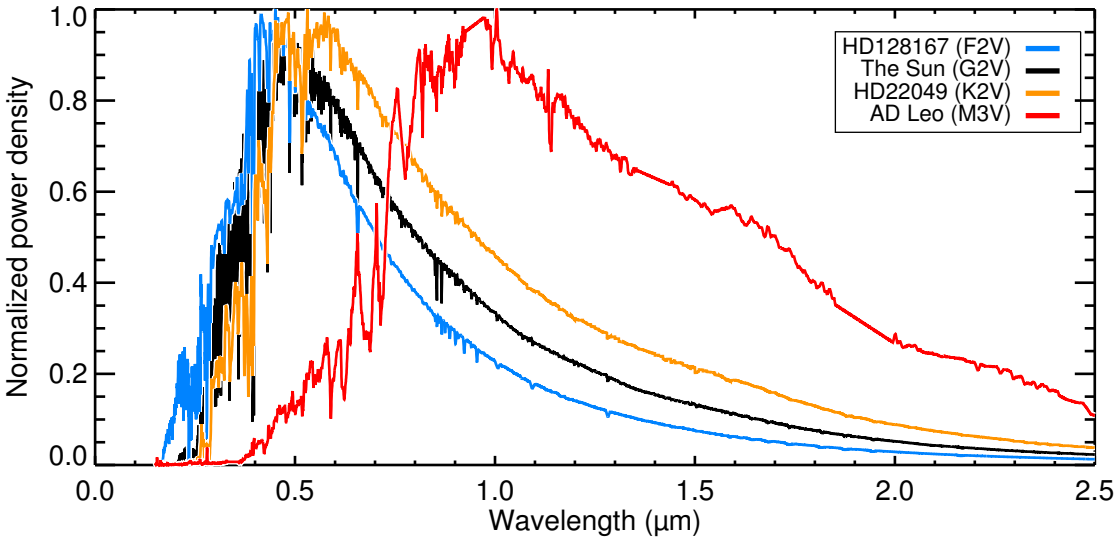

Figure 1.3 The SEDs for F-, G-, K-, and M-dwarf stars, normalized by their peak flux.

1.3.1.a The spectral dependence of ice and snow albedo

The albedo α of a surface is the fraction of incident stellar radiative energy flux reflected and scattered upward from that surface. It is expressed in its most basic form as:

$$\alpha = \frac{F_{up}}{F_{dn}} \tag{1.2}$$

where F_{dn} is the downwelling instellation at the surface, typically referred to as "shortwave" radiation (as opposed to thermal radiation emitted by the planet's surface and atmosphere); and F_{up} is the shortwave instellation that is reflected or scattered upwards and away by the surface (Grenfell, 2011).

If due to some perturbation in the climate system temperatures change on a planetary surface, the surface itself—whether, ocean, land, or ice—will respond according to its individual molecular properties. As temperatures grow colder, surface liquid water will eventually freeze to form ice, with a higher albedo than water in its liquid state. As more ice forms, it reflects more solar radiation back to space, absorbing less radiation, further lowering temperatures, and so on. Likewise, if temperatures warm, ice extent will decrease,

revealing darker land and ocean surfaces that absorb more radiation, leading to a further increase in surface temperatures and melting of more ice. This is known as a process of "positive feedback". The ice-albedo feedback mechanism plays a chief role in influencing climate change on Earth (Budyko, 1969; Sellers, 1969).

However, ice albedo has a spectral (wavelength) dependence. The spectral albedo can be expressed as:

$$\alpha_\lambda = \frac{F_{up}(\lambda)}{F_{dn}(\lambda)} \tag{1.3}$$

The broadband albedo is then given by:

$$\alpha = \frac{\int_{SW} \alpha_\lambda \cdot F_{dn}(\lambda)\,\mathrm{d}\lambda}{\int_{SW} F_{dn}(\lambda)\,\mathrm{d}\lambda} = \frac{\int_{SW} \alpha_\lambda \cdot F_{dn}(\lambda)\,\mathrm{d}\lambda}{F_{dn}} \tag{1.4}$$

Spectra of albedo as a function of wavelength for ice and snow are shown in Figure 1.4, along with the albedo spectra for ocean and a land surface for comparison. In the near-ultraviolet (near-UV, 0.3 μm $< \lambda <$ 0.4 μm) and visible (0.4 μm $\leqslant \lambda \leqslant$ 0.7 μm) range of the electromagnetic spectrum, both ice and snow albedo are high. But in the infrared and near-IR ($\lambda >$ 0.7 μm), the reflectance of ice and snow drops substantially, due to an increase in their absorption coefficients at longer wavelengths (Dunkle & Bevans, 1956); a consequence in large part of molecular vibrations involving various combinations of the water molecule's three fundamental vibrational modes (Farrell & Newnham, 1967).

The wavelength dependence of ice and snow albedo has been derived analytically assuming diffuse solar irradiation (Dunkle & Bevans, 1956). Subsequent model comparisons with field measurements have verified the spectral behavior of ice and snow albedo, and highlighted its dependence on directional irradiation and solar zenith angle, as well as grain size, with absorption and forward scattering of radiation increasing for larger grains (Wiscombe & Warren, 1980). A photo of the two end members of ice albedo in Figure 1.4 is shown in Figure 1.5–that of large-grained blue marine ice, and fine-grained snow. Since ice albedo is wavelength and grain size dependent, the behavior of the ice-albedo feedback mechanism depends on the type of water ice on the planet, the type of radiation coming from the host star, and the interaction between the two.

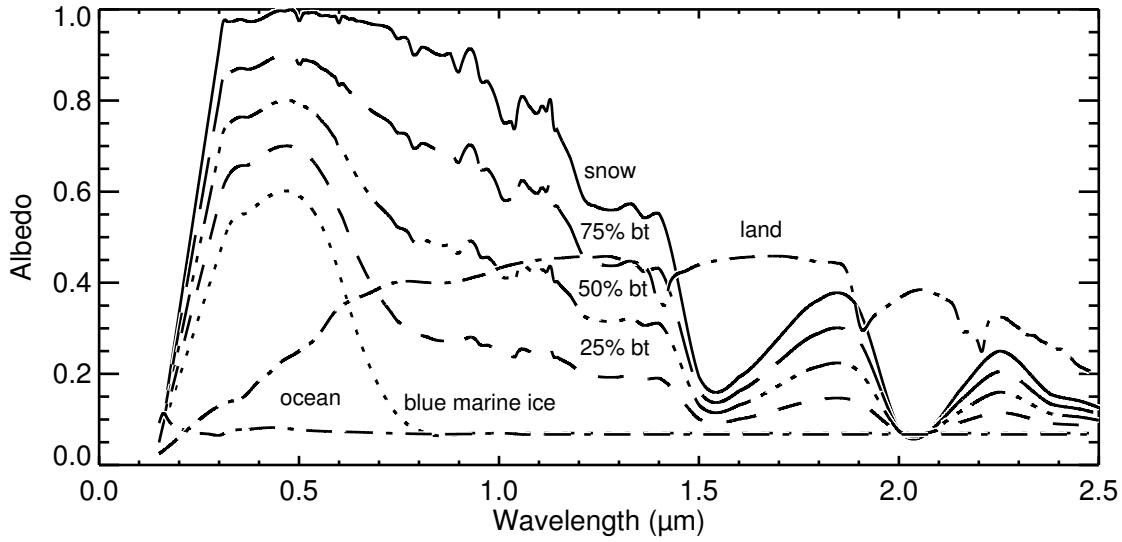

Figure 1.4 The spectral distribution of fine-grained snow, blue marine ice, and 25%, 50%, and 75% mixtures of the two end-members. Ocean and land spectral distributions are also plotted.

1.3.2 Radiative consequences for exoplanets

When considering the effect of ice-albedo feedback on Earth's planetary climate, the most common interaction is that between ice and our own host star, the Sun. Since the majority of incoming solar radiation is in the visible part of the spectrum, where ice and snow are strongly reflective, the effect of this feedback on Earth's climate is largely cooling. However, because of the spectral dependence of ice albedo, the ice-albedo feedback mechanism is sensitive to the wavelength of light coming from the host star. For M-dwarf stars, whose instellation is largely composed of near-IR radiation, ice and snow on orbiting planets may behave quite differently, since they have a much lower albedo in the near-IR. On M-dwarf planets, the cooling effect of ice-albedo feedback may be suppressed.

On M-dwarf planets, a significant amount of radiation emitted by the host star is absorbed by atmospheric gases such as CO_2 and water vapor, which have strong absorption bands in the near-IR (Kasting et al., 1993; Selsis et al., 2007). However, a disproportionate amount of the longer-wavelength radiation that does reach the surface will be absorbed by,

Figure 1.5 Fine-grained snow and blue marine ice are both shown in this photo taken in Antarctica by Stephen Warren. These two ice types constitute end-members in terms of ice grain size and albedo at Earth-like surface temperatures and pressures.

rather than reflected from, icy or snowy surfaces on these planets (Joshi & Haberle, 2012). This will reduce the difference between ice and ocean surface albedo. As entrance into and exit out of snowball states have been shown to be sensitive to ocean-ice albedo contrast (Pierrehumbert et al., 2011), snowball states may be less likely to occur on M-dwarf planets.

Similarly, planets orbiting stars with higher visible and near-UV output, given the higher albedos of ice and snow at these wavelengths, will experience a different climatic response. The susceptibility of planets to entering snowball states is therefore going to be sensitive to the host star SED, the ice grain size and albedo on the planet's surface, and the composition and absorption properties of its atmosphere. While preliminary research in this area indicated that the outer edge of the habitable zone may be wider for M-dwarf stars as a result of the spectral dependence of ice albedo (Joshi & Haberle, 2012), this work was purely analytical, and applied a heavily approximated approach to the interaction between both the M-dwarf SED and atmospheric gases such as CO_2.

A planet's ability to thaw out of global ice cover as its host star ages and brightens may also be influenced by the SED of its host star. Planets orbiting beyond their host stars' habitable zones may exist in stable, globally ice-covered states (Budyko, 1969; Sellers, 1969). As mentioned previously, exit out of Snowball Earth is often attributed to the build-up of CO_2 in the atmosphere as a result of volcanic outgassing and decreased silicate weathering (Pierrehumbert et al., 2011). Given that the carbonate-silicate cycle on Earth is sensitive to plate tectonic speeds and mantle degassing rates (Driscoll & Bercovici, 2013), the efficiency of a similar mechanism on other planets may be variable. Without a continuously-operating carbon cycle to stabilize the climate, the steady brightening of their host stars over time (Iben, 1967; Gough, 1981) may be the dominant mechanism by which planets become hospitable for surface life. Such a scenario has been referred to as a "cold start" (Kasting et al., 1993). A cold start is a possible path for an extrasolar planet orbiting beyond the outer edge of its host star's habitable zone, and super-Earth-mass planets in these types of orbits have already been found by microlensing surveys (Beaulieu et al., 2006). Planets that exhibit greater climate stability, through a resistance to entering into or remaining in episodes of low-latitude glaciation, may be more likely hosts for surface life over long timescales, and the preferred targets for follow-up missions.

M-dwarf stars also exhibit high degrees of chromospheric activity, resulting in flares that emit significant amounts of high-energy radiation (Hawley & Pettersen, 1991), which could affect planetary composition and be detrimental to surface life. However, photochemical and radiative/convective models have yielded a maximum depletion in atmospheric ozone number density of 1% due to UV radiation emitted by flares, indicating that planetary surface habitability may not be unequivocally threatened by stellar flare events (Segura et al., 2010). The addition into simulations of the proton flux that can be associated with stellar flares results in a reduction in ozone column depth by as much as 93%. This is an upper limit, as not all flares are accompanied by the ejection of energetic ionizing particles, and the effect of flare-associated particle ejections on atmospheric ozone concentration could be ameliorated by a planet's magnetic field (Segura et al., 2010).

1.3.3 Gravitational mechanisms

Climate is also affected by a planet's orbital elements and their evolution over time, and these in turn are affected by gravitational interactions between the planet, its host star, and perhaps other planets in the planetary system. The relationship between planetary obliquity (the angle between the orbital spin axis and the axis perpendicular to the orbital plane) and climate is long established, with seasonality increasing strongly for large obliquities (Ward, 1974; Williams, 1975; Williams & Pollard, 2003). For obliquities greater than 54°, the equatorial regions of a planet receive less stellar insolation annually than the poles, and previous modeling efforts have examined the likelihood of low-latitude glaciation at high obliquity on planets orbiting Sun-like stars (Williams, 1975, 1988; Hunt, 1982; Jenkins, 2000; Williams & Pollard, 2003; Spiegel et al., 2009). Using a one-dimensional energy balance climate model, Spiegel *et al.* (2009) found that high-obliquity planets orbiting G-dwarf stars may be less susceptible to snowball episodes. And modeled G-dwarf planets that undergo high-frequency obliquity oscillations are more stable against global-scale glaciation (Armstrong et al., 2014).

The annual global insolation received on a planet increases with increased eccentricity (Berger et al., 1993; Williams & Pollard, 2002; Berger et al., 2006), in accordance with the following relation:

$$S = \frac{S_a}{\sqrt{1 - e^2}} \tag{1.5}$$

where S is the average instellation at the mean star-planet distance, as in equation (1.1); S_a is the instellation at a given distance a from the star during a planet's orbit; and e is the eccentricity of the planet's orbit (Berger et al., 2006). Small increases in Earth's eccentricity associated with its 100,000-yr eccentricity cycle have been shown to correlate with decreased ice volume on the planet's surface (Hays et al., 1976; Berger et al., 1990). Research has found that high-eccentricity planets receiving instellation from a Sun-like star melt out of snowball states more easily (Spiegel et al., 2010). However, this study was limited to one particular type of host star and wavelength-independent surface ice albedo, and since it was done with a one-dimensional model, lacked a detailed analysis of atmospheric circulation on the planet.

Changes in ocean coverage fraction on a G-dwarf planet with low-eccentricity can also affect the transition to global ice cover, due to the high thermal inertia of the ocean, which increases its resistance to large temperature changes compared to areas with high land coverage fraction (Dressing et al., 2010; Pierrehumbert et al., 2011). Additionally, the transport of heat by the ocean from the equator to the pole can slow the transition into a snowball state compared to simulations where ocean heat transport is excluded (Poulsen et al., 2001; Pierrehumbert et al., 2011).

1.3.4 Gravitational consequences for exoplanets

The question of whether any observed planets orbiting low-mass stars are habitable is complicated by the close proximity of the habitable zone to the parent star. In such close-in orbits, tidal effects are expected to be strong, and could lead to capture into resonances in spin-orbit period (Dole, 1964). A 1:1 spin-orbit resonance such as synchronous rotation may occur, where the planet takes as long to make one rotation as it does to complete one orbit around its star. Such spin states may cause enhanced radiative cooling (Heng & Kopparla, 2012), weakened low-latitude zonal winds (which also cool a planet), and increased atmospheric latent and oceanic diffusive heat transport, which reduces temperature contrasts between the sunlit and dark sides of an aqua planet (Edson et al., 2011), where no continent is present. Initial concerns about the atmospheres of M-dwarf planets condensing out on the permanent night side were assuaged by climate simulations of synchronously-rotating M-dwarf planets, which suggest that 0.1 bar of a greenhouse gas such as CO_2 is enough to ensure sufficient heat transport between the sun-lit and dark sides of the planet, preventing atmospheric freeze-out (Joshi et al., 1997; Edson et al., 2011). Recent work has also indicated that there may be a climatic benefit of synchronous rotation on M-dwarf planets, by suggesting that the inner edge of the habitable zone is a function of planetary rotation rate, and can be moved closer to the star for synchronously rotating planets due to cloud formation at the substellar point, which buffers these planets against runaway greenhouse states (Yang et al., 2013).

An understanding of the effect of tidal interactions on orbital evolution and planetary

habitability is vital given the close proximity of K- and M-dwarf planets orbiting in the habitable zones of their stars, and the likelihood of additional planetary companions in these systems. Tides raised between a star and a close orbiting planet introduce torques on the planet, resulting in changes in semi-major axis and eccentricity (Barnes et al., 2008, 2009), obliquity (Heller et al., 2011), and surface heating (Barnes et al., 2013). The eccentricity of a close-in planet, which can otherwise be damped due to tidal interactions between a planet and its host star, will undergo oscillations in the presence of outer companions in the system (Mardling, 2007), and may be pumped to significantly higher values (Correia et al., 2012). Given the relationship between eccentricity, annual global insolation, and planetary ice coverage (Hays et al., 1976; Berger et al., 1990), large changes in eccentricity may have profound effects on atmospheric circulation and evolution, as well as planetary surface conditions.

1.4 Outline

In subsequent chapters, I discuss a theoretical approach to examining the influence on planetary climate of the interaction between a planet and its parent star. First, the climate models used in this study are introduced, described, and validated. Then, beginning with habitable surface temperatures and low planetary ice cover, a "warm start", the effect of stellar SED and ice-albedo feedback on a planet's susceptibility to enter snowball states as the instellation is decreased is explored. A variety of possible ice grain sizes and densities is applied to examine the effect of these surface types on planetary climate. And a planet's climate sensitivity to the surface and to ice-albedo feedback given high amounts of atmospheric CO_2 (assuming a carbonate-silicate cycle operates on these planets) are also explored and compared for host stars of different spectral types.

The influence of stellar SED on climate stability is then examined, by comparing the amount of instellation required to melt out of a snowball state on planets orbiting M-, G-, and F-dwarf stars, assuming fixed atmospheric CO_2. If an active carbon cycle does operate on these distant outer worlds, the exit out of a snowball state with Earth's present level versus the maximum level of atmospheric CO_2 believed to exist at the end of Snowball Earth (0.1 bar, Pierrehumbert et al., 2011) is also compared for planets orbiting different

types of stars.

As lower-mass stars are likely candidates for multiple rocky planets, gravitational interactions among potentially habitable planets may have significant effects on climate and planetary habitability over orbital periods and longer timescales, depending on the oscillation behavior of orbital elements in the system. A specific case is explored—that of Kepler-62 (Borucki et al., 2013), a K-dwarf star that is host to five planets, including two in the star's habitable zone. Using an n-body model, the orbits of the planets in this system are numerically integrated to determine the highest initial eccentricity possible for Kepler-62f while maintaining stability within the system. The effects of eccentricity, rotation rate, obliquity, and insolation asymmetry on the climate and surface habitability of this planet are explored using 3-D climate models. This is the first time that n-body dynamical constraints have been used to direct 3-D global climate model simulations. The implications of these stellar and planetary interactions for the evolution of climate stability and planetary habitability are then discussed.

Chapter 2

METHODS I: MODELING THE CLIMATE OF EXTRASOLAR PLANETS

This work provides a comprehensive exploration of a range of star-planet interactions and their effects on planetary climate and habitability, using a hierarchy of models which have been modified to simulate planets orbiting different types of stars. In this chapter I describe the models and inputs used to explore the climate of extrasolar planets. An energy balance climate model was used to calculate planetary global surface temperatures and ice line latitudes. To simulate the interaction between the planetary surface and the incoming stellar radiation from stars of different spectral type, a radiative transfer model was used to generate broadband planetary albedos from input stellar and planetary surface spectra. I also describe the more sophisticated, three-dimensional (3-D) general circulation model (GCM) that was used to explore the response of the atmosphere and its interaction with the ocean, and the specific modifications that were made to the GCM to allow the modeling of planets orbiting stars with SEDs very different from that of the Sun. Portions of this chapter were originally published in collaboration with V. S. Meadows, C. M.. Bitz, et al. in the August 2013 edition of the journal Astrobiology (Shields et al., 2013, *Astrobiology*, Vol. 13, pp. 715-739;), and with C. M.. Bitz, V. S. Meadows, et al. in the April 2014 edition of Astrophysical Journal Letters (Shields et al., 2014, *ApJ*, Vol. 785, L9;), and are reproduced below with permission of Mary Ann Liebert, Inc. and the American Astronomical Society, respectively.

2.1 Introduction

Finding an Earth-like planet—with atmospheric and surface conditions conducive to the presence of liquid water—requires the application of theoretical approaches in addition to advances in observational instrumentation. Computer models can be used to comprehensively explore a wide range of parameter space, and to constrain self-consistent combinations

of planetary and stellar characteristics. As more characteristics of a planetary system are identified by observational methods, these specific stellar and planetary traits can be applied to model calculations, providing a more precise assessment of the likely climate state and habitability potential of planets within a given stellar system. Here I describe our method of using a hierarchy of models to explore the effect of host star SED and ice-albedo feedback on planetary climate. The models in our hierarchy are: an energy balance model, which provides a general overview of a planet's surface temperature and ice extent as a function of instellation; a radiative transfer model that provides input to the energy balance model; and a global climate model, that permits a more detailed analysis of the atmospheric dynamics and circulation on a planet.

2.2 Climate Models

A climate model is a mathematical representation of a climate system, taking into account the physical, chemical, and biological properties of the system. Climate models span a wide range of complexity. Some models, like the model expressed analytically by equation (1.1), are zero-dimensional, treating the average energy of a planet as steady state, as shown in Figure 2.1. Other models, like one-dimensional energy balance models, generate data that are zonally averaged over latitude. And still others, such as general circulation or global climate models, determine output over a numerical grid with a high spatial resolution, and contain individual, coupled components governing the behavior of the atmosphere, ocean, land, and sea ice, and the interactions between them. The greater the number of physical regions into which a planet is divided, the more complex the model becomes, and the greater the need for computational techniques to solve the necessary equations describing more detailed physical and chemical processes. Even models with the highest resolution miss small-scale processes such as atmospheric turbulence and detailed cloud microphysics. And within our own Earth climate system there are still fine details about atmosphere and ocean circulation that are unknown. Therefore, inherent uncertainties exist in every climate model, depending on the specific parameterizations adopted.

Each type of climate model offers its own benefits and disadvantages. Models that offer reduced computational time require sacrifices in spatial and wavelength resolution (by

strongly generalizing radiative transfer through the atmosphere, for example). However, they allow the exploration of a wide parameter space, and provide a quick identification of general trends in climate given changes in specified parameters. Models of high complexity and resolution demand long run times, making the exploration of a wide parameter space computationally expensive and time-consuming. However, they provide a detailed analysis of radiative transfer, atmospheric circulation, and the interaction between the atmosphere and the ocean. Used in tandem, both models provide a robust and complementary examination of the effect of perturbations in planetary or stellar parameters on the overall climate system of a planet.

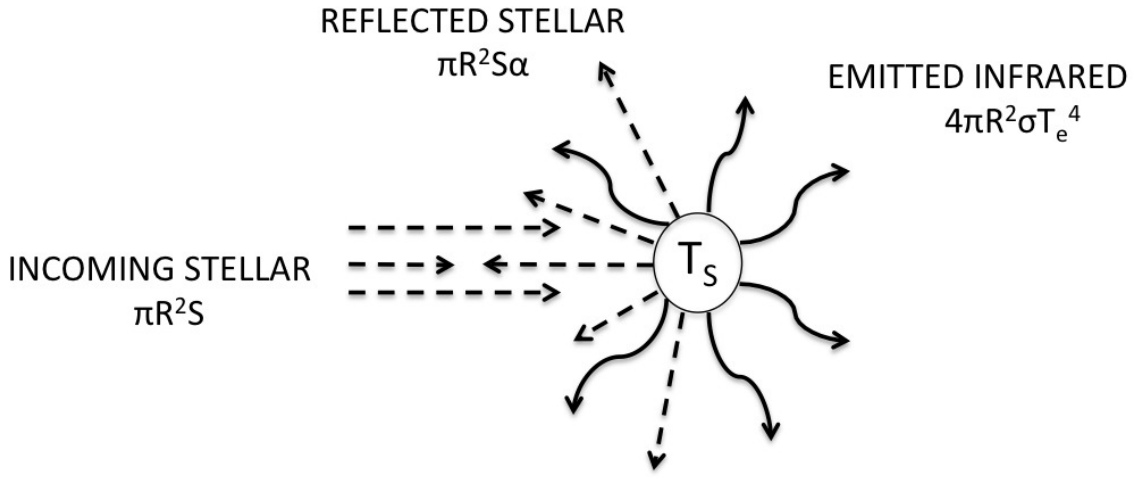

Figure 2.1 Schematic diagram of a zero-dimensional energy balance model, based on Figure 3.1a in *A Climate Modeling Primer*, K. McGuffie and A. Henderson-Sellers, Wiley, pg. 83, (2005). Here the planet is treated as a single point in space, with a global mean effective temperature T_e and surface temperature T_s. If there are greenhouse gases in the atmosphere $T_s = T_e + \Delta T$. Here the emissivity ϵ is assumed to be unity.

2.2.1 Energy Balance Model

Energy balance climate models (EBMs) simulate the climate from an equation that expresses the balance between the incoming radiation from a host star, and the outgoing thermal emission from an orbiting planet, similar to the generalized energy balance equa-

tion (1.1) given in Chapter 1. Here a seasonally varying, one-dimensional (1-D, in latitude) EBM adapted from North and Coakley (1979) is used, where the surface temperature is latitudinally resolved. The energy balance at each latitude is the sum of absorbed shortwave radiation, outgoing longwave radiation, and the convergence of horizontal heat transport equated with the tendency of the vertical column to receive and store heat (Figure 2.2). The model solves two one-dimensional energy balance equations, provided here based on those in North and Coakley (1979):

$$QS(x,t)(1-\alpha_L) = C_L\frac{dT_L}{dt} - \frac{d}{dx}D(1-x^2)\frac{dT_L}{dx} + \frac{\nu}{f_L(x)}(T_L - T_W) + (A + BT_L) \quad (2.1)$$

$$QS(x,t)(1-\alpha_W) = C_W\frac{dT_W}{dt} - \frac{d}{dx}D(1-x^2)\frac{dT_W}{dx} + \frac{\nu}{f_W(x)}(T_W - T_L) + (A + BT_W) \quad (2.2)$$

The left hand side of these equations represents shortwave radiation absorbed by the planet for land (L) and water (W), where Q is the solar constant divided by 4 ($\sim$340 W/m^2 at present), and $S(x,t)$ is the fraction of incident solar radiation received by latitude x at time t. The solar flux absorbed at a given latitude and time t is then equal to $S(x,t)$ multiplied by $Q(1-\alpha(x,t))$, where $(1-\alpha(x,t))$ is the planetary coalbedo (the fraction of incident flux absorbed over land or ocean), which depends on temperature (to mimic the presence of ice on the planet when the ocean temperature goes below freezing).

The first term on the right hand sides of both equations represents the planetary response to this absorbed shortwave radiation, given the thermal inertia, or heat capacities per unit area, of the land (0.452 Wm$^{-2\circ}$C^{-1}) and ocean (9.82 Wm$^{-2\circ}$C^{-1}) surfaces (C_L and C_W, respectively). This term is positive because the change in the temperature of the land or water, multiplied by the amount of energy required to change the temperature by a certain amount, determines whether heat is gained or lost from the particular latitude zone.

The second term on the right hand sides of (2.1) and (2.2) describes the transport of heat across the planet. In equilibrium, the incident shortwave radiation absorbed by the Earth is not exactly balanced by the outgoing longwave radiation emitted by the planet. The solar flux absorbed at the top of the atmosphere over the tropics is greater than that over the poles. This imbalance is compensated for by the meridional (north-south) divergence of

heat flux, which transports heat from areas of energy surplus (lower latitudes) to areas of energy deficit (higher latitudes). This transport is modeled diffusively by the term $D\nabla^2 T$, where D is a thermal diffusion coefficient fit to Earth's present climate. A typical value for D is 0.442 $\mathrm{Wm}^{-2\circ}\mathrm{C}^{-1}$, and this is the value we used in Equations (2.1) and (2.2).

The third term on the right hand side of these equations governs the relationship between ocean and land temperature gradients, where f_L is the fraction of the globe that is covered in land, with the remaining covered by ocean ($f_W = 1 - f_L$). Here ν is the coefficient governing the strength of coupling between land and ocean temperature, which we set at 3.0 $\mathrm{Wm}^{-2\circ}\mathrm{C}^{-1}$. We verified that smaller values of this coefficient often seen in the literature (North & Coakley, 1979) yielded negligible differences in global mean surface temperature and ice extent given our small land fraction of 0.01 (see below). And in the fourth term on the right hand side the dependence of outgoing longwave radiation (OLR) on temperature is linearly parameterized ($OLR = A + BT$, where the standard value of the coefficient A is 203.02 $\mathrm{W/m}^2$ and the radiation constant B is 2.092 $\mathrm{Wm}^{-2\circ}\mathrm{C}^{-1}$) based on the general effect of CO_2 and water vapor on atmospheric radiative transfer as a function of planetary surface temperature in the present climate on Earth.

The North and Coakley model (1979) was first coded up as published with their parameter choices, to verify that it reproduced the results of their paper. Then it was modified as follows: Heat transport was computed from diffusion of temperature with a latitudinally-varying diffusion coefficient, which enhanced tropical relative to subtropical heat transport, thus smoothing temperature variations in the tropics and leading to consistency with thermal wind observations (Lindzen & Farrell, 1977).

We used idealized land (rectangular land without any surface topography, described by the fraction of the planet that is designated to be land, f_L). Each latitude has a land and ocean fraction specified to be uniform at 0.01 and 0.99, respectively, to approximate an aqua planet. We also used prescribed time-independent orbital parameters for all planets modeled (which are used in the calculation of the daily mean distribution of instellation, $S(x,t)$). Default values for eccentricity, obliquity, and the argument of perihelion are 0.0167, 23°, and 102.07°, respectively. For the simulations in chapters 3 and 4, the eccentricity was set to zero, so that results were symmetric in the time-mean about the equator over an

annual cycle. The instellation is spectrally integrated, and varies with latitude and time of year.

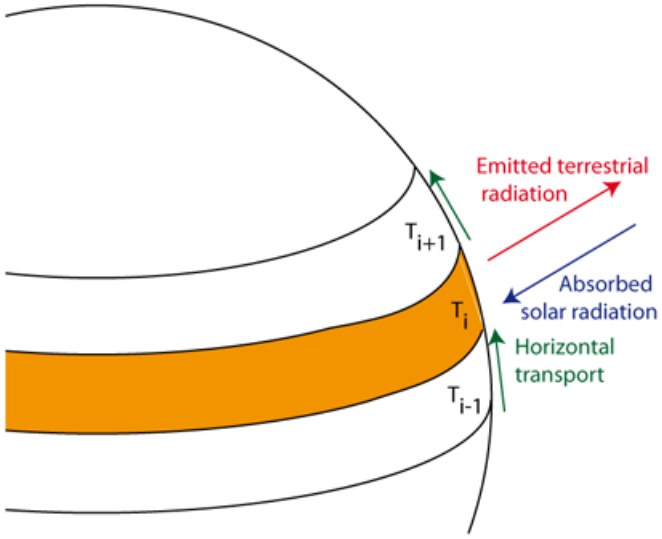

Figure 2.2 Schematic diagram of a 1-D energy balance model[1], based on Figure 3.1b in *A Climate Modeling Primer*, K. McGuffie and A. Henderson-Sellers, Wiley, pg. 83, (2005). Temperature is averaged over bands of latitude, based on the balance between absorbed solar and emitted terrestrial radiation, with horizontal heat transport from areas of energy surplus at the tropics to polar latitudes, where there is an energy deficit.

To simulate the wavelength dependent reflectivity of planets orbiting stars of different spectral type we calculated the interaction of the stellar SED with the planetary surface using a radiative transfer model. The planetary albedos we calculated (see Section 2.2.1.a) with different stellar spectra, an Earth-like atmosphere, and surface albedo files for land, ocean, and ice of varying grain size were input as broadband albedos over land and ocean in the EBM. This allowed the EBM to incorporate to first order the effect of varying SED on the energy balance of the planet.

This EBM configuration assumes a rapidly rotating planet like the Earth, via the value of the thermal diffusion coefficient D. Planets with slower rotation rates would likely distribute

[1] http://stratus.astr.ucl.ac.be/textbook/

heat more efficiently given their weaker Coriolis force (Joshi et al., 1997; Merlis & Schneider, 2010; Pierrehumbert, 2011). Additional work to examine alternate spin states such as synchronous rotation, which is expected to prevail in the habitable zones of M-dwarf stars, must be done using more sophisticated, general circulation models (see Chapter 6).

There is no explicit ice model; instead the ocean temperature is allowed to be below freezing, which then causes the albedo to increase. A general EBM land/ocean albedo parameterization is as follows:

$$\alpha_L = \begin{cases} 0.363 + 0.08(3x^2 - 1)/2; & T > -2°C \\ 0.6; & T \leq -2°C \end{cases} \tag{2.3}$$

$$\alpha_W = \begin{cases} 0.263 + 0.08(3x^2 - 1)/2; & T > -2°C \\ 0.6; & T \leq -2°C \end{cases} \tag{2.4}$$

However, the first terms in equations (2.3) and (2.4) were adjusted to the values of broadband planetary albedo calculated with our radiative transfer model for land, ocean, and below-freezing surfaces for each host star. In the Equations (2.3) and (2.4) x is the sine of the latitude, and the $(3x^2 - 1)/2)$ term is the second Legendre polynomial[2]. This latitudinally-dependent term for ice-free areas is symmetric about x. This provides for hemispherical symmetry in modeling behavior (provided that land and ocean fractions are also equal in each hemisphere), and accounts for stellar zenith angle dependence, and the nonhomogeneous annual mean distribution of clouds. We acknowledge that neglecting the energy- and time-dependent dynamics of melting ice will affect the seasonal cycle, therefore we use the EBM primarily to determine the annual mean temperature behavior, and defer to the results of our GCM simulations regarding the behavior of the ice margin. With the EBM we evaluated how the ice line latitude changed as a function of stellar flux, given the broadband planetary albedos over land, ocean, and ice-covered areas that were calculated with our radiative transfer model using different stellar spectra as input.

---

[2]Legendre polynomials are azimuthally symmetric solutions to Legendre's Differential Equation, defined as $(1 - x^2)y'' - 2xy' + n(n + 1)y = 0$

2.2.1.a Model Inputs: SMART

The Spectral Mapping Atmospheric Radiative Transfer model (SMART) is a 1-D (in altitude), multistream, multilevel, line-by-line, multiple-scattering radiative transfer model developed by David Crisp (Meadows & Crisp, 1996; Crisp, 1997), and was used here to generate high-resolution synthetic spectra of planetary atmospheres and surfaces. The SMART model parameterization combines a discrete ordinate method with a spectral mapping technique to generate spectrally-dependent solutions to the equation of radiative transfer as given by Goody and Yung (1995, p46) and Meadows and Crisp (1996):

$$\mu \frac{dI(\tau,\mu,\phi,\nu)}{d\tau} = I(\tau,\mu,\phi,\nu) - S(\tau,\mu,\phi,\nu) \tag{2.5}$$

The equation of radiative transfer governs the propagation of radiation through a medium (in this case a planetary atmosphere), which can interact with that radiation through absorption, emission, and scattering processes. Here I is the radiance (incoming stellar radiation) at wavenumber ν (here a different ν than in (2.1) and (2.2)), τ is the vertical optical depth measured from the top of the atmosphere (TOA) down, μ is the cosine of the stellar zenith angle (the angle between the point directly overhead and the center of the star's disc), and ϕ is the azimuth angle (the angle along the horizon between a reference direction and a projected line pointing to the star on the same plane). The source function is given by:

$$\begin{aligned} S(\tau,\mu,\phi,\nu) =& \frac{\omega(\tau,\nu)}{4\pi} \int_0^{2\pi} \mathrm{d}\phi' \int_{-1}^{1} \mathrm{d}\mu' P(\tau,\mu,\phi,\mu',\phi',\nu) I(\tau,\mu',\phi',\nu) \\ &+ [1-\omega(\tau,\nu)] B[\nu, T(\tau)] \\ &+ \frac{\omega(\tau,\nu)}{4\pi} F_\odot P(\tau,\mu,\phi-\mu_\odot,\phi_\odot,\nu) \exp(-\tau/\mu_\odot) \end{aligned} \tag{2.6}$$

where $P(\tau,\mu,\phi,\mu',\phi',\nu)$ is the scattering phase function, $\omega(\tau,\nu)$ is the single scattering albedo at optical depth τ and wavenumber ν, $B[\nu,T(\tau)]$ is the thermal source (Planck) function at wavenumber ν and temperature $T(\tau)$, and $F_\odot$ is the TOA instellation.

The discrete ordinate method uses Gaussian quadrature to evaluate the integrals in (2.6), by approximating them as weighted sums of values of the functions at specific points within the boundaries of integration (Stamnes et al., 1988). This provides zenith-angle- and azimuth-angle-dependent radiance fields at each atmospheric layer, rather than the

hemispherically-averaged radiances calculated using traditional two-stream solutions to the equation of radiative transfer. The high-resolution spectral mapping technique maximizes computational efficiency, by identifying similarities in the monochromatic optical properties within a larger spectral region and mapping them to a smaller number of broadband, quasi-monochromatic bins. The radiative transfer equation is then solved one time for each bin. And then the solutions are mapped back to their spectral region of origin. Inhomogeneity within the atmosphere is addressed by dividing it into ∼60 vertical layers. Optical properties are held constant within each individual layer, but are allowed to change from one layer to the next.

For modeling Earth-like planets we used the Earth's temperature-pressure profile for the atmosphere derived using the Intercomparison of Radiation Codes in Climate Models program (ICRCCM). The profile for ICRCCM mid-latitude summer sounding is representative of the average temperature-pressure profile for the Earth. It includes atmospheric pressures, temperatures, and mass mixing ratios for seven absorbing gases, and is resolved into 64 vertical layers throughout the atmosphere. Included is absorption by H_2O, CO_2, O_3, N_2O, CO, CH_4, and O_2, and Rayleigh scattering.

We generated absorption cross sections for relevant gases using the HITRAN 2008 line list database[3] (Rothman et al., 2009). We then simulated line profiles for use in our SMART runs using a line-by-line absorption coefficient model called LBLABC (Meadows & Crisp, 1996), which calculates gas absorption coefficients over a broad range of temperatures and pressures on a series of nested spectral grids, completely resolving the cores of individual gas absorption line profiles at all atmospheric levels.

The model uses data on the stellar spectrum, planetary atmospheric composition and temperature, and surface and cloud properties as inputs, and computes wavelength-dependent radiative intensity and flux profiles, for both reflected and emitted light. From the computed specific fluxes, bolometric upwelling and downwelling stellar flux profiles can be calculated, and then used to generate the total broadband planetary albedo given the input stellar and surface albedo spectrum.

---

[3]http://www.cfa.harvard.edu/hitran/

2.2.1.b Model Inputs: Stellar Spectra

Earlier climate simulations explored the albedo effects of surface water ice on the climate of M-dwarf planets using a blackbody distribution to approximate incoming stellar radiation (Pierrehumbert, 2011). Here composite SEDs derived from observations and models of main-sequence stars of different spectral types were used to calculate broadband planetary albedos for a planet covered in specific surface types. We used F2V Star HD128167, K2V Star HD22049 (Segura et al., 2003), M3V star AD Leo[4] (Reid et al., 1995, Segura et al., 2005), and the solar spectrum obtained from Chance and Kurucz (2010). All stellar SEDs are shown normalized by their peak flux in Figure 1.3. For the SMART runs, all stellar spectra were adjusted so as to integrate to TOA solar constant values of between 1360 and ∼1380 W/m^2. For the GCM runs (see Section 2.2.2), the value of the solar constant was set to 1360 W/m^2 for all SEDs. This is equivalent to placing the model planets at the Earth's equivalent distance from their host stars. The zenith angle varies according to the diurnal cycle in the GCM, and in the SMART runs it is fixed at an average illumination value of 60°.

2.2.1.c Model Inputs: Surface Albedos

Previous EBMs have employed a broadband frozen surface albedo of 0.6 for M-dwarf star illumination (Pierrehumbert, 2011). Here, we carried out a more comprehensive analysis of the effect of incoming stellar radiation on the broadband frozen surface albedo, using high-resolution, wavelength-dependent albedo spectra for multiple water ice types, shown in Figure 1.4. We used spectra of albedo as a function of wavelength for fine-grained snow (Grenfell et al., 1994) and for blue marine ice (Warren et al., 2002). Bubbles in glacier ice result from air trapped in snow as it is compressed under the weight of overlying snow. The blue marine ice was not glacier ice; it resulted instead from freezing of liquid water. It contained few bubbles but numerous cracks, which were responsible for the albedo (see Figure 1.5). The cracks are caused by thermal stresses, so they would be present (and contributing to the albedo) even on a planet with no atmosphere (Stephen Warren, priv.

[4]http://vpl.astro.washington.edu/spectra/stellar/mstar.htm

comm.). Since these two ice types constitute end-members in terms of ice grain size and albedo at Earth-like surface temperatures and pressures, and ice may exist between these two states, wavelength-dependent albedo spectra have been modeled at 25%, 50%, and 75% mixtures of blue ice and snow (see Figure 1.4). Albedos for $\lambda < 0.31$ μm were decreased linearly from their values at 0.31 μm down to 0.05 at 0.15 μm for all ice and snow types.

As clouds also exhibit a wavelength-dependent reflectivity, in some cases reaching higher albedos than snow surfaces at longer wavelengths, the contribution of two major cloud types to the Earth's overall reflectivity is shown in Figure 2.3, and they are included in the SMART + EBM model validation in Section 2.2.1.d. Clouds, particularly low stratocumulus clouds, have the largest contribution to the Earth's reflectivity at the longest wavelengths of the shortwave spectrum (i.e. 1.5 - 2.5 μm), where the reflectivity of snow and high cirrus cloud drop significantly. An underlying snow surface is assumed in Figure 2.3, to highlight the contrast in the wavelength-dependent reflectivity between snow and clouds.

We used an ocean albedo spectrum obtained from Brandt *et al.* (2005). For wavelengths between 0.15 and 0.31 μm, albedos were calculated using the Fresnel equations, with indices of refraction of water from Segelstein (1981). Following Robinson *et al.* (2011), we obtained the spectrum for the clay mineral kaolinite (mixed with trace amounts of smectite and illite) from the United States Geological Survey (USGS) spectral library[5] for use as the bare land surface in the EBM simulations.

2.2.1.d Validation[6] of SMART + EBM Model

We validated the method of using SMART in combination with an EBM by reproducing the Earth's current ice line latitude (where "ice line latitude" is defined here as the farthest latitude towards the equator where ice is present on a planet's surface) and global mean surface temperature at its present obliquity, using outgoing infrared flux and diffusive heat

[5] http://speclab.cr.usgs.gov/spectral-lib.html

[6] The term "Validation" is generally used in the fields of astronomy and planetary science to mean the assessment of a model's performance compared to data taken from observations. The term "Evaluation" is used in atmospheric science for a similar undertaking, though inter-model comparisons may also be included (see e.g., Flato et al., 2013). We therefore use the former term here in the section where SMART is used with an EBM, and the latter term in the GCM section, with the understanding that their meanings are interchangeable.

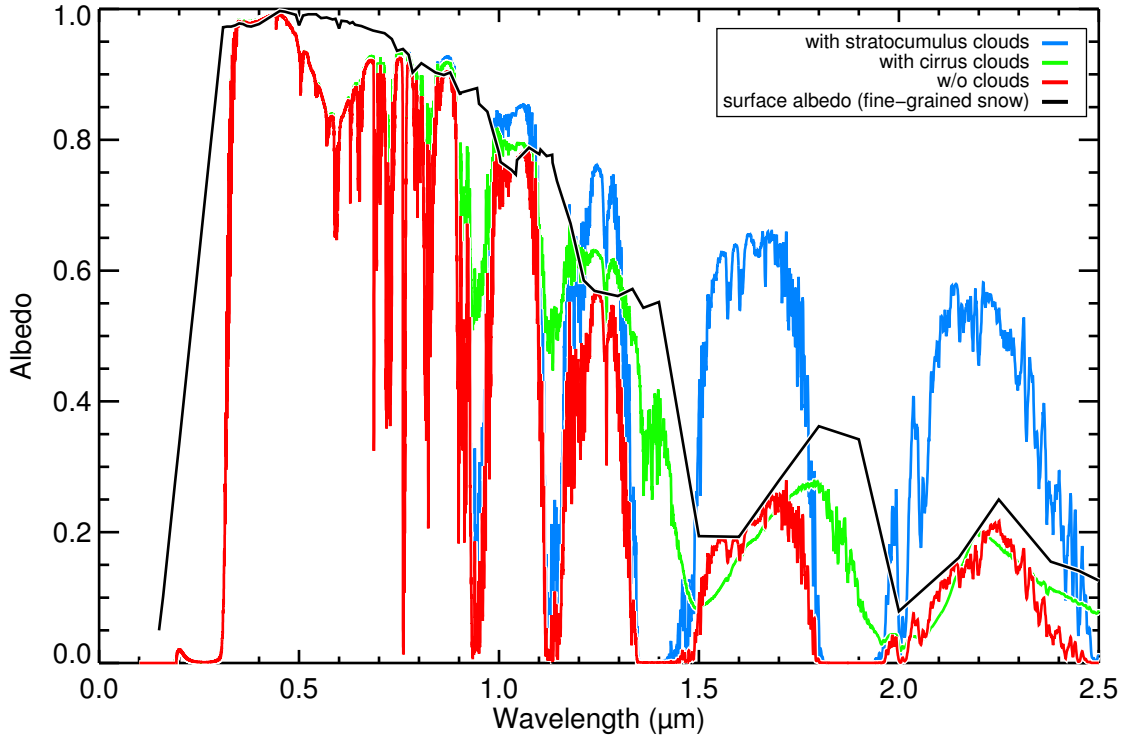

Figure 2.3 Wavelength-dependent reflectivity of a planet with an Earth-like atmosphere, an underlying snow surface, clearsky conditions (red), 100% cirrus cloud cover (green), and 100% stratocumulus cloud cover (blue), calculated using SMART. The empirical spectrum for fine-grained snow (from Figure 1.4) is plotted here (black) for reference.

transport parameterizations by North and Coakley (1979) and described here in Section 2.2.1. The maximum and minimum top-of-atmosphere (TOA) upward fluxes we calculated match observations from the Earth Radiation Budget Experiment (ERBE, Barkstrom & Hall, 1982) to within 6%. As described in Section 2.2.1.a, we used a temperature-pressure profile for the atmosphere derived using the ICRCCM program. Broadband planetary albedos for the surface types described in Section 2.2.1.c were generated assuming both clear and cloudy sky conditions. Approximately 64% of the Earth is covered in clouds (Warren & Hahn, 2002). Two cloud layers were used—that of low stratocumulus clouds and high cirrus clouds. For the purposes of my model, we assume 36% clear sky conditions, 40% low stratocumulus clouds, and 24% high cirrus clouds. Average broadband albedos over

ocean, land, and regions where the surface temperature falls below -2°C were calculated as described in Zsom *et al.* (2012):

$$\alpha_{avg} = \alpha_{cl} \times (1 - f_{st} - f_{cr} + f_{st}f_{cr}) + \alpha_{st} \times (f_{st} - f_{st}f_{cr}) + \alpha_{cr} \times (f_{cr} - f_{st}f_{cr}) + C_{ran} \times (f_{st}f_{cr}) \tag{2.7}$$

where α_{cl} is the albedo assuming clear sky conditions; α_{st} is the albedo assuming stratocumulus cloud covered conditions; α_{cr} is the albedo assuming cirrus cloud covered conditions; f_{st} and f_{cr} are the stratocumulus (0.40) and cirrus (0.24) cloud fractions, respectively; and $C_{ran} = f_{st} + f_{cr} - f_{st}f_{cr}$, the combined cloud fraction assuming random overlap, as given in Oreopoulos and Khairoutdinov (2003). An optical depth of 10 was used for both cloud types.

A modern land/ocean geographical configuration was used in the EBM. Areas over ocean and land surfaces were assigned broadband albedos of 0.32 and 0.41, respectively. Regions where the surface temperature fell below -2°C were assigned a broadband albedo of 0.46, which corresponds to the 25% mixture of blue marine ice and fine-grained snow in Figure 1.4. The EBM ice line latitude is 54.4°N, which is within six degrees of the Earth's northern hemisphere ice line latitude as defined as the southernmost tip of Greenland by Kukla (1979) and Mernild *et al.* (2010). The EBM global mean surface temperature (including zonal mean land and ocean temperatures) is 12°C, and is within three degrees of the global mean surface temperature of the Earth as defined as 15°C by Hartmann (1994). The EBM ice line latitude and global mean surface temperature (Figure 2.4) were calculated using only the surface types in Figure 1.4.

We have assumed a water vapor concentration equal to a mid-latitude average of 1% of the atmosphere at 1-bar surface pressure to calculate broadband planetary albedos used in our model validation. The amount of water vapor decreases rapidly with increasing latitude, and can be as much as 10 times lower at the poles (Hartmann, 1994). To test the sensitivity of our calculated albedos to water vapor, we ran SMART with 0.1% water vapor, and found our broadband albedos over land, ocean, and below-freezing surface types to increase by no more than 10% for ocean and ice surfaces, and 13% for our land spectrum.

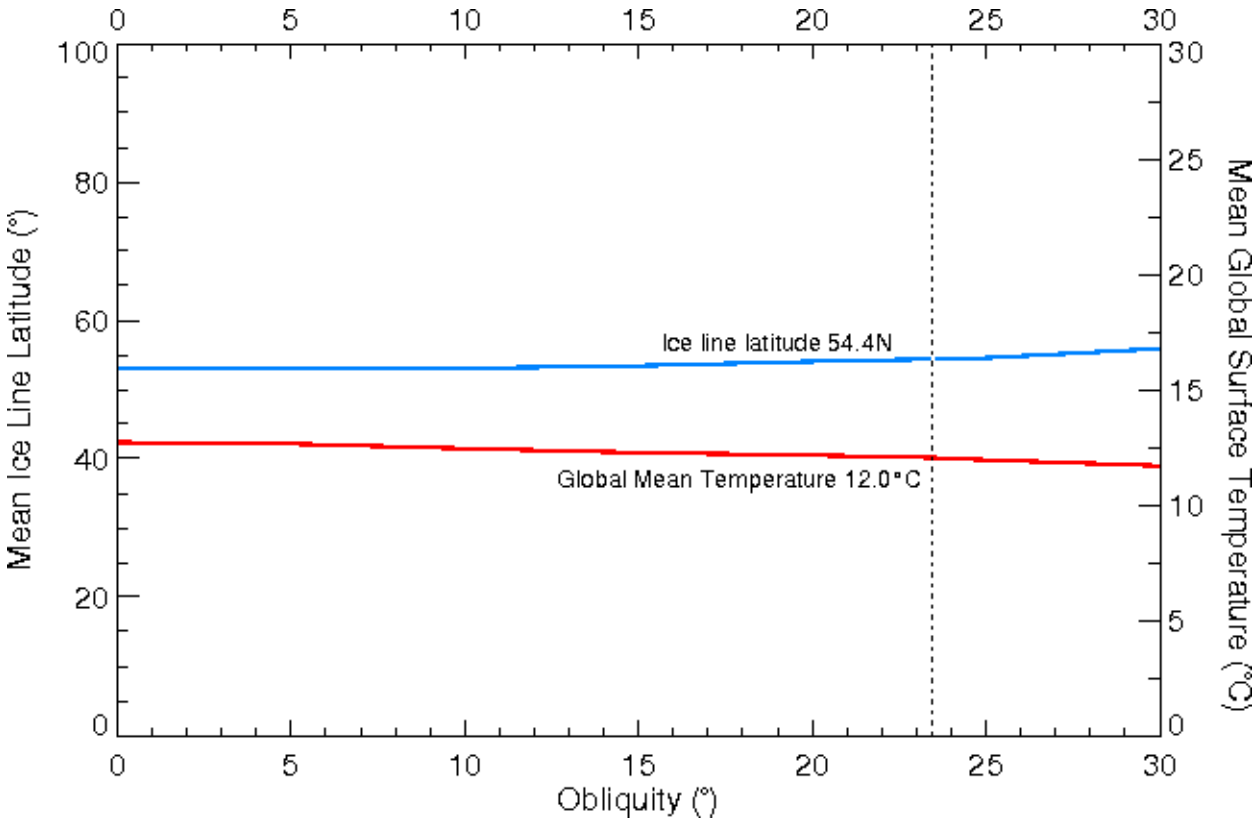

Figure 2.4 Mean ice line latitude (blue) and global surface temperature (red) as a function of obliquity, calculated using a seasonal EBM. The Earth's northern hemisphere ice line latitude and global mean surface temperature at its present obliquity of 23.5°C (vertical dashed line) is verified to within six degrees in latitude and three degrees Celsius, respectively. Ocean and land surfaces were assigned broadband albedos of 0.32 and 0.41, respectively (including atmosphere, for 36% clear sky, 40% stratocumulus cloud cover, and 24% cirrus cloud cover). Regions where the surface temperature fell below -2°C were assigned a broadband planetary albedo of 0.46, which was calculated using the same percentages of clear sky and cloud cover, with the spectrum corresponding to the 25% mixture of blue marine ice and fine-grained snow in Figure 1.4. Random overlap between the two cloud layers is assumed.

2.2.2 General Circulation Model

GCMs provide a 3-D representation of the global climate system, by dividing the planet into individual grid cells with horizontal (latitude-longitude) and vertical (height/pressure) components (Figure 2.5), and calculating average physical properties within each grid cell

based on the physics and dynamics (fluid motion) within the cell and due to interactions with other cells. GCMs allow for the simulation of changes in climate as a result of slow changes in boundary conditions, such as changes in the solar constant or greenhouse gas concentrations.

We used version 4.0 of the Community Climate System Model (CCSM4), a fully-coupled, global climate model developed to simulate past, present, and future climate states on the Earth (Gent et al., 2011). CCSM4 was run with a 50-meter deep, slab ocean (see e.g., Bitz et al., 2012). The slab ocean model normally has ocean heat flux convergence (often called a q-flux) input. We set this flux to zero, as done in experiments by Poulsen *et al.* (2001), though this does allow for a snowball transition at a higher instellation than if ocean dynamic heat flux, which tends to buffer against a snowball state, were incorporated (Poulsen et al., 2001; Pierrehumbert et al., 2011). The ocean is treated as static, but fully mixed with depth. Simulations that include a fully-dynamic ocean, though more realistic, can take thousands of model years to equilibrate for a given radiative forcing, and as such are too computationally expensive to allow for the exploration of a wide parameter space as we have done here.

CCSM4 consists of a dynamical core (a module governing primarily resolved scale processes), which numerically solves a series of nonlinear differential equations that describe atmospheric circulation through global fluid motions and transport. A finite difference method is used to evolve properties of fluid flow, by approximating derivatives of these properties as discrete, finite differences in their values over small units of time and space. Given here for a unit mass of fluid in motion, assuming a coordinate system that is fixed with respect to the Earth, these equations are mathematical representations of the following principles:

(1) Conservation of momentum:

$$\frac{d\vec{v}}{dt} = -\frac{1}{\rho}\vec{\nabla}p - \vec{g} + \vec{F}_{fric} - 2\vec{\Omega} \times \vec{v} \tag{2.8}$$

where $\frac{d}{dt}$ is the total (advective) derivative,

$$\frac{d}{dt} = \frac{\partial}{\partial t} + \vec{v} \cdot \vec{\nabla}$$

$\vec{v}$ is the vector describing the horizontal and vertical components of the velocity; $\vec{g}$ is the gravity vector; $\vec{F}_{fric}$ is the force per unit mass due to friction; $\vec{\Omega}$ is the angular velocity of the Earth ($-2\vec{\Omega} \times \vec{v}$ is the Coriolis force); p is the pressure, and ρ is the density.

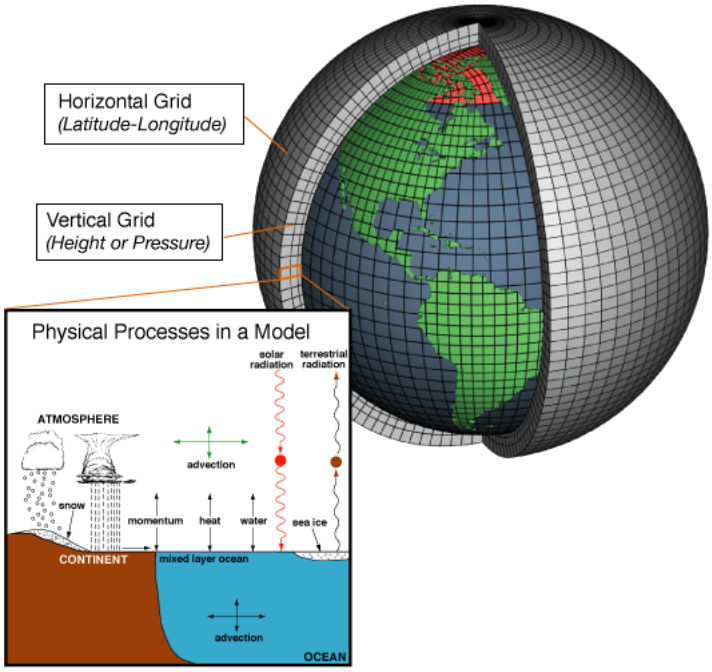

Figure 2.5 Schematic diagram of a 3-D general circulation model[7]. The planet is divided into horizontal and vertical grids, and individual properties of the climate system are evaluated within each grid cell.

(2) Mass continuity:

$$\frac{\partial \rho}{\partial t} = -\vec{\nabla} \cdot (\rho \vec{v}) \tag{2.9}$$

(3) Conservation of energy (the first law of thermodynamics):

$$Q = C_p \frac{dT}{dt} - \frac{1}{\rho} \frac{dp}{dt} \tag{2.10}$$

where Q is the heating rate per unit mass; T is the temperature; and C_p is the specific heat capacity, as in equations (2.1) and (2.2).

[7] http://celebrating200years.noaa.gov/breakthroughs/climate_model/

(4) Equation of state for the atmosphere, which relates ρ, p, and T:

$$p = \rho RT \tag{2.11}$$

where R is the ideal gas constant.

To solve these equations, the heating rate must be specified, which requires a detailed analysis of radiative transfer within the atmospheric column, given the shortwave and longwave radiation balance. The radiation scheme CCSM4 uses to determine the heating rate is described below. Radiative transfer, along with the influences on heat and energy transfer of clouds, evaporation-precipitation-condensation and related processes, and convection constitute the "physics" of the model, while the equations in (2.8)-(2.11) describing fluid motion and transport comprise the model "dynamics".

In solving these basic, or primitive Eulerian equations of motion, GCMs apply two key assumptions: (1) That the effects of changes in the vertical density on the mass balance of the continuity equation, and on the frictional force term in the momentum equation, are negligible (a "quasi-Boussinesq" approximation), thus filtering out sound waves in the atmosphere, which change on timescales much smaller (seconds) than the typical time step in GCMs ($\sim$15 minutes); and (2) that the horizontal scale of motions is much larger than the vertical scale, which is a reasonable approximation given that the height of the fluid layer (the atmosphere) is much smaller compared to the radius of the Earth. We can therefore neglect to first order any changes in the gravitational acceleration g with height z, and approximate the vertical component of (2.8) as the equation of hydrostatic balance, with the vertical pressure gradient equal to the density multiplied by gravity ($\frac{dp}{dz} = -\rho g$). This essentially amounts to setting the vertical components of the velocity ($\frac{dv_z}{dt}$), drag (F_{fric_z}), and the Coriolis force ($-2\Omega_z \times v_z$) equal to zero in (2.8), which is reasonable given that outside of areas where there is strong convection, $v_z << v_x, v_y$. This is referred to as the hydrostatic approximation, and can generally be applied when the horizontal scale of atmospheric motions is greater than 10 km (Holton, 2004).

GCMs often use a sigma coordinate system. Sigma coordinates are vertical coordinates,

and follow the topography of the Earth by scaling the local atmospheric pressure to the local surface pressure. Surface pressure can vary widely across the planet, particularly for topographic surfaces that are significantly above sea level. The vertical coordinate σ is therefore defined as a ratio:

$$\sigma = \frac{p}{p_s} \tag{2.12}$$

where p_s is the surface pressure at a particular point on the Earth. A sigma scale that is divided equally results in vertical layers of equal thickness above each surface point. Using sigma coordinates therefore allows GCMs to represent lower boundary conditions more smoothly and with greater resolution. CCSM4 uses a hybrid coordinate system, which uses these terrain-following sigma coordinates, as well as pressure levels in the upper atmosphere.

The atmospheric component to CCSM4 is the Community Atmosphere Model version 4 (CAM4). CAM4 divides the incident shortwave (stellar) radiation into twelve wavelength bands, given in Table 2.1. The percentage of the total flux from the star is specified in these wavelength bands, with a significantly higher percentage of total stellar flux at longer wavelengths (94.6% for M-dwarf star AD Leo, vs. 52.8% for the Sun, and 40.7% for F-dwarf star HD128167 in waveband 10). As AD Leo emits non-negligible amounts of radiation at wavelengths shortward of 0.2 μm and longward of 5.0 μm, the percentages of flux in these regions were folded into the shortest (Band 1) and longest (Band 10) wavebands, respectively, to include the full stellar spectrum.

A model atmosphere in CAM4 is divided into a series of vertical layers, each bounded by layer interfaces. Radiative heating rates are then determined for each layer. The percentages of downwelling stellar radiation in each of the spectral bands are specified, as well as the cosine of the stellar zenith angle. Each layer is assumed to be vertically and horizontally homogeneous, and to contain a combination of atmospheric constituents such as CO_2, H_2O, O_2, and O_3, which absorb and/or scatter radiation according to their individual properties, defined in terms of extinction optical depth, single-scattering albedo, asymmetry parameter, and forward scattering fraction. Scattering by water cloud droplets is also included.

The radiative transfer scheme uses the δ-Eddington approximation (Joseph et al., 1976), which involves approximating the scattering phase function (the angular distribution of

Table 2.1 CAM4 spectral wavelength bands specifying shortwave (stellar) incoming flux into the atmosphere, and the percentage of flux within each waveband for the Sun, M-dwarf star AD Leo, and F-dwarf star HD128167.

Band	λ_{min}	λ_{max}	Sun % flux	AD Leo % flux	HD128167 % flux
1	0.200	0.245	0.124	0.025	3.291
2	0.245	0.265	0.130	0.009	0.717
3	0.265	0.275	0.177	0.0029	0.597
4	0.275	0.285	0.167	0.008	0.528
5	0.285	0.295	0.349	0.003	0.763
6	0.295	0.305	0.399	0.004	0.917
7	0.305	0.350	2.805	0.029	4.620
8	0.350	0.640	36.00	3.390	43.12
9	0.640	0.700	6.643	1.895	6.220
10	0.700	5.000	52.79	94.64	40.68
11	2.630	2.860	0.613	1.783	0.393
12	4.160	4.550	0.175	0.749	0.114

radiation at a given wavelength that is scattered by a particle) as a combination of a delta function and a two-term approximation. This approximation addresses the difficulty of solving the radiative transfer equation for highly asymmetric phase functions—such as those due to the strongly forward-peaked scattering of cloud droplets—by approximating the forward peak as a delta function, and specifying the fraction of scattering into the forward peak as proportional to the square of the phase function asymmetry parameter. The δ-Eddington solution to the equation of radiative transfer is faster and more accurate than the Eddington and the two-stream approximation, which employ more generalized approximations to address the angular dependence of radiation intensity (Joseph et al., 1976).

Unlike in line-by-line radiative transfer codes such as SMART, where the contribution of each spectral line for each atmospheric gas to the flux within a given wavelength range is calculated, in the δ-Eddington approximation available absorption data for atmospheric gases is adjusted for the spectral intervals in Table 1, and using mass mixing ratios for these gases in Earth's atmosphere, absorption coefficients (also called "k-coefficients") are calculated for each spectral interval. These k-coefficients are then used to generate absorption

optical depths, and with these the δ-Eddington solution is calculated for the reflectivity and transmissivity within a given layer. Upward and downward fluxes within each layer are calculated for each stellar flux band, given the absorption and scattering properties of each gas present in the layer. These fluxes are then summed up across layers in each spectral interval to generate the spectrally integrated (broadband) fluxes. Broadband fluxes are differenced across layers to determine the stellar heating rate (Briegleb, 1992). As such, CCSM4 is most accurate for use in modeling atmospheres similar to the Earth's, given that the k-coefficients used in the radiation scheme depend on Earth's mass mixing ratios for constituent gases.

We have assumed an Earth-like atmospheric composition for CO_2, H_2O, and O_2. The ozone profile has been set to zero, as we were concerned primarily with surface temperature as a measure of planetary habitability, and have found the presence of ozone to have a negligible effect on the surface temperature of M- and G-dwarf planets (Shields et al., 2013). F-dwarf planets may exhibit colder surface temperatures and greater ice extent with ozone in their atmospheres than without, possibly as a result of greater stratospheric heating in F-dwarf planet atmospheres (Segura et al., 2003) preventing more shortwave radiation from reaching the surface.

The sea ice component is the Los Alamos sea ice model CICE version 4 (Hunke & Lipscomb, 2008), except we have made the ice thermodynamic only (no sea-ice dynamics, which may affect the snowball transition, Abbot et al., 2011), and have reverted back to the sea-ice albedo parameterization from CCSM3. The latter change was made because the newer δ-Eddington, multiple scattering albedo parameterization is much more difficult to control. In the CCSM3 albedo parameterization, the surface albedo is divided into two bands, visible ($\lambda \leqslant 0.7$ μm) and near-IR ($\lambda > 0.7$ μm). Default near-IR and visible wavelength band albedos are 0.3 and 0.67 for cold bare ice and 0.68 and 0.8 for cold dry snow. The albedos decrease modestly as the surface approaches the melting temperature to mimic the effect of melt ponds. The CCSM3 cold bare ice albedo is approximately halfway between the two end-members for blue marine ice and snow in Figure 1.4, while the CCSM3 cold dry snow albedo is between the brightest end-member, and 3/4 of the way towards the brightest end-member in Figure 1.4. We used the default near-IR and visible

band albedos for all simulations except the surface sensitivity tests described in Chapter 3. However, near-IR and visible band ice albedos calculated using our ice and snow spectra and weighted by the M-dwarf SED are higher than the default values by 3.3% and 1.5%, respectively, higher by 21% for the visible band snow albedo, and lower by 23% for the near-IR snow albedo. An implicit error therefore must exist within this range as a result of using the default GCM two-band model, and may affect the exact values of temperature and ice extent calculated for different SEDs. But as the spectral dependence of ice and snow albedo is still captured in the two-band model, the general trends shown here are expected to be robust.

Coupled GCMs are crucial to understanding the full planetary response to changes in radiative and surface forcing. This is demonstrated in Figure 2.6, where the TOA absorbed shortwave radiation minus OLR as a function of latitude in an EBM is compared with that in a GCM for a G-dwarf planet receiving 100% of the modern solar constant. When averaged over a few years or more, the net incoming heat flux must be equal to the divergence of heat from each grid cell in order to yield a net surface flux of zero locally and globally in our slab ocean model. The EBM shows a large jump in the net incoming heat flux near the poles, due to the abrupt change in albedo for ice-covered areas in the EBM, and the lack of parameterized clouds (beyond our SMART treatment). This large jump causes the ice line to be unstable and collapse to the equator at significantly higher latitudes in the EBM compared to the GCM. A smoother transition in net incoming heat flux as a function of latitude is visible in the GCM, due to the presence of full-scale atmospheric dynamics, including clouds.

The GCM was run on four intel Xeon hex core chips at 2.27 GHz, giving $\sim$11 simulation years per wallclock day. For each simulation in the warm-start runs in Chapter 3, the model was run for 37 years to equilibrate to the modern Earth climate at present solar instellation. We then ran our simulations for 40 years after that, with decreasing instellation with the SED from either the Sun (a G-dwarf star), an M-dwarf star, or an F-dwarf star. In Chapter 6, we also ran 30-40-year simulations with the SED from a K-dwarf star with a similar photospheric temperature to Kepler-62, to explore the possible climate of the potentially habitable planet Kepler-62f. The cold-start runs in Chapter 4 were started with the ice-

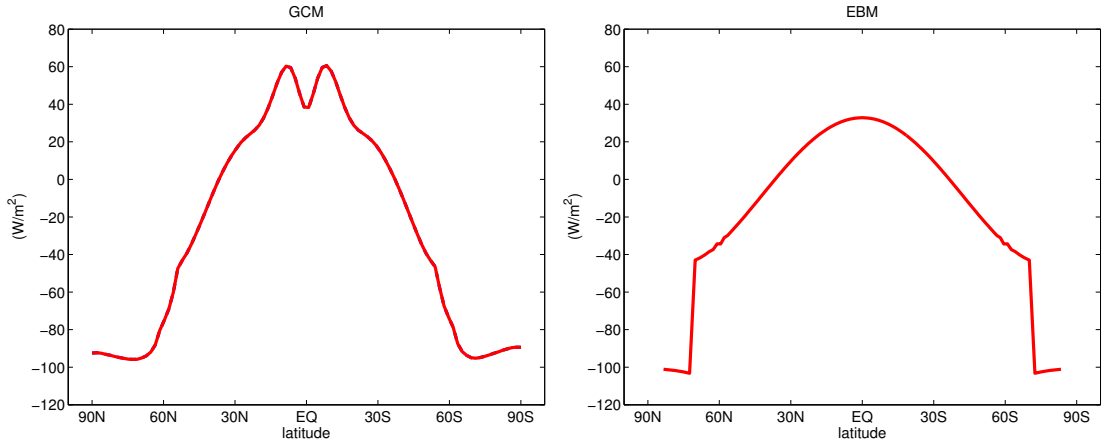

Figure 2.6 TOA absorbed shortwave radiation minus OLR as a function of latitude, calculated in the GCM (left) and the EBM (right) for a G-dwarf planet receiving 100% of the modern solar constant. When averaged over a few years or more, the net incoming heat flux must be equal to the divergence of heat from each grid cell in order to yield a net surface flux of zero locally and globally in our slab ocean model. The EBM shows a large jump in the net incoming heat flux near the poles, due to the abrupt change in albedo for ice-covered areas in the EBM, and lack of parameterized clouds (beyond our SMART treatment). A smoother transition in net incoming heat flux as a function of latitude is visible in the GCM, due to the presence of full-scale atmospheric dynamics, including clouds.

covered (snowball) climate state found at the end of the warm-start runs, and the instellation was then increased over 40 years of simulation. We ran select simulations for an additional 50 years to ensure equilibration of the ice extent. We also ran simulations of M- and G-dwarf snowball planets with an atmospheric CO_2 concentration of 10%. Assuming the CO_2 weathering feedback on a snowball planet still operates, we compare the planetary response to high amounts of CO_2 as a function of host star SED.

2.2.2.a Evaluation of CCSM4

Figure 2.7 shows a schematic diagram of the basic energy balance of the Earth, using data supplied by Kiehl & Trenberth (1997), compared with one using output generated by our GCM runs assuming an aqua planet orbiting the Sun with Earth's present instellation (1360 W/m^2). Values calculated by CCSM4 for total reflected solar radiation, radiation absorbed by the atmosphere and surface, and outgoing longwave radiation differ by less

than 6% compared to widely accepted values. Greater differences in individual surface and atmosphere contributions to the total reflected solar radiation are due largely to the aqua planet approximation used in our GCM runs, which results in increased cloudiness at most heights relative to modern Earth's geography, and a higher contribution by clouds to the total reflected solar radiation. Based on this model validation, we use similar data from GCM runs with different host stars in our analysis of the effect of host star SED on planetary energy balance and climate in Chapter 3.

2.2.2.b Implications for Planets Orbiting Different Stars

Figure 2.8 shows schematic diagrams of the global energy balance of an aqua planet orbiting a G-dwarf star, an F-dwarf star, and an M-dwarf star at equivalent stellar flux distances. Though all planets receive the same instellation from their host stars (100% of the modern solar constant), the SEDs of the incoming radiation differ greatly for these three types of stars. The F-dwarf host star emits a larger fraction of its radiation at visible and near-UV wavelengths than the G-dwarf star (the Sun), while the M-dwarf star emits predominantly in the near-IR (see Figure 1.3). As discussed in Section 1.3.1, the interaction between the stellar SED and an orbiting planet's atmosphere and surface will affect the manner in which the planet achieves global energy balance through a combination of reflected, absorbed, and/or emitted shortwave and longwave radiation. For instance, as shown in Figure 2.8, the M-dwarf planet absorbs much more incoming stellar radiation than the other two planets, while the F-dwarf planet reflects much more radiation. As we shall see in Chapters 3 and 4, this has important implications for how the surface temperature and climate differ and will evolve over time for these planets, and reveals mechanisms that could allow planets to use their unique star-planet interactions to compensate for changes in stellar flux or atmospheric composition.

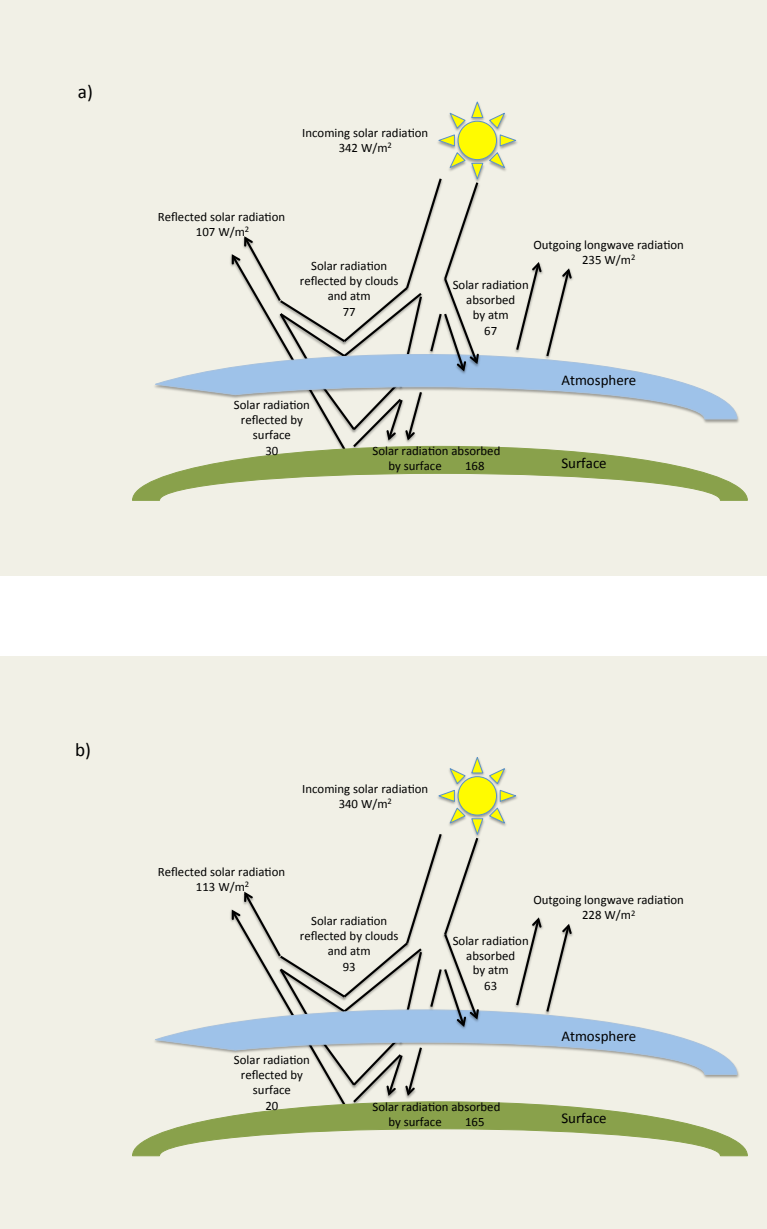

Figure 2.7 Schematic diagram of Earth's global energy balance, based on a diagram by Hartmann (Hartmann, 1994) using a) data supplied by Kiehl & Trenberth (1997), and b) model output from our aqua planet simulation with a GCM (CCSM4). Values calculated by CCSM4 for total reflected solar radiation, radiation absorbed by the atmosphere and surface, and outgoing longwave radiation differ by less than 6%.

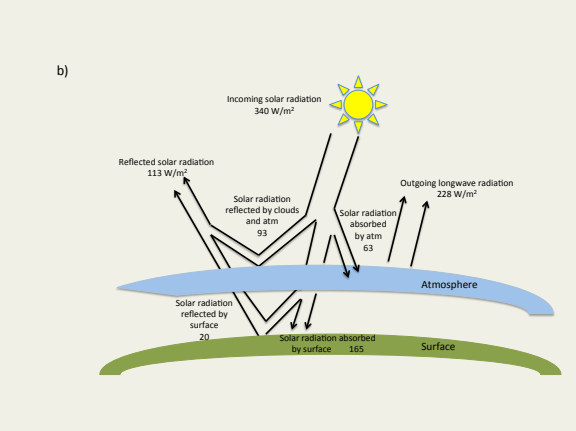

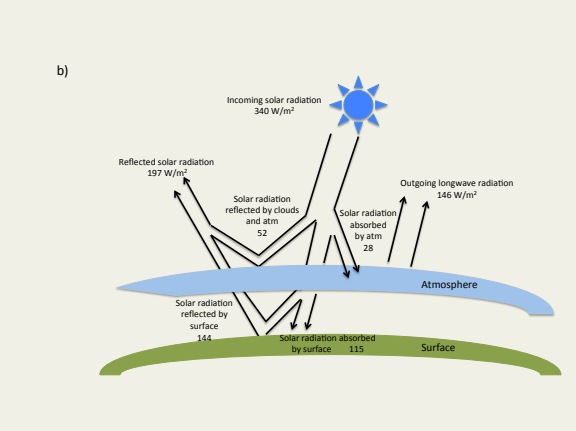

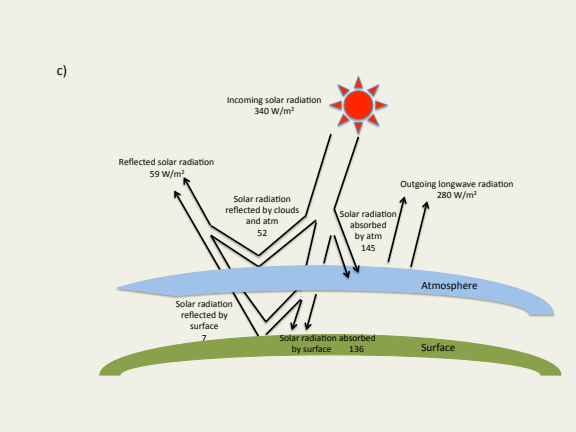

Figure 2.8 Schematic diagram of global mean energy balance for an aqua planet orbiting a) the Sun, as in Fig. 2.7b, b) an F-dwarf star, and c) an M-dwarf star. All planets receive equivalent instellation (100% of the modern solar constant), here globally averaged (340 W/m^2).

Chapter 3

APPLICATION I: ENTRANCE INTO A SNOWBALL STATE

In this chapter, the SMART + EBM model as well as a GCM were used to explore the specific interaction of a host star's spectrum with its planet's surface and atmosphere, and the effect of this interaction on the transition into a snowball state for planets orbiting stars of different spectral types. These simulations allowed us to quantify the effect of stellar SED, ice grain size, and CO_2 concentration on planetary albedo and climate for planets in different stellar environments, and to identify classes of planets that may be less susceptible to snowball episodes given the spectral class of their host stars. Portions of this chapter were originally published in collaboration with V. S. Meadows, C. M.. Bitz, et al. in the August 2013 edition of the journal Astrobiology (Shields et al., 2013, *Astrobiology*, Vol. 13, pp. 715-739;), and are reproduced below with the permission of Mary Ann Liebert, Inc.

3.1 Introduction

A crucial task on the road to identifying a habitable world beyond our Solar System is distinguishing planets that are more likely to support climates conducive to the long-term presence of surface liquid water from those that may be more volatile in terms of their climate stability. Planets less likely to experience extreme climate events may be more attractive candidates for target selection for future follow-up missions focused on the characterization of their atmospheres and the identification of possible biosignatures (atmospheric fingerprints of biological processes that may indicate the presence of life on a planet's surface).

It has been understood for some time that because of the large amount of near-IR radiation emitted by their host stars, M-dwarf planets are likely to have lower planetary albedos given the presence of atmospheric CO_2 and water vapor, which absorb strongly in the near-IR, and due to the more negligible effect on planetary albedo of Rayleigh scattering, which is stronger for shorter, bluer wavelengths of radiation (Kasting et al., 1993; Selsis

et al., 2007; Kopparapu et al., 2013a,b). The lower the planetary albedo, the more energy is absorbed on the planet, as shown in Eqn. (1.1). Thus a lower planetary albedo can lead to a warmer planetary climate.

However, planetary climate can also be affected by the interaction of the host star spectral energy distribution with the wavelength-dependent reflectivity of ice and snow, in addition to atmospheric gases. Given the dependence of ice and snow albedo on wavelength, and the large difference in the distribution of spectral energy for different types of stars (see Figure 1.3), the interaction between the SED of M-dwarf stars and the icy or snowy surfaces that may exist on their orbiting planets will differ greatly from that of G- and F-dwarf stars and their planets' ice surfaces. Additionally, on M-dwarf planets, a significant amount of radiation emitted by the host star is absorbed by atmospheric gases such as CO_2 and water vapor, and this will affect the manner in which heat is transferred through the atmosphere. It has been proposed that M-dwarf planets may be less susceptible to snowball states, and that the outer edge of the habitable zone could be wider for M-dwarf stars, due to the large percentage of near-IR radiation emitted by these stars, which is more strongly absorbed by ice, snow, and atmospheric gases on these planets (Joshi & Haberle, 2012).

Joshi and Haberle (2012) speculated that the outer edge of the habitable zone, which they define as the orbital distance at which carbon dioxide condenses out onto the surface of a planet, may be as much as 30% farther out for M-dwarf stars than originally calculated, given the spectral dependence of water ice and snow albedo. This work was purely analytical, using synthetic stellar and blackbody spectra, one surface water ice type and one snow type to show that broadband albedos are likely lower for M-dwarf planets. Neither radiative transfer through an atmosphere, nor the effect of clouds, were included in these calculations. The effect of near-IR CO_2 and water vapor absorption was estimated using a constant scaling factor at wavelengths beyond 1.5 μm.

At the very outer limit of the habitable zone, atmospheric CO_2 content is expected to be high as a result of decreased silicate weathering (Walker et al., 1981). As the maximum greenhouse limit for CO_2 (more than $\sim$2 bars, Pierrehumbert, 2010) is approached, planetary albedo becomes dominated by the thicker CO_2 atmosphere. This high amount of atmospheric CO_2 could reduce climate sensitivity to surface ice albedo. This possibility

has not previously been investigated. The exact CO_2 concentration required to mask the climatic effect of the interaction between host star SED and surface ice and snow has not been constrained.

Here, we provide a more comprehensive study of the interaction between host star SED and an orbiting planet's atmosphere and surface, using a hierarchical approach. We use SMART to calculate broadband planetary albedos assuming different incident stellar spectra, a wide range of ice and snow surface types, and land and ocean as input to a seasonally-varying, 1-D EBM. With the EBM we explore the latitudinal extent of the ice line, and thus what fraction of the planet is ice-covered, as a function of incident stellar and surface albedo spectrum. Using SMART, with spectrally-resolved absorption coefficients for CO_2, we determine the atmospheric CO_2 concentration necessary to mask surface ice-albedo feedback effects entirely.

The manner in which radiative transfer through atmospheric gases is treated can affect the EBM results. To address these effects, we run a 3-D atmospheric GCM (CCSM4) coupled to a motionless 50m-depth "mixed-layer" ocean with a thermodynamic sea ice model. There is no land, and hence it is referred to as an aqua planet. We vary the SED of the instellation in order to investigate the climate of a hypothetical planet of a host M-dwarf star, and compare it to the climate of an aqua planet orbiting the Sun, a G-dwarf star, as well as an F-dwarf star, which emits a greater fraction of visible and near-UV radiation. We also describe how changes to the surface albedo parameterization in the GCM affect the climate of an M-dwarf planet. And we discuss implications of the results of our climate model simulations for M-dwarf habitability, given the effect of host star SED on climate sensitivity.

3.2 Results

3.2.1 SMART + EBM

We used SMART to comprehensively address the radiative transfer that takes place between a planet's ice, ocean, and land surfaces and the incident stellar radiation. Derived broadband planetary albedos used as input to the EBM are therefore unique to the planet-star system, rather than broadly generalized. Here we first explore the contributions to broadband

planetary albedo for different surface types, atmospheric pressures, and stellar SEDs. We then explore climate-sensitivity to changes in instellation, surface type, and ice grain particle size for Earth-like planets orbiting stars of different spectral type.

3.2.1.a Contributions to Broadband planetary albedo

Figure 3.1 shows broadband planetary albedos that are output from SMART, given various surface types. We are primarily interested in quantifying the effects of surface albedo on planetary climate, and used the aqua planet EBM as a testbed for identifying general trends. Broadband planetary albedos decrease monotonically with stellar luminosity, even though all stellar spectra have been adjusted to provide the same integrated flux as that received by the Earth around the Sun. This can be explained by the larger fraction of spectral energy emitted at $\lambda > 1.0$ μm for stars with lower luminosities. These broadband planetary albedos incorporate the wavelength-dependent reflectivity of the underlying surface. At these longer wavelengths, ice and snow absorb strongly (Figure 1.4), resulting in a lower average surface albedo contribution to the overall planetary albedo.

Since Rayleigh scattering is stronger at shorter wavelengths due to the $1/\lambda^4$ cross-section dependence, it is expected to be more pronounced on an F-dwarf planet than on other host star planets, and can result in higher broadband planetary albedos (Kasting et al., 1993; Pierrehumbert, 2011; Kopparapu et al., 2013a,b). To verify the trend stated above, we reduced the atmospheric pressure in additional SMART runs with an F-dwarf spectrum incident on an ocean surface, and excluded atmospheric gases. We confirm that the Rayleigh scattering tail present at $\lambda < 0.7$ μm for atmospheres with 1 bar surface pressure is virtually absent for thin atmospheres of less than 0.1 mb (Figure 3.2). The resulting broadband albedos in the "no Rayleigh scattering" case are plotted in Figure 3.1 (middle column). Even with Rayleigh scattering removed, Figure 3.1 reveals higher broadband planetary albedos with ice and snow surfaces for the F-dwarf host star, and the lowest broadband albedos for the M-dwarf host star. Also plotted are broadband planetary albedos calculated with Rayleigh scattering only (no atmospheric gas absorption, left column), and with both Rayleigh scattering, atmospheric gases, and clouds included (right column). These values for each stellar type are listed in Table 3.1.

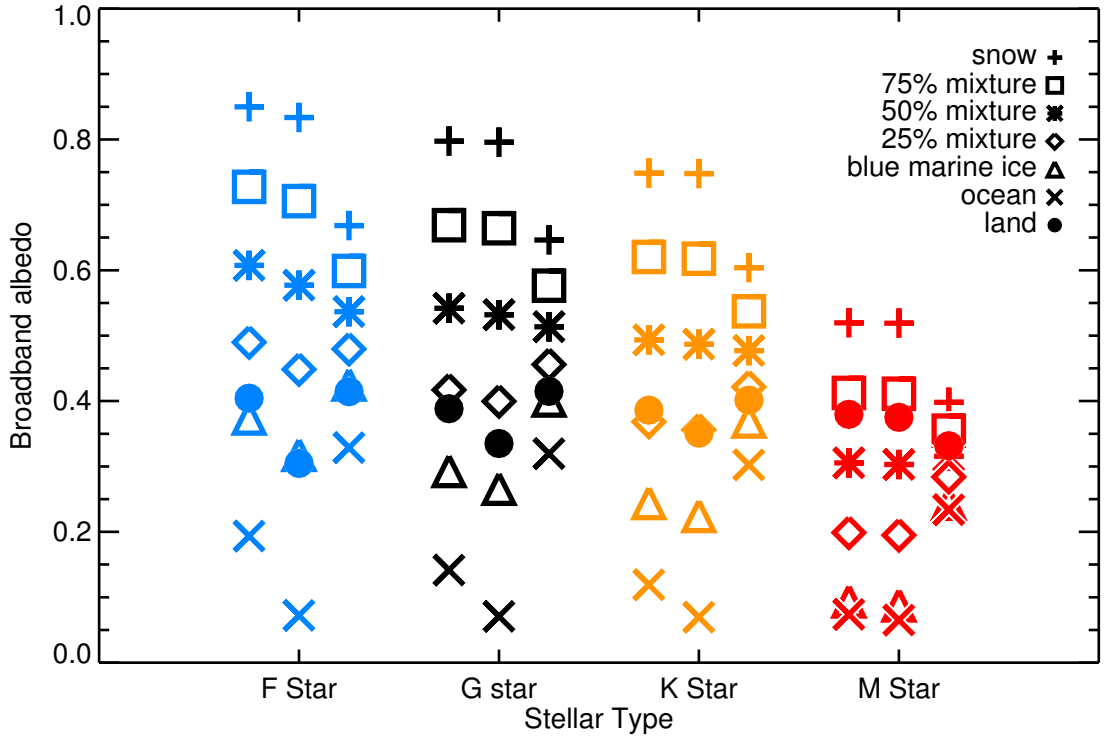

Figure 3.1 Broadband planetary albedos calculated with upwelling and direct downwelling stellar flux outputs from SMART for ice, snow, ocean, and land surfaces given the SEDs of F-, G-, K-, and M-dwarf stars. For each star: Left – no atmospheric gas absorption, but Rayleigh scattering is included; middle – no gases or Rayleigh scattering (broadband F-dwarf planetary albedos for ice and snow surfaces are still larger than those for G-, K-, or M-dwarf planets, even after the effects of Rayleigh scattering are removed); right – Rayleigh scattering, gas absorption, and clouds are included. These values are listed in Table 3.1.

3.2.1.b Climate sensitivity for Earth-like planets

Broadband planetary albedos calculated from SMART (with an Earth-like atmospheric composition and distribution of clouds) were used as input to the EBM, as described in Chapter 2 (Section 2.2.1.d). Below-freezing surfaces encountered during the EBM runs (where the temperature is less than -2 degrees Celsius) were given broadband planetary albedos for ice and snow of varying grain size calculated from SMART at 1 bar surface pressure. EBM simulations were run with an initial warm start, with an approximate

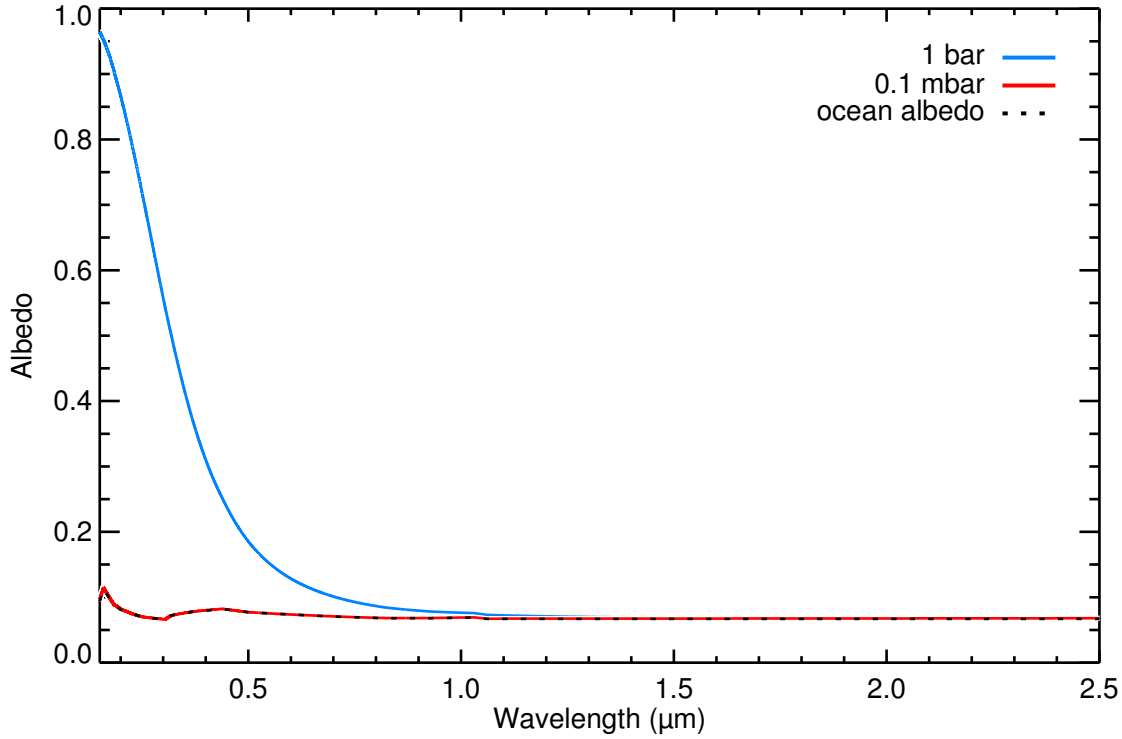

Figure 3.2 Top-of-the-atmosphere (TOA) upwelling flux divided by the downwelling stellar flux (which is a measure of the planetary albedo) as a function of wavelength, for an ocean-covered planet with a surface pressure of 1 bar (blue), and 0.1 mbar (red) orbiting an F-dwarf star at an equivalent flux distance to the Earth around the Sun, calculated using SMART. No atmospheric gas absorption is included here. The rise in TOA flux (and therefore planetary albedo) evident in the 1-bar atmosphere case at $\lambda < 0.7$ μm is due to Rayleigh scattering. At 0.1 mb, the Rayleigh scattering tail is absent, and matches the empirical albedo spectrum of the ocean surface from Figure 1.4 (dotted black).

Earth-like zonal mean temperature distribution. The global mean surface temperature and mean latitude of the ice line in the northern hemisphere were calculated at present Earth obliquity (23.5°) as a function of percent of modern solar constant, with 100% of the modern solar constant being the present amount of solar instellation, or flux density, on the Earth. The results are plotted in Figure 3.3, and can be assumed to be similar for the southern hemisphere, given an assumed eccentricity of zero. The slope of each line is a measurement of the climate sensitivity of the planet to changes in instellation. The smaller the grain size

Table 3.1 Broadband planetary albedos calculated with upwelling and direct downwelling stellar flux outputs from SMART for fine-grained snow, large-grained blue marine ice, ice of intermediate density between the two end-members, ocean, and land surfaces, given the SEDs of F-dwarf star HD128167, the Sun (a G-dwarf star), K-dwarf star HD22049, and M-dwarf AD Leo. For the planetary albedos that include gases and clouds (right column), average broadband albedos were calculated as described in Zsom *et al.* (2012) assuming 64% cloud cover (Warren et al., 2002), with 40% low stratocumulus clouds and 24% high cirrus clouds. Random overlap between the two cloud layers is assumed (Oreopoulos & Khairoutdinov, 2003).

Stellar Type	surface	No gases or clouds Rayleigh scattering on	No gases or clouds Rayleigh scattering off	Earth-like gases, clouds Rayleigh scattering on
F-dwarf	snow	0.84988	0.83361	0.66833
	75%	0.72756	0.70568	0.59884
	50%	0.60744	0.57704	0.53664
	25%	0.48993	0.44840	0.47961
	blue ice	0.37330	0.31782	0.42542
	ocean	0.19349	0.07221	0.32865
	land	0.40438	0.30470	0.41428
G-dwarf	snow	0.79724	0.79577	0.64622
	75%	0.66882	0.66421	0.57636
	50%	0.54191	0.53194	0.51363
	25%	0.41708	0.39966	0.45585
	blue ice	0.29312	0.26603	0.40093
	ocean	0.14155	0.07070	0.31948
	land	0.38829	0.33513	0.41484
K-dwarf	snow	0.74842	0.74784	0.60392
	75%	0.62041	0.61768	0.53716
	50%	0.49350	0.48685	0.47708
	25%	0.36822	0.35602	0.42150
	blue ice	0.24418	0.22435	0.36870
	ocean	0.11921	0.06965	0.30235
	land	0.38606	0.35098	0.40133
M-dwarf	snow	0.51963	0.51905	0.39800
	75%	0.41245	0.41125	0.35478
	50%	0.30542	0.30308	0.31546
	25%	0.19890	0.19491	0.28406
	blue ice	0.09361	0.08749	0.24317
	ocean	0.07390	0.06518	0.23372
	land	0.37974	0.37516	0.33165

of the ice (and therefore the higher the albedo), the farther towards the equator the ice advances. For stars with higher visible and near-UV output, ice-covered planetary states occur with smaller decreases in instellation. Cooler, redder stars allow planets to remain free of global ice cover with larger decreases in instellation. An alternate branch of these results exists with significant ice cover if an initial cold start is assumed, with zonal mean temperatures characteristic of a snowball state. We explore that branch in Chapter 4.

3.2.2 GCM simulations

1-D EBMs offer insight into the latitudinally-resolved distribution of temperature and ice across a planet. However, they heavily parameterize atmospheric radiative transfer and eddy heat transport. Furthermore, ours only captures the albedo effects of sea ice (not the insulating effect). To test the robustness of the results from our EBM simulations, and to provide further physical insight into the contribution of atmospheric dynamics to planetary climate, we employed a coupled atmospheric GCM with more complete sea ice physics.

We begin our analysis of GCM simulations by characterizing how the global climate depends on the stellar constant for an aqua planet orbiting the Sun or an M-or F-dwarf star. Then we describe the climates in greater detail for an aqua planet around the Sun and an M-dwarf star, where we consider runs with similar temperate climates but vastly different SEDs, followed by stellar constants that give similar snowball climates. We explore the role played by atmospheric dynamics in generating similar ice-covered states, given the different stellar SEDs. Finally, we investigate the sensitivity of planetary climate to surface albedo alone.

3.2.2.a Climate sensitivity: G-dwarf vs. M-dwarf and F-dwarf planets

Figure 3.4 shows the latitudinal ice extent and annual global mean surface temperature in the northern hemisphere as a function of percent of modern solar constant for a G-dwarf aqua planet with an incident spectrum of the Sun, an M-dwarf aqua planet with the incident spectrum measured for AD Leo, and an F-dwarf aqua planet with the incident spectrum measured for HD128167. As we have assumed an eccentricity of zero in our GCM runs, an obliquity of 23°, and no land surface, the temperature and ice behavior are symmetric in

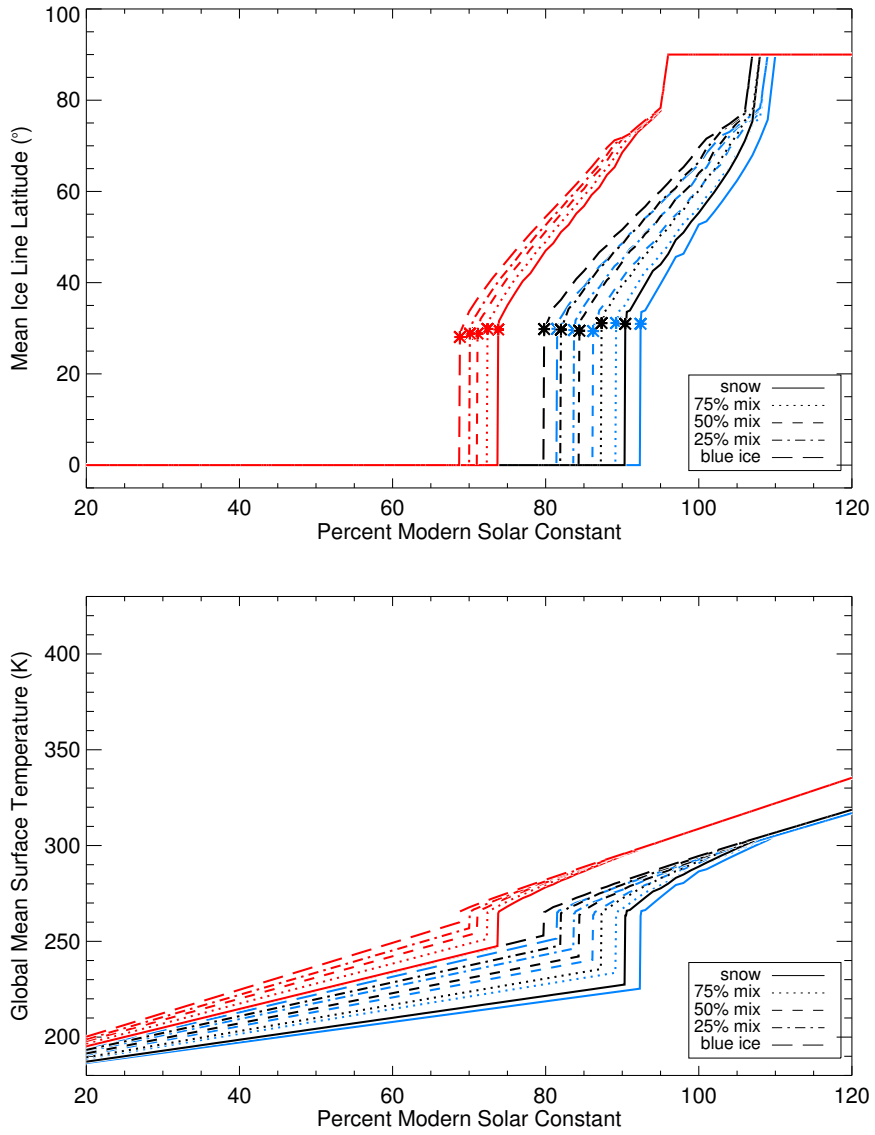

Figure 3.3 Mean ice line latitude (top) and global mean surface temperature (bottom) in the northern hemisphere as a function of percent of modern solar constant are calculated using a seasonal EBM, at present Earth obliquity (23.5°) for aqua planets (land and ocean fraction 0.01 and 0.99, respectively) orbiting F-, G-, and M-dwarf stars at equivalent flux distances. Below-freezing surfaces encountered during the EBM runs (where the temperature is less than -2°C) were given broadband planetary albedos for ice and snow of varying grain size calculated from SMART at 1-bar surface pressure. EBM simulations were run with an initial warm start, with an approximate Earth-like zonal mean temperature distribution. The results can be assumed to be similar for the southern hemisphere, given an assumed eccentricity of zero. The present atmospheric level (PAL) of CO_2 was used (F-dwarf planet in blue, G-dwarf planet in black, and M-dwarf planet in red). Asterisks denote the minimum ice line latitude before collapse to the equator and global ice coverage.

the time-mean about the equator over an annual cycle.

The ice line latitude is stable (does not collapse to the equator) 17-24 degrees farther towards the equator for all simulated aqua planets (Figure 3.4) than those calculated in the EBM (Figure 3.3), yielding gentler transitions in latitudinal ice extent and global mean surface temperature as a function of percent of modern solar constant in the GCM than is seen in the EBM. This is largely due to the presence of full-scale atmospheric dynamics and clouds in the GCM, as explained in Section 2.2.2. As the slopes of the lines in Figures 3.3 and 3.4 are a measure of the climate sensitivity of the planets, the GCM results indicate a lower climate sensitivity to changes in instellation than would be inferred from the EBM results alone.

A comparison of 3-D simulations of the climate of a planet receiving 90% of the modern solar constant (1224 W/m^2) from an M-dwarf with one receiving 90% flux from the Sun yields significant differences in the resulting climate states. The planet receiving the Sun's SED is completely ice-covered, with a global mean surface temperature of 215 K, while the planet receiving the M-dwarf star's SED is 72 degrees hotter (at ∼288 K, see Figure 3.5). This is largely due to the increased absorption of the predominantly near-IR radiation emitted by M-dwarf stars, by atmospheric CO_2 and water vapor. This results in a much larger greenhouse effect that keeps the M-dwarf planet's surface warmer than the G-dwarf planet (Kasting et al., 1993; Selsis et al., 2007). The M-dwarf planet's global mean surface temperature and ice line latitude (58.7°) are in better agreement with the global mean surface temperature and latitudinal ice extent on a G-dwarf planet receiving 100% of the modern solar constant (∼1360 W/m^2), which are 287 K and 58.3°, respectively. One-dimensional radiative-convective calculations by Kasting *et al.* (1993) yielded comparable stratospheric water vapor mixing ratios and planetary surface temperatures between G- and M-dwarf planets when the M-dwarf planet received 10% less flux from its star compared to the G-dwarf planet, though the emission from the stars in their simulations was approximated by blackbody radiation (Kasting et al., 1993).

With the CO_2 held fixed at 400 ppm, we started with simulations that would result in similar surface climate conditions on F-, G-, and M-dwarf aqua planets. On an F-dwarf

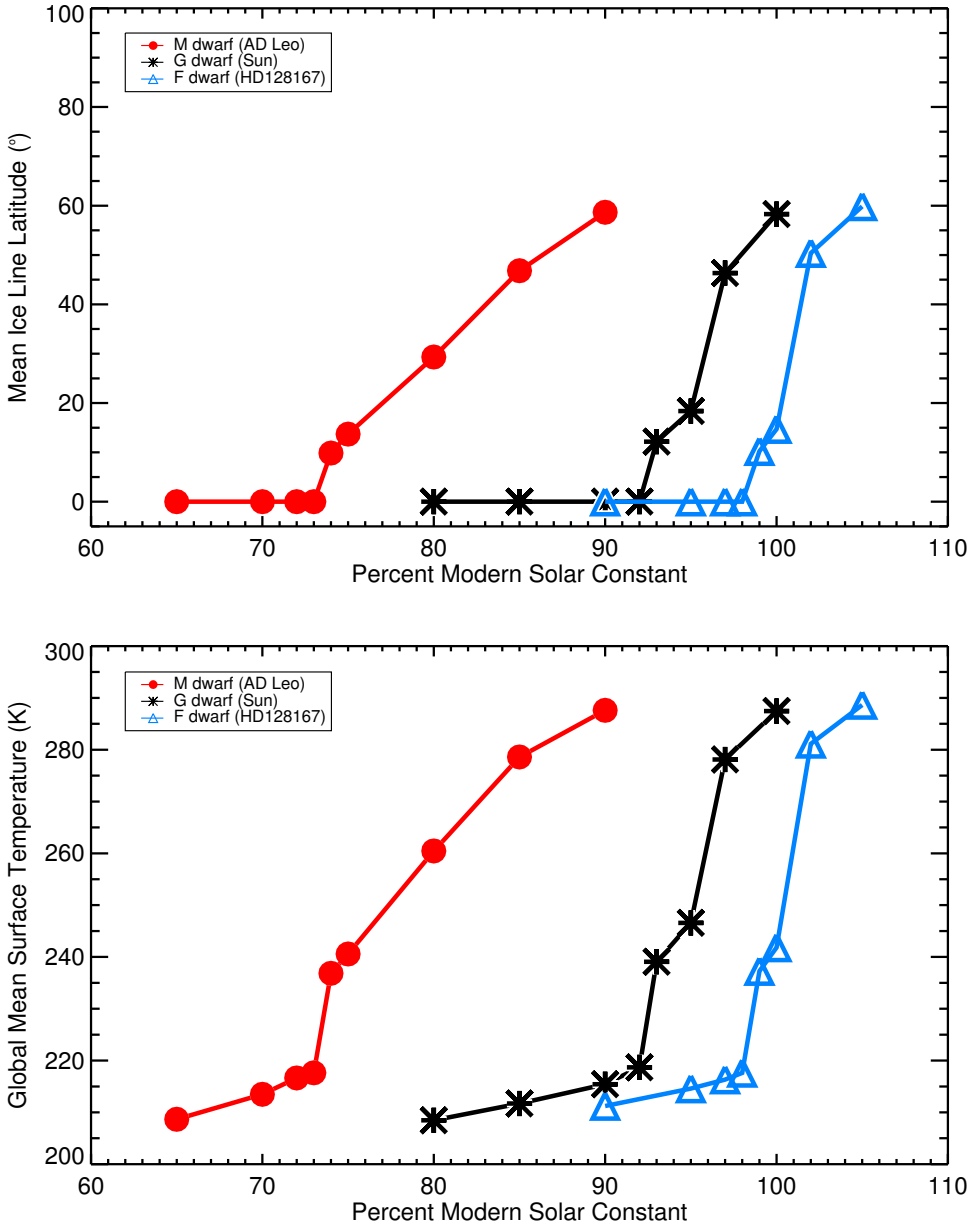

Figure 3.4 Mean ice line latitude (top) and global mean surface temperature (bottom) as a function of percent of modern solar constant after a 40-year GCM run for an aqua planet orbiting the Sun (black), M-dwarf star AD Leo (red), and F-dwarf star HD128167 (blue) at equivalent flux distances. The slope of each line is a measurement of the climate sensitivity of the planet to changes in stellar flux. The shallower slope of the M-dwarf planet indicates a smaller change in surface temperature and ice extent for a given change in instellation than on the planets orbiting stars with greater visible and near-UV output.

planet, this required that the instellation be increased to 105% of the modern solar constant in order to yield a comparable global mean surface temperature and ice line latitude (289 K and 59.8°, respectively) to the G-dwarf planet receiving 100% of the modern solar constant (287 K and 58.3°). On an M-dwarf planet, an instellation equal to 90% of the modern solar constant is all that is required to yield a comparable global mean surface temperature and ice line latitude (288 K and 58.6°) to the G-dwarf planet receiving 100% of the modern solar constant.

On an F-dwarf planet receiving 100% of the modern solar constant, the ice line latitude is ∼15°. This is 43° farther towards the equator than the ice line latitude on a G-dwarf receiving equivalent instellation. A snowball state (where the ice covers the entire hemisphere, with a mean ice line latitude of 0°) then occurs on the F-dwarf planet with a 2% further reduction in instellation, to 98% of the modern solar constant (Fig. 3.4). An 8% reduction in instellation from the Sun is required to plunge the G-dwarf planet into global ice cover, at 92% of the modern solar constant. Ice on our M-dwarf planet does not extend all the way to the equator until the instellation has been reduced by an additional 19% compared to the G-dwarf planet, equivalent to 73% of the modern solar constant (∼979 W/m^2). In Figure 3.4, the slope of the curve with decreasing stellar flux for the M-dwarf planet is much shallower than those for the G- and F-dwarf planets, indicating a much lower change in surface temperature and ice extent for a given change in stellar flux on the M-dwarf planet.

As stated earlier, in our GCM simulations the ice line extends farther before unstable collapse to the equator than the critical latitude of 25-30° often required by diffusive EBMs. EBMs that transport less heat across the ice line, as well as fully-coupled atmosphere-ocean GCMs, have been found to permit stable ice lines at lower latitudes (Poulsen et al., 2001; Pollard & Kasting, 2005). Cloud cover has also been shown to serve as a negative feedback on the latitudinal extent of tropical sea ice, as it contributes little additional reflectivity when located over high-albedo surfaces, but still adds to the greenhouse effect (Poulsen et al., 2001). Increased cloud cover may therefore contribute to stabilizing the ice edge in GCMs. And stable climate states with extremely low-latitude (but not equatorial) ice coverage on planets orbiting the Sun have been generated using climate models, as a

result of large albedo differences between bare sea ice and snow-covered ice (Abbot et al., 2011). The fact that the ice line extends farthest towards the equator without collapsing to a snowball state on the M-dwarf planet than on the G- or F-dwarf planets is likely a consequence of the lower albedo of ice on the planet given the M-dwarf spectrum. Indeed, the average albedo of the (mostly ice-covered) M-dwarf planet receiving 74% of the modern solar constant (the lowest amount of instellation received by the planet in our simulations without becoming completely ice-covered) is 0.51, while the G- and F-dwarf planets with slightly less ice coverage (receiving 93% and 99% of the modern solar constant respectively), have mean albedos of 0.55 and 0.58.

3.2.2.b 90% M-dwarf vs. 100% G-dwarf: The climatic effect of stellar host SED

The global mean surface temperature of the M-dwarf planet receiving 90% of the modern solar constant is quite similar to a G-dwarf planet receiving the full modern solar constant (100%), differing by less than one degree Kelvin. The latitudinal surface temperature profile is also strikingly similar (Figure 3.5), although the M-dwarf planet exhibits warmer temperatures at the poles. To understand how the M-dwarf planet is compensating for the decreased instellation, we first take a closer look at the atmospheres of the two planets.

While the surface temperature profiles of both planets appear relatively similar at subpolar latitudes, there is about ∼10% less precipitation on the M-dwarf planet everywhere except at the poles (Fig. 3.6). Precipitation is lower on the M-dwarf planet because there is less shortwave radiation reaching the surface to drive evaporation.

The shift towards longer wavelengths in the M-dwarf star SED gives rise to a greater amount of shortwave heating due to absorption in the M-dwarf planet's atmosphere than on the G-dwarf planet, particularly in the tropics. The plot of zonal mean vertical temperature follows a similar pattern, with higher temperatures throughout most of the atmospheric column in the tropics and at the poles, indicating a smaller lapse rate over most of the troposphere on the M-dwarf planet than on the G-dwarf planet (Fig. 3.7a-c). The weaker Hadley circulation on the M-dwarf planet (Fig. 3.8) contributes to the greater tropospheric temperatures. However, near the surface, the difference in atmospheric temperature between the two planets is minimal. The stability of the atmospheres is therefore similar near the

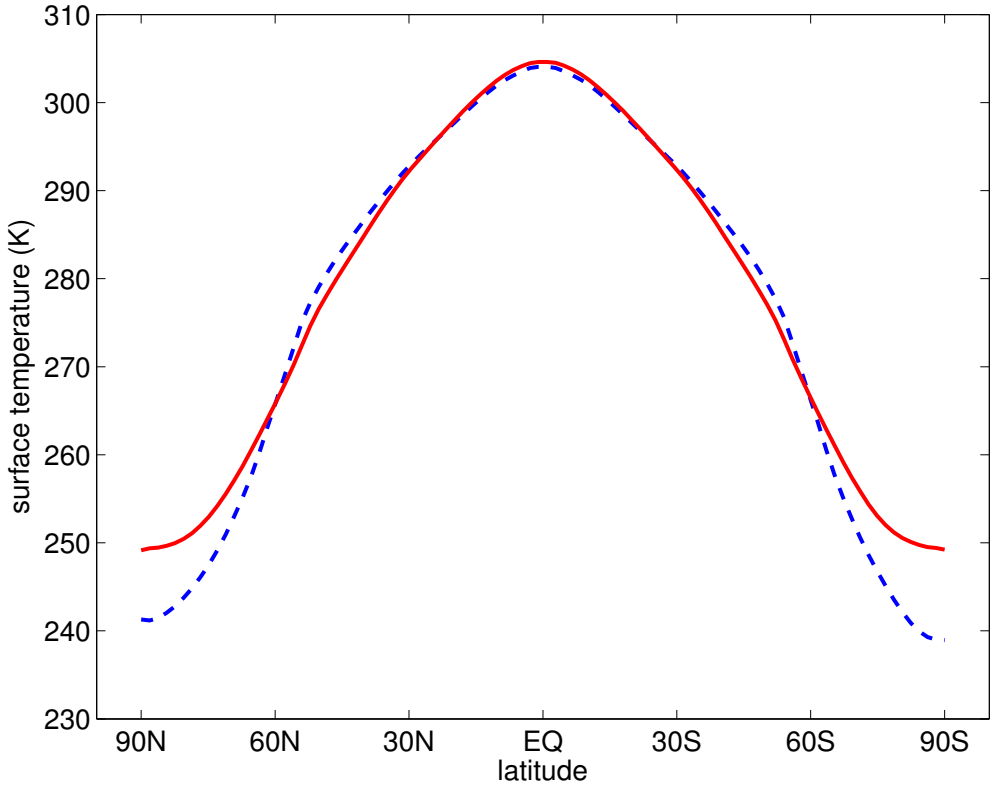

Figure 3.5 Surface temperature on an aqua planet receiving 90% of the modern solar constant from an M-dwarf star (red) compared with an aqua planet receiving 100% of the modern solar constant from the Sun, a G-dwarf star (blue), after a 40-year GCM run.

surface, but the M-dwarf planet appears more stable over the free (upper) troposphere, resulting in less cloudiness at most heights (Fig. 3.9), less precipitation, and more shortwave radiation absorbed by the planet. The more absorbing ice and snow on the M-dwarf planet (Fig. 3.10) allows the polar regions of the M-dwarf planet to be slightly warmer than the G-dwarf planet, with a similar ice line latitude despite the greatly reduced instellation.

3.2.2.c 73% M-dwarf vs. 92% G-dwarf: A comparison of Snowball planets

GCM simulations of an aqua planet receiving 73% of the modern solar constant from an M-dwarf star and an aqua planet receiving 92% of the modern solar constant from the Sun result in similar surface conditions, with ice extending all the way to the equator on both planets.

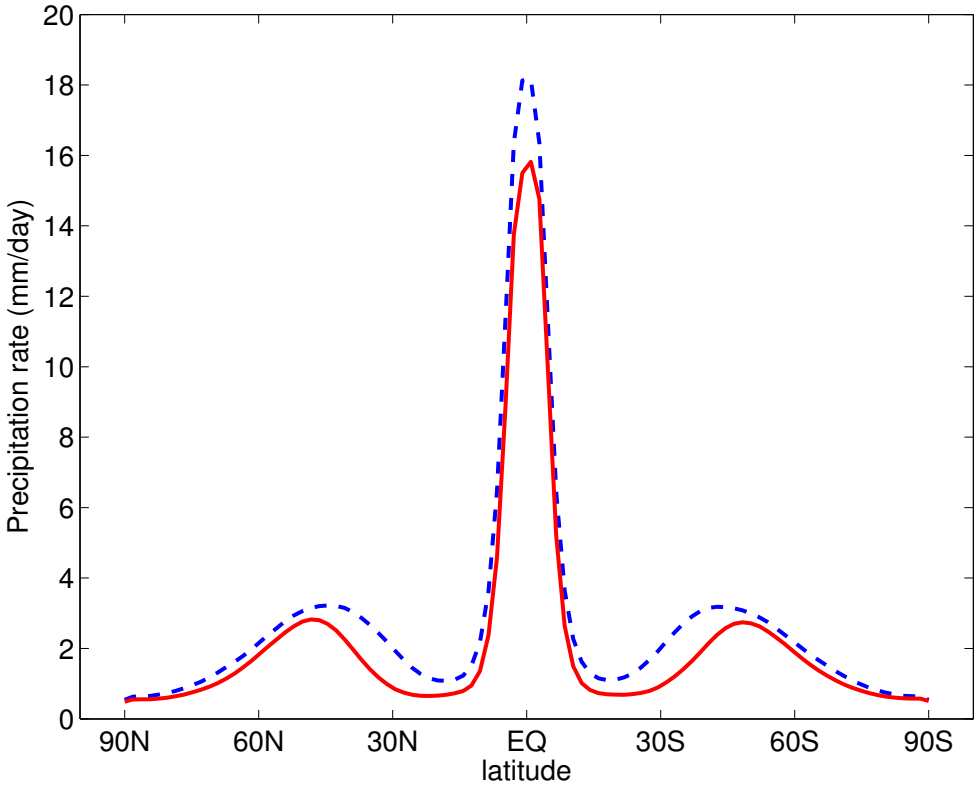

Figure 3.6 Precipitation rate on an aqua planet receiving 90% of the modern solar constant from an M-dwarf star (red) compared with an aqua planet receiving 100% of the modern solar constant from the Sun (blue), after a 40-year GCM run.

A comparison of zonal mean vertical temperature on the two snowball planets shows higher temperatures in the upper troposphere of the M-dwarf planet (likely a consequence of greater shortwave heating due to absorption in the M-dwarf planet's atmosphere, as described in the previous section), but minimal difference in atmospheric temperature between the two planets near the surface (Fig. 3.11). Surface shortwave downwelling flux is the amount of flux from the host star that passes through the atmosphere and reaches the surface of the planet. Since the G-dwarf planet receives 19% more radiation from its star than the M-dwarf planet, much more shortwave radiation reaches the surface of the G-dwarf planet (Figure 3.12a). However, the G-dwarf planet's surface is more reflective, due to the greater percentage of visible radiation (as discussed in Section 1.3) incident on the G-dwarf planet

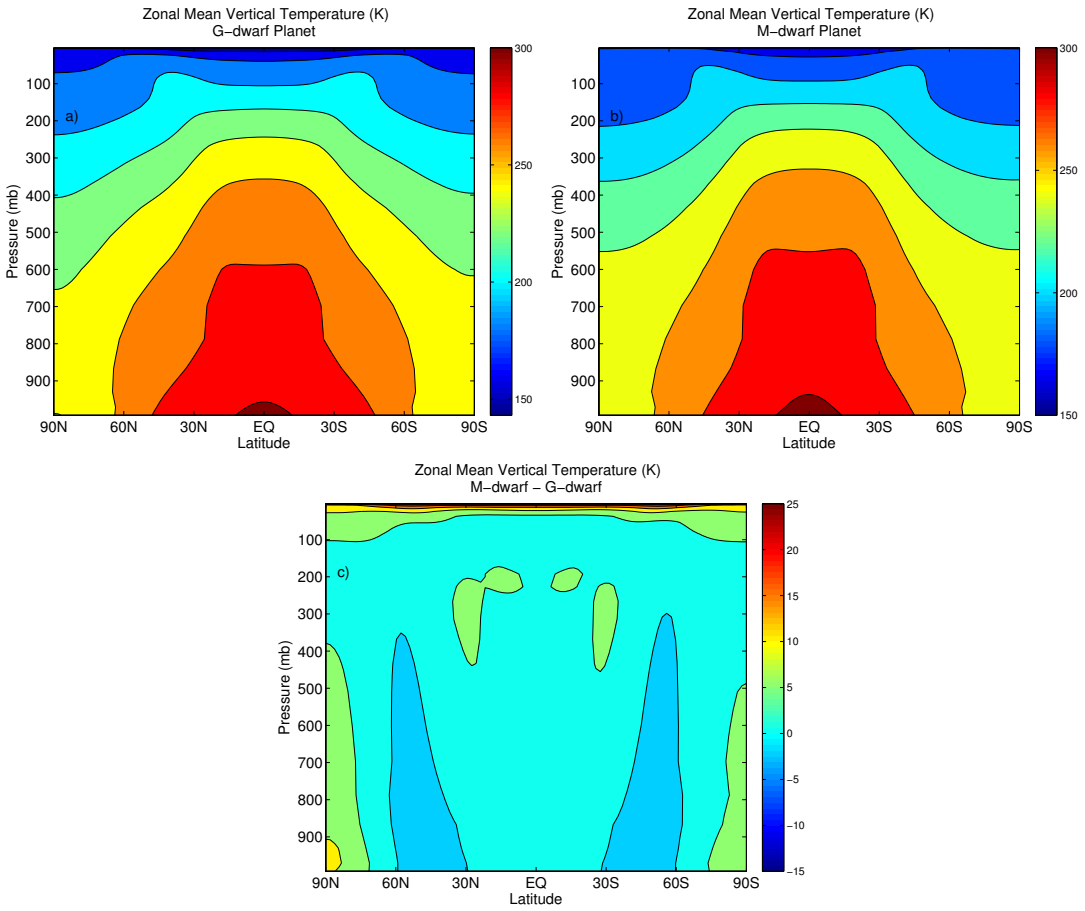

Figure 3.7 GCM Comparison of an M-dwarf aqua planet receiving 90% of the modern solar constant compared with an aqua planet receiving 100% of the modern solar constant from the Sun, a G-dwarf star. (a) zonal mean temperature in the atmosphere of the G-dwarf aqua planet; (b) zonal mean temperature in the atmosphere of the M-dwarf aqua planet; (c) increase in zonal mean temperature in the atmosphere of the M-dwarf aqua planet, calculated by taking the difference between the M-dwarf planet's atmospheric temperature profile and the G-dwarf planet's atmospheric temperature profile.

(Figure 3.12b). As a result the G-dwarf planet cannot absorb enough shortwave radiation to avoid full ice coverage. Higher absorption of the shortwave spectrum incident on the surface of the M-dwarf planet compensates for the reduced instellation, resulting in similar amounts of shortwave radiation absorbed on the surfaces of both planets (Figure 3.12c), and similar global mean surface temperatures of ∼218 K (Figure 3.12d). Indeed, of the total shortwave

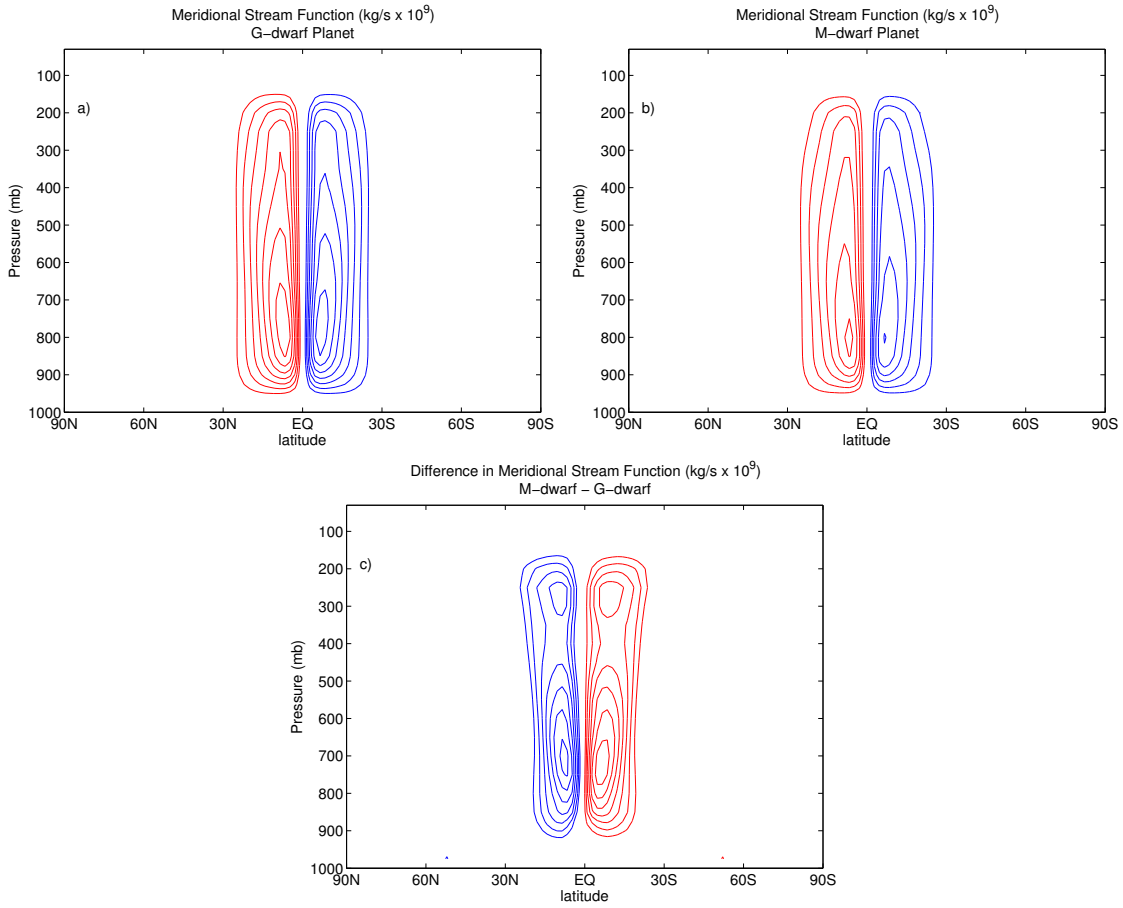

Figure 3.8 GCM Comparison of an M-dwarf aqua planet receiving 90% of the modern solar constant compared with an aqua planet receiving 100% of the modern solar constant from the Sun, a G-dwarf star. Blue = clockwise circulation. Red = counterclockwise circulation. (a) Meridional stream function in the atmosphere of the G-dwarf planet. The contours start at 50 kg/s x 10^9, and the contour interval is 25 kg/s x 10^9; (b) Meridional stream function in the atmosphere of the M-dwarf planet. The contours start at 50 kg/s x 10^9, and the contour interval is 25 kg/s x 10^9; (c) increase in the meridional stream function in the atmosphere of the M-dwarf planet, calculated by taking the difference between the M-dwarf planet's meridional stream function and the G-dwarf planet's meridional stream function. The contours start at 10 kg/s x 10^9, and the contour interval is 5 kg/s x 10^9. The weaker Hadley circulation on the M-dwarf planet results in greater atmospheric temperatures, and less heat transported away from the equator, compensating for the reduced instellation relative to the G-dwarf planet.

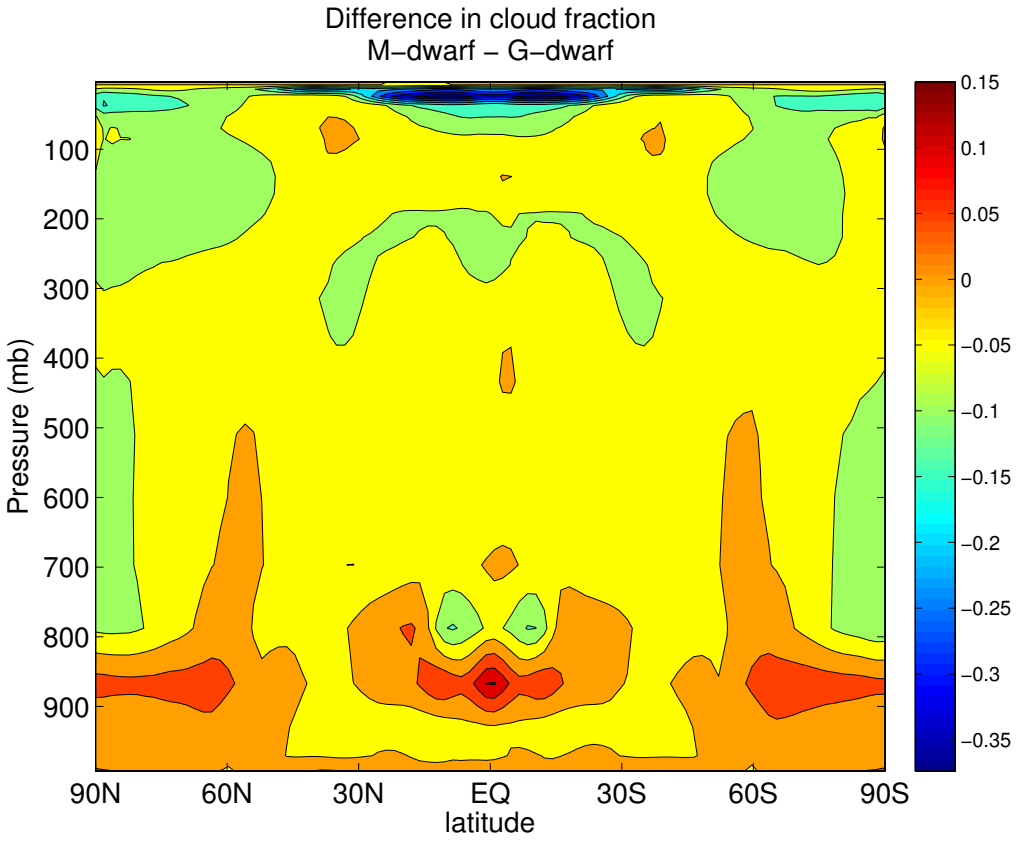

Figure 3.9 Difference between the cloud fraction in the atmosphere of an aqua planet receiving 90% of the modern solar constant from an M-dwarf star and an aqua planet receiving 100% of the modern solar constant from the Sun after a 40-year GCM run.

flux that reaches the surface of the M-dwarf planet, ∼44% is absorbed by the surface at the equator and ∼30% is absorbed at the poles, compared with ∼35% absorbed at the equator and ∼25% at the poles on the G-dwarf planet. The three peaks in surface absorbed shortwave in the tropics and subtropics on the G-dwarf planet in Figure 3.12c result from local minima in the surface albedo (Fig. 3.12b) where evaporation exceeds precipitation and hence snow depths are locally smaller.

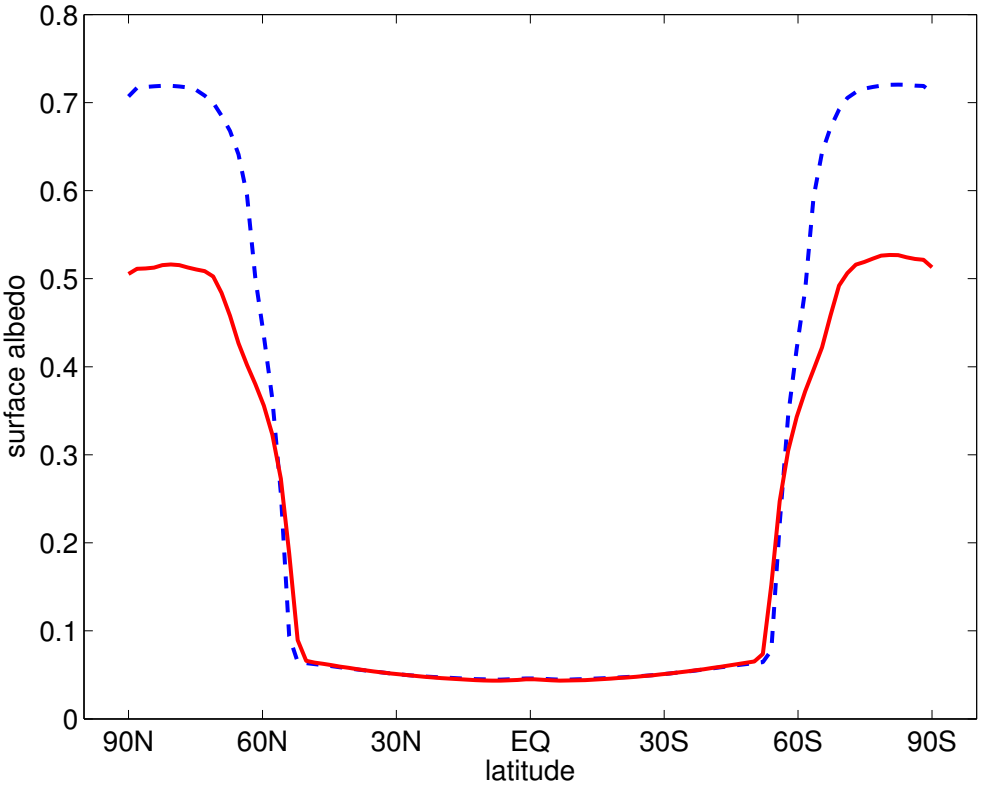

Figure 3.10 Surface albedo as a function of latitude for an M-dwarf aqua planet receiving 90% of the modern solar constant (red) compared with an aqua planet receiving 100% of the modern solar constant from the Sun, a G-dwarf star (blue), after a 40-year GCM run.

3.2.2.d Testing climate sensitivity to surface albedo

Since the atmosphere of the M-dwarf planet absorbs such a large amount of the shortwave radiation, lowering the overall planetary albedo, it was important to verify whether the spectral dependence of surface ice albedo had any discernible effect on a planet's climate at Earth-like atmospheric CO_2 levels. By lowering the IR and visible band cold ice and snow albedos for an M-dwarf planet to 0.2, thereby significantly reducing the difference between ice and ocean on the planet's surface, we were able to examine the effect on climate sensitivity of surface ice and snow albedo interacting with the host star SED. Ice and snow albedos were lowered on M-dwarf planets receiving 75% and 85% of the modern solar constant, and the results were compared with model runs with the default albedo

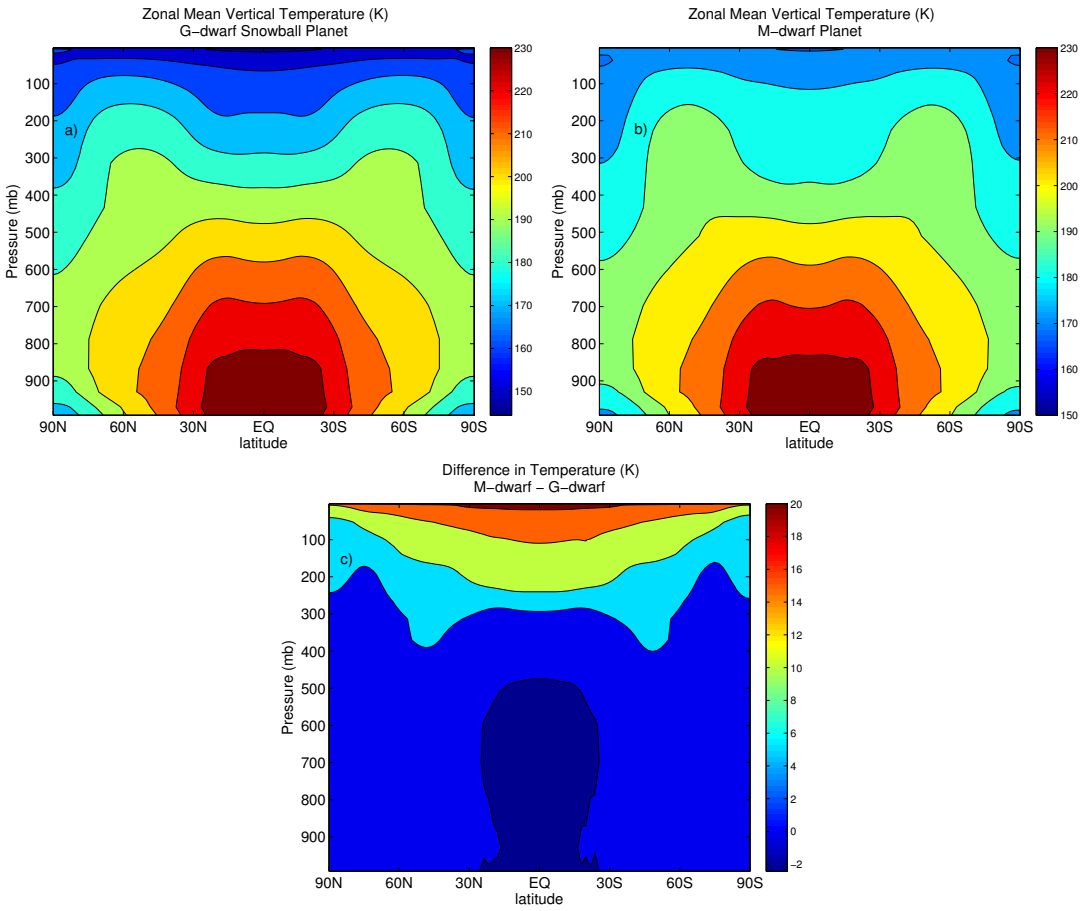

Figure 3.11 GCM Comparison of an M-dwarf aqua planet receiving 73% of the modern solar constant (993 W/m^2) with an aqua planet orbiting the Sun and receiving 92% of the modern solar constant (1251 W/m^2). Both planets are completely ice-covered. (a) Zonal mean temperature in the atmosphere of the G-dwarf planet; (b) zonal mean temperature in the atmosphere of the M-dwarf planet; (c) increase in temperature in the atmosphere of the M-dwarf aqua planet, calculated by taking the difference between the M-dwarf planet's atmospheric temperature profile and the G-dwarf planet's atmospheric temperature profile.

parameterization (see Section 2.2.2) for planets receiving equivalent instellation. The results are plotted in Figure 3.13.

The result for both M-dwarf planets is a warmer climate and less ice than with the default albedo parameterization. The difference in climates is larger between the M-dwarf planets receiving 75% instellation than between the M-dwarf planets receiving 85% instellation, as

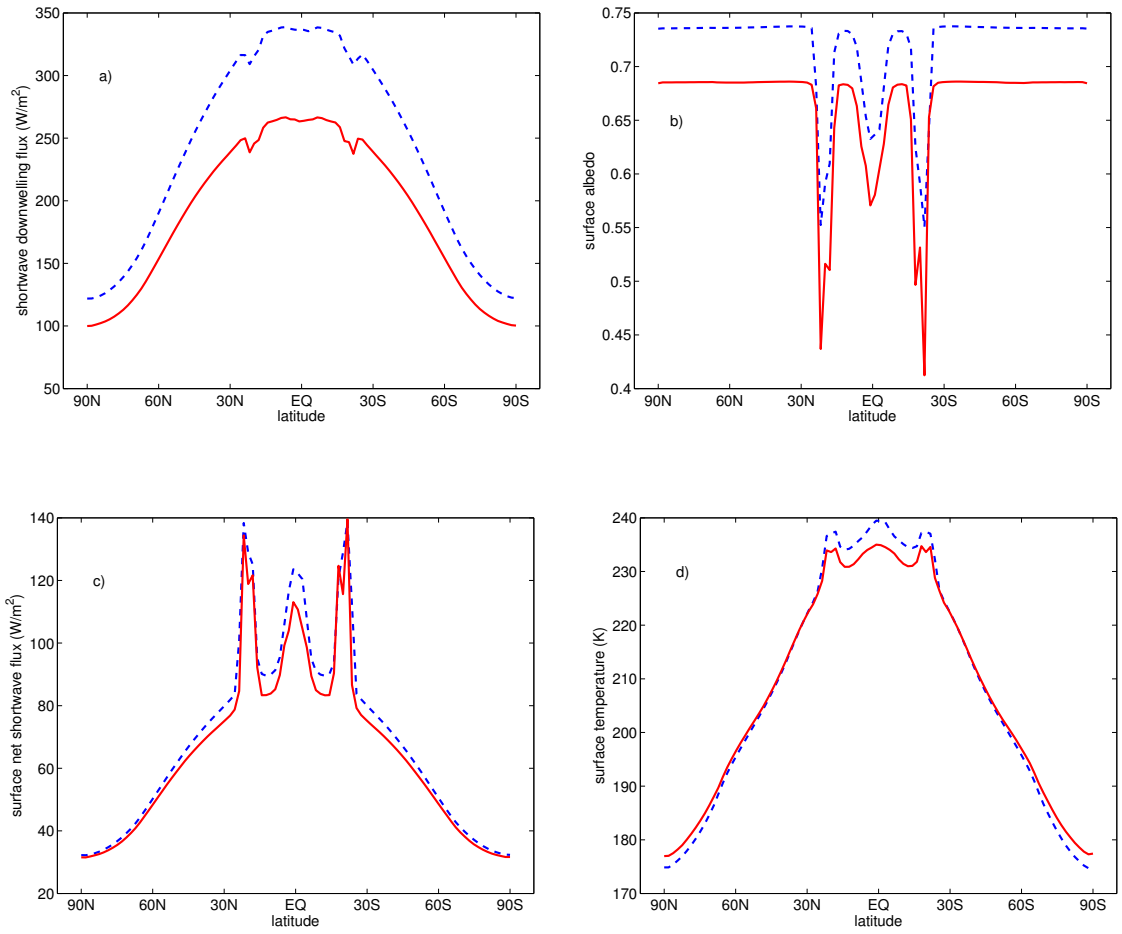

Figure 3.12 GCM Comparison of an M-dwarf aqua planet (red) receiving 73% of the modern solar constant (993 W/m^2) with an aqua planet orbiting the Sun and receiving 92% of the modern solar constant (1251 W/m^2, blue). Both planets are completely ice-covered. (a) Surface shortwave downwelling flux as a function of latitude; (b) surface albedo; (c) net shortwave flux absorbed by the surface; (d) surface temperature.

indicated by the black vertical lines in Figure 3.13. This is because there is a higher surface coverage of ice on the M-dwarf planet receiving lower instellation, resulting in a larger impact on the planet's climate when the ice and snow albedos are lowered, including larger increases in temperature, cloudiness and precipitation. As a result, the M-dwarf planet's slope of the temperature and ice extent as a function of instellation is much shallower than that of the M-dwarf planet runs with the default albedo parameterization. This shallower

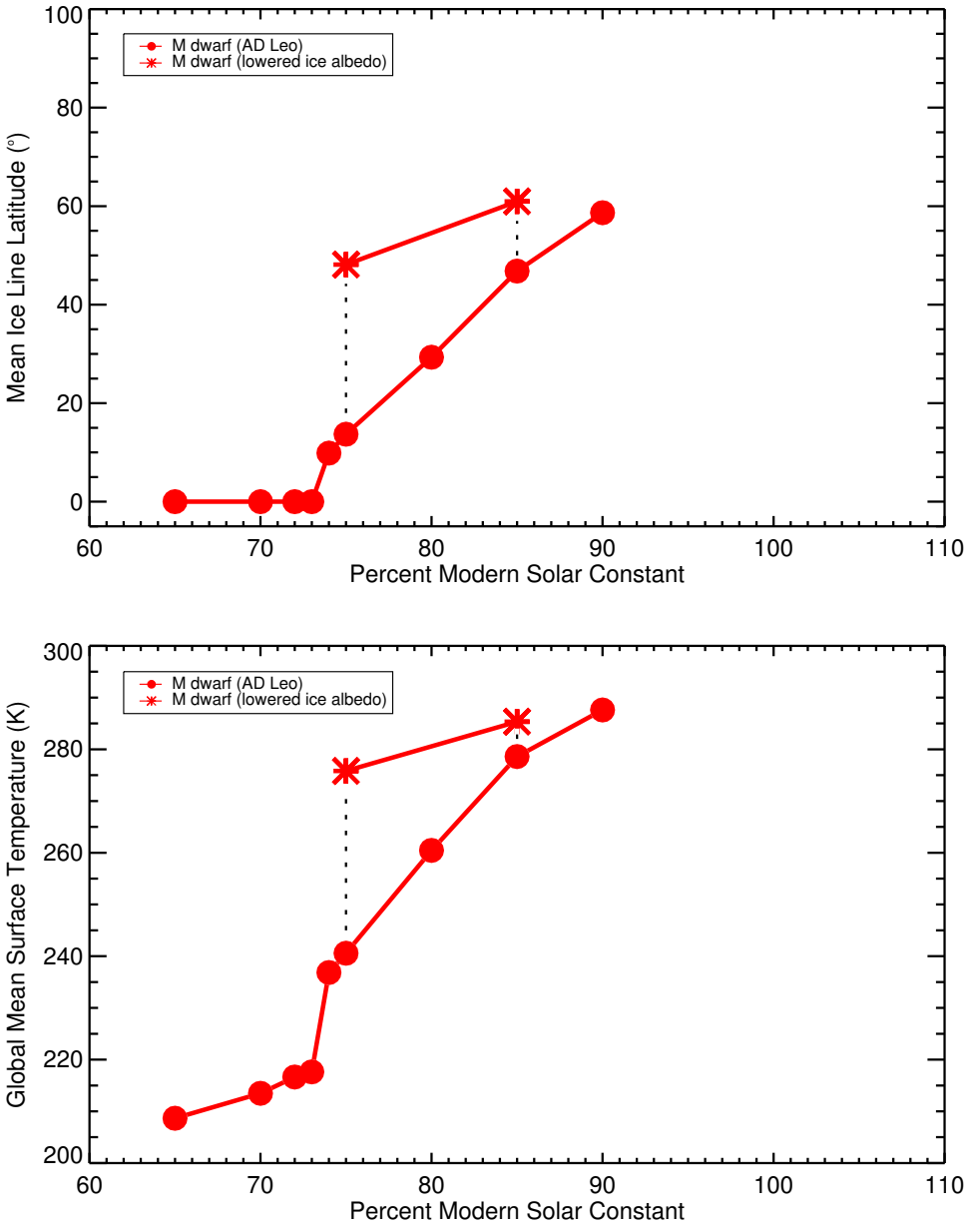

Figure 3.13 Mean ice line latitude (top) and global mean surface temperature (bottom) as a function of percent of modern solar constant after a 40-year GCM run for an aqua planet orbiting an M-dwarf star, from Figure 3.4. Also plotted here are the resulting ice extents and global mean surface temperatures for M-dwarf planets receiving 75% and 85% instellation, with IR and visible band ice and snow albedos lowered to 0.2 (asterisks). The difference in climates is larger between the M-dwarf planets receiving 75% instellation than between the M-dwarf planets receiving 85% instellation (as indicated by the black vertical lines), exhibiting a shallower change in global mean surface temperature and ice extent for lowered instellation than with the default albedo parameterization.

slope implies a smaller change in surface temperature and ice extent for a given change in instellation, indicating that a planet's climate is sensitive to surface ice and snow albedo, even with an Earth-like atmospheric concentration of greenhouse gases.

3.2.3 High-CO_2 atmosphere: The outer edge of the habitable zone

Atmospheric CO_2 concentrations are expected to increase farther out in the habitable zone, where decreased silicate weathering would lead to CO_2 building up in the atmosphere (Walker et al., 1981). CO_2 content at the OHZ would therefore be high, and could reach levels of over 2 bars before reaching the maximum CO_2 greenhouse limit (Pierrehumbert, 2010). Given that CO_2 has a number of absorption bands in the near-IR, where M-dwarf stars emit strongly and snow albedo drops significantly, we ran sensitivity tests to quantify the effect of CO_2 on the suppression of the cooling effect of ice-albedo feedback for M-dwarf planets. Runs were completed using SMART and included a case for a pure nitrogen atmosphere with little to no near-IR gas absorption, and cases for atmospheres consisting of 10% CO_2 and 90% N_2, 50%/50% CO_2/N_2, and pure CO_2 atmospheres at 2-, 3-, 10-, 12-, 14- and 15-bar surface pressures. For these sensitivity tests, no clouds were included. For atmospheric pressures greater than 1 bar, the vertical pressure profile was multiplied by the desired integer scaling factor, and the molecular weight of the atmosphere was adjusted accordingly. We did two runs at each atmospheric concentration: One with the actual fine-grained snow albedo spectrum from Grenfell (1994), which drops to low values in the near-IR, and one where the Grenfell snow spectrum was altered to exhibit artificially high albedo values of 0.6 at wavelengths longer than 1.1 μm. Cross-section and line absorption coefficient files for CO_2 were included as input and created using LBLABC with data from the HITRAN 2008 database (Rothman et al., 2009). The results are plotted in Figure 3.14.

The pure nitrogen atmosphere run resulted in the highest broadband planetary albedo, due to its relative dearth of spectral absorption features. When 0.1 bar of atmospheric CO_2 is introduced, the broadband planetary albedo decreases by 7%. When the artificially-enhanced snow spectrum is used as the input surface spectrum, the broadband albedo values for the pure nitrogen atmosphere case increase by the largest amount. As atmospheric

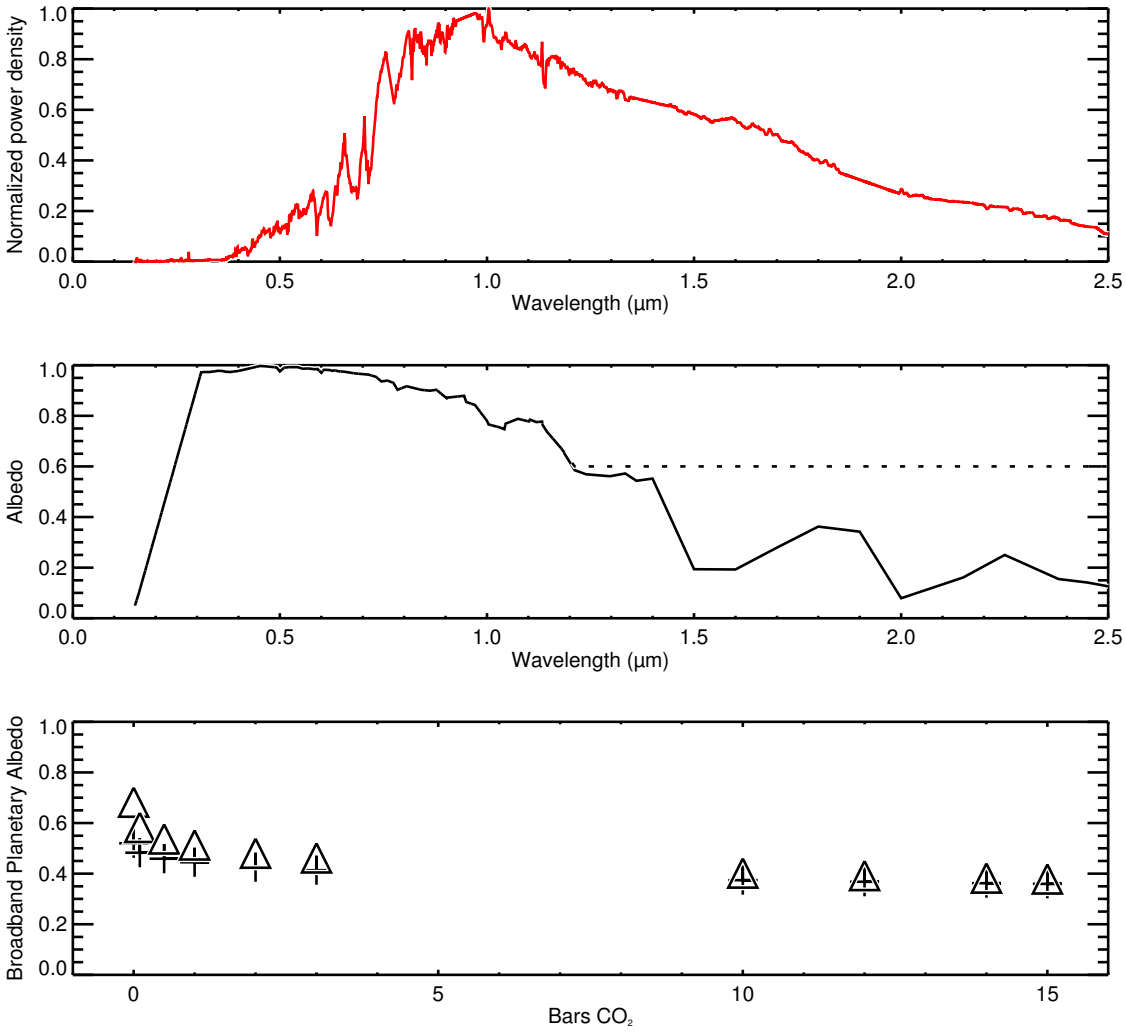

Figure 3.14 Top: The normalized SED of the M3V star AD Leo. Middle: The albedo spectrum of fine-grained snow (solid line), with artificially-enhanced albedo values of 0.6 at wavelengths longer than 1.1μm (dashed line). Bottom: Broadband planetary albedos (0.15 μm $\leqslant \lambda \leqslant$ 2.5 μm) as output from SMART, given an incident M-dwarf spectrum, input actual (plus symbols) and artificially-enhanced (triangles) snow albedo spectra, and various concentrations of atmospheric CO_2. The concentration of CO_2 can be expected to effectively mask the ice-albedo spectral dependence when the broadband planetary albedo for the actual input snow spectrum (with lower near-IR albedo values) matches that for the artificially-enhanced snow spectrum (with high values of near-IR albedo), demonstrating that broadband planetary albedo is no longer sensitive to the surface albedo of the planet. This appears to happen at atmospheric concentrations of between 3 and 10 bars of CO_2.

CO_2 concentration is increased, the difference between the calculated broadband planetary albedo using the actual snow spectrum, and that using the artificially higher snow spectrum decreases. At atmospheric concentrations of ∼3 bars of CO_2, the broadband albedo for the planet with the actual snow spectrum matches that calculated with the artificially-high snow spectrum to within ∼10.5%. At 10 bars of CO_2, the two values match to within 6.9%. Differences in reflectivity as a function of wavelength between the planets with the actual and altered snow surfaces, given CO_2 concentrations of 0.1, 3, and 10 bars, are shown in Figure 3.15. With 10 bars of CO_2 in the atmosphere, the reflectivity at longer wavelengths has plummeted due to near-IR absorption by CO_2, and the spectra of the planets with the actual and artificially-enhanced snow albedo spectra are indistinguishable.

The absorption cross-section of CO_2 is temperature-dependent, with cross-sections increasing with temperature towards longer wavelengths (Parkinson et al., 2003). Increasing the temperature at which our absorption coefficients were calculated in SMART by 50 K for atmospheres of 10 bars of CO_2 resulted in a ∼0.1-0.2% decrease in broadband planetary albedo.

As CCSM4 is currently incapable of simulating atmospheric CO_2 concentrations greater than ∼0.1 bar, we used SMART with our 1-D EBM to address the high-CO_2 case. Figure 3.16 shows the results of EBM simulations using broadband planetary albedos calculated with SMART assuming a 3-bar pure CO_2 atmosphere on planets orbiting M-, G-, and F-dwarf stars, along with the original EBM simulations with Earth-like atmospheric CO_2 concentrations from Figure 3.3. Inputs to SMART, including the atmospheric pressure profile, were scaled for a 3-bar surface pressure. As in the model runs with an Earth-like atmosphere, broadband planetary albedos for different surface types were generated assuming both clear and cloudy sky conditions. Average broadband planetary albedos over ocean, land, and below-freezing surfaces for the high-CO_2 case were calculated as described in Section 2.2.1.d, and used as input to the EBM. The coefficients governing the effect of CO_2 and water vapor in the linear function of temperature that is parameterized for outgoing longwave radiation in the EBM were also adjusted to account for the increased CO_2. Due to near-IR absorption by the significantly larger amount of CO_2 in the atmospheres of the three planets, ice-free climates exist on all planets with much higher decreases in instellation

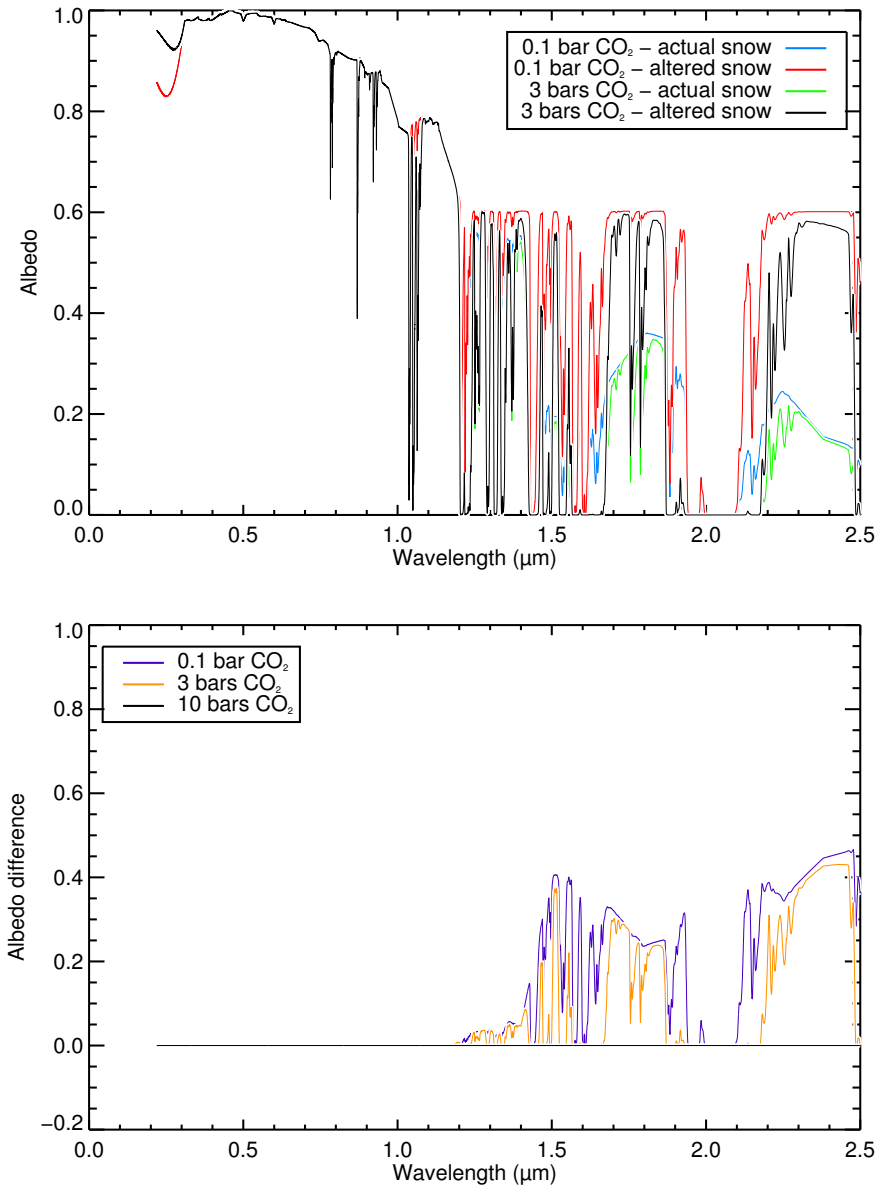

Figure 3.15 Wavelength-dependent reflectivity of a planet with various concentrations of atmospheric CO_2 and an underlying snow surface, calculated with SMART using the actual measured albedo spectrum, and one that was altered to exhibit artificially high albedo values of 0.6 at wavelengths longer than 1.1 μm. Top: 0.1 bar of CO_2 and an underlying snow surface matching the fine-grained snow spectrum in Figure 1 (blue); 0.1 bar of CO_2 with a snow surface with an artificially-enhanced spectrum (red); 3 bar-CO_2 atmosphere with the actual snow spectrum (green); 3 bar-CO_2 atmosphere with the artificially-enhanced snow spectrum (black). Bottom: Change in reflectivity between the planets with artificially-enhanced vs. actual snow surface albedo spectra. With 3 bars of CO_2 in the atmosphere, the difference between the albedos of the planets (orange) has decreased compared to that of the 0.1-bar planets (purple). With 10 bars of CO_2 in the atmosphere, the difference in the albedo spectra of the planets (black) is close to zero, due to increased near-IR absorption by CO_2 at longer wavelengths.

than in the simulations with an Earth-like CO_2 concentration. Once ice appears on each planet, the ice expands to total ice cover with a smaller reduction in instellation than with Earth-like CO_2 levels, as the planets are close to the OHZ at these low values of stellar flux density. This increased climate sensitivity is the result of much lower surface temperatures at those low values of instellation, as well as the weaker relationship between outgoing longwave radiation and surface temperature in this high-CO_2 case. In essence, the greenhouse effect fails to keep the surface temperature above freezing over large areas of the planet at these low values of instellation as we approach the maximum CO_2 greenhouse limit. Figure 3.16 indicates that given high levels of CO_2, planets remain ice-free throughout the majority of the width of the habitable zone. M-dwarf planets with 3-bars of CO_2 in their atmospheres appear ice-free with larger decreases in instellation than G- or F-dwarf planets with equivalent CO_2 concentrations. This is due to greater CO_2 absorption of the increased near-IR radiation emitted by M-dwarf stars. M-dwarf planets appear to be less susceptible to global glaciation over the course of their history, but at the outer edge of the habitable zone, where CO_2 levels are expected to be high, the ice-albedo effect is muted by atmospheric CO_2 absorbing strongly in the near-IR. Once ice does appear on the planets, even with the largest-grained, lowest-albedo ice surfaces, the points of global ice cover do not occur farther out than the traditional maximum CO_2 greenhouse limits (Kasting et al., 1993), which have been updated by Kopparapu *et al.* (2013a; 2013b) and we have plotted as vertical lines for each planet in Figure 3.16.

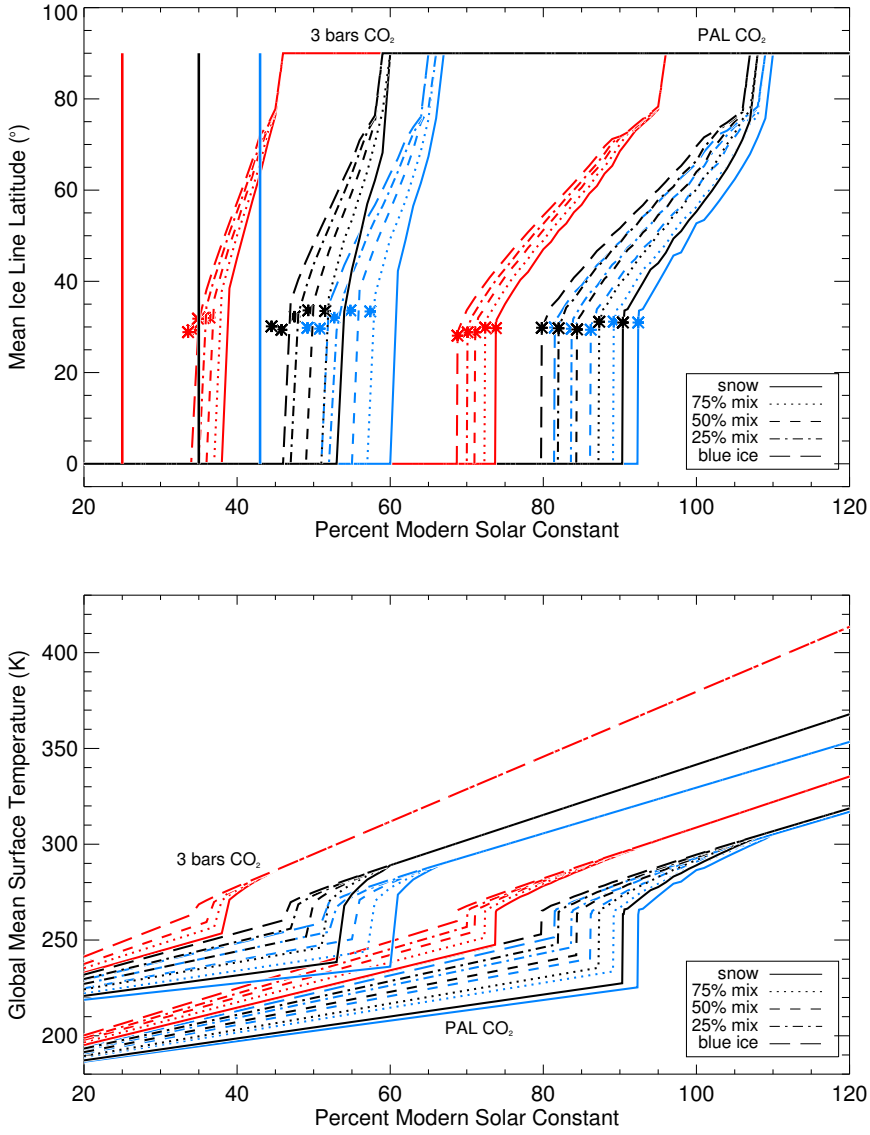

Figure 3.16 Mean ice line latitude (top) and global mean surface temperature (bottom) in the northern hemisphere as a function of percent of modern solar constant are calculated using a seasonal EBM, at present Earth obliquity (23.5°) for aqua planets (land and ocean fraction 0.01 and 0.99, respectively) orbiting F-, G-, and M-dwarf stars at equivalent flux distances, as in Figure 3.3. Here the present atmospheric level (PAL) of CO_2, as well as 3 bars of CO_2 were used (F-dwarf planet in blue, G-dwarf planet in black, and M-dwarf planet in red). Asterisks denote the minimum ice line latitude before collapse to the equator and global ice coverage. Also plotted here as vertical solid lines are the updated maximum CO_2 greenhouse limits for the F-dwarf (blue), G-dwarf (black), and M-dwarf (red) planets (Kopparapu et al., 2013a,b).

3.3 Discussion

The results of our model simulations indicate that the interaction between wavelength-dependent planetary surface albedo and the SED of a star may significantly affect the climate of an orbiting planet. The spectral dependence of ice and snow albedo is most important for planets in the middle range of a star's habitable zone. At the inner edge of the habitable zone, a planet will receive too much flux to have significant ice on its surface. At the outer edge of the habitable zone, high CO_2 masks the ice-albedo effect.

Our SMART + EBM model can reproduce the Earth's current global mean surface temperature and ice line latitude at its present obliquity to within three degrees Celsius and six degrees of latitude respectively, given gas absorption by the seven major atmospheric constituent species. EBM simulations produce ice lines that are farther towards the poles on M-dwarf planets compared to those on G-dwarf planets for a given instellation, providing confirmation of the analytical supposition of Joshi and Haberle (2012) that the cooling effect of ice-albedo feedback may indeed be suppressed on planets orbiting stars that emit large amounts of radiation in the near-IR, where ice and snow absorb strongly. Building on their initial work, our EBM results additionally imply that the cooling effect of ice-albedo feedback may be enhanced on planets orbiting F-dwarf stars, as global ice cover occurs for a much smaller change in instellation on F-dwarf planets than on planets orbiting G- or M-dwarf stars (Figs. 3.3 and 3.4). SMART upwelling and downwelling flux output indicate that broadband planetary albedo increases for SEDs with higher visible and near-UV radiation output, especially for ice and snow surface spectra, whose wavelength-dependent albedo increases in the visible and near-UV. This trend remains even when the effect of Rayleigh scattering in the atmosphere is removed, and would be absent without incorporating the spectral dependence of ice and snow albedo across the full near-UV through near-IR spectrum. Our results suggest that planets orbiting cooler, redder stars remain free from global ice cover with larger decreases in instellation. This effect may also be reinforced at higher obliquities than those considered here, as previous work has shown that planets with high planetary obliquities may be less susceptible to snowball episodes (Williams & Kasting, 1997; Spiegel et al., 2009).

Additionally, we find that ice grain size strongly affects the latitudinal extent of the ice line, and that the type of ice on a planetary surface may strongly affect its climate. The larger the ice grain size, the lower the calculated broadband planetary albedo, and the higher the resulting ice line latitude determined by the EBM. Given a simplified aqua planet configuration, ice-covered states are possible with smaller decreases in instellation for below-freezing surfaces of finer grain size such as fresh snow, which have high broadband albedos given an F-dwarf incident spectrum. Assuming an Earth-like atmosphere with clouds and the effect of Rayleigh scattering included, our SMART runs show that increasing the ice grain size results in a $\sim$12% to $\sim$17% increase in broadband planetary albedo per 25% mixture of blue ice and snow. Planets with surfaces composed of ice of larger grain size appear to be more stable against snowball episodes.

To further explore the atmospheric response to instellation of varying SED, we ran 3-D GCM simulations as well. In our GCM runs we have assumed an aqua planet with a 50-meter slab ocean. With a 10% reduction in instellation, surface temperatures are warmer on an orbiting M-dwarf aqua planet than a G-dwarf aqua planet, due to greater atmospheric absorption and emission of the large proportion of near-IR radiation from M-dwarf stars, by greenhouse gases like CO_2 and water vapor, which have many absorption bands in the near-IR and IR regions of the spectrum. Therefore, atmospheric absorption and downwelling longwave heating play a large role in reducing the fraction of ice covering M-dwarf planets.

However, the role played by the spectral dependence of ice albedo in affecting climate is not insignificant. In our GCM simulations of M-dwarf planets receiving far less instellation than G-dwarf planets, we find that a higher percentage of absorption by surface ice of the reduced amount of incident shortwave radiation on the M-dwarf planet helps to compensate for the reduced instellation. Lowering the albedos of ice and snow decreased the climate sensitivity of the M-dwarf planet compared to that using the default albedo values. This result implies that increased shortwave absorption by surface ice increases climate stability to changes in instellation, and planetary climate appears to be affected by the spectral dependence of ice albedo, even in the presence of Earth-like greenhouse gases in the atmosphere.

The slopes in Figure 3.4 are a measure of the climate sensitivity to changes in instellation

for these planets, given their host star SEDs and the concentration of CO_2 held fixed at the present atmospheric level on Earth. They indicate a larger change in ice cover for a given change in instellation for planets with incident spectra like the Sun's, or bluer, compared to redder host stars. The G-dwarf planet has entirely frozen over at 92% of the modern solar constant. This result is similar to those of previous climate simulations carried out by Abe *et al.* (2011), who find that an aqua planet around the Sun becomes ice-covered with a 10% reduction in instellation. A snowball state is not reached in our GCM simulations of an M-dwarf planet until the amount of flux from the star has been reduced to 73% of the modern solar constant. An F-dwarf planet has completely frozen over with only a 2% reduction in instellation compared to that of present Earth. M-dwarf planets therefore appear much less sensitive to changes in instellation, and thus less susceptible to snowball states. The M-dwarf planet in our simulations also exhibited stable lower latitude ice lines than the G- or F-dwarf planets, and this may be due to the lower-albedo ice formed on its surface. A more stable low-latitude ice line on M-dwarf planets may be possible as the result of a large albedo contrast between bare sea ice and snow-covered ice (Abbot et al., 2011).

Land planets orbiting Sun-like stars, given their lower thermal inertia and drier atmospheres, completely freeze with a 23% reduction in instellation, to 77% of the modern solar constant (Abe et al., 2011). Given that M-dwarf aqua planets continue to exhibit ice-free areas until their stellar flux has been reduced by 27% (to 73% of the modern solar constant), M-dwarf planets may be more resistant to freezing than G-dwarf planets, regardless of land percentage.

3.3.1 Additional factors affecting planetary climate

We have assumed a rotation period equal to the present Earth (24 hours) for our simulations, to isolate the effect of stellar SED and ice-albedo feedback on planetary climate. Synchronous rotation, which is expected to occur on M-dwarf planets orbiting in their stars' habitable zones (Dole, 1964; Kasting et al., 1993; Joshi et al., 1997; Edson et al., 2011), will certainly affect the results presented here. Earlier work by Edson *et al.* (2011) indicates that increasing the rotation period of an aqua planet weakens low-latitude zonal winds and cools the planet, and increased atmospheric latent and oceanic diffusive heat transport could

reduce temperature constrasts between the sunlit and dark sides of the planet. Given that a solar-type spectrum was used in their work, and our work here with an M-dwarf spectrum results in greater surface temperatures on M-dwarf planets than on G-dwarf planets receiving equal amounts of instellation, temperature contrasts between the sunlit and dark sides of a synchronously-rotating aqua planet orbiting an M-dwarf star at a 1-AU equivalent flux distance may be even further reduced.

Previous work using GCM simulations of synchronously rotating planets at 1-AU equivalent flux distances from a solar-type star suggests that atmospheric CO_2 concentrations could be nearly 200 times higher than the present atmospheric level on Earth if the substellar point is over a predominantly ocean-covered area, due to a lack of continental weathering (Edson et al., 2012). However, atmospheric CO_2 concentration could be limited by seafloor weathering on an aqua planet, resulting in much lower CO_2 partial pressures (Edson et al., 2012). Here, we have simulated an M-dwarf aqua planet with a 24-hour rotation period, making an Earth-like atmospheric CO_2 concentration a reasonable assumption.

Although M-dwarf planet climates appear to be sensitive to the surface at present atmospheric levels of CO_2, there is a limit to the amount of CO_2 that can exist in the atmosphere of a planet without masking the surface entirely at near-IR wavelengths. While the SED of M-dwarf stars coupled with the spectral dependence of ice and snow albedo may indeed allow M-dwarf planets to exist "Snowball free" with larger decreases in instellation than planets orbiting stars with higher visible and near-UV output, assuming low-to-moderate atmospheric levels of CO_2, CO_2 can be expected to build up in the atmosphere in response to lower surface temperatures and decreased silicate weathering (Walker et al., 1981). Abbot *et al.* (2012) found that, provided the land fraction is at least $\sim$0.01, climate weathering feedback should operate without a strong dependence on land fraction. As our EBM simulations with high-CO_2 atmospheres used a land fraction of 0.01 (Section 2.2), then assuming a high-CO_2 atmosphere that could result from climate weathering feedback at the OHZ is not unreasonable.

The high-CO_2 atmospheres (>3-10 bars) we have simulated using SMART may be sufficient to mask the suppressed ice-albedo feedback that is expected to occur on M-dwarf planets. From our EBM simulations of planets with 3-bar pure CO_2 atmospheres, the in-

creased absorption of near-IR radiation by large amounts of CO_2 prevents ice from forming on all three planets with significantly larger decreases in instellation than in the simulations with Earth-like CO_2 levels. The increased climate sensitivity that occurs once ice does appear on a planet with 3 bars of CO_2 in its atmosphere is the result of the greenhouse effect failing to keep surface temperatures above freezing at low values of instellation near the OHZ. We would expect to see this behavior persist in GCM simulations as well. Climate model simulations of Earth-like planets at the outer edge of their stars' habitable zones, with CO_2 partial pressures of 3-10 bars, are outside of the realm of the present capabilities of the GCM we used in this study (CCSM4).

Higher concentrations of CO_2 appear to lower the calculated broadband albedo of planets with M-dwarf host stars (though the amount of reduced albedo decreases as CO_2 increases, as indicated by the flattening of the curve in Figure 3.14, bottom). For M-dwarf host stars, this may be largely due to increased CO_2 atmospheric absorption in the near-IR. However, increased Rayleigh scattering due to high-CO_2 concentrations is expected to lead to increases in planetary albedo, at least for G-dwarf host stars such as the Sun (Kasting & Ackerman, 1986). The effect of Rayleigh scattering could dominate atmospheric absorption at higher pressures. However, given that the effect of Rayleigh scattering is more pronounced for shorter-wavelength incident radiation, our decreased planetary albedos for higher-pressure atmospheres may be the consequence of atmospheric absorption masking high-albedo snow, given that Rayleigh scattering is less important on planets receiving higher percentages of long-wavelength radiation from their host stars (Kasting et al., 1993; Pierrehumbert, 2011; Kopparapu et al., 2013a,b). There may therefore be a particular stellar mass (somewhere between AD Leo and the Sun) above which the combined effects of Rayleigh scattering and atmospheric near-IR absorption are maximized. Indeed, we found that the broadband albedo of a K-dwarf planet also decreased with higher concentrations of CO_2, and by a smaller percentage than that of our M-dwarf planet. Here we have assumed a 1-AU equivalent flux distance for the M-dwarf planet, so the likelihood of CO_2 cloud formation in the atmosphere is low. Previous work with a 1-D radiative-convective model has suggested that CO_2 ice clouds in the atmosphere may result in net warming of a planet's surface (Forget & Pierrehumbert, 1997).

Given that the silicate weathering thermostat adjusts the CO_2 concentration to increase with decreasing surface temperature, and M-dwarf planets appear less sensitive to changes in instellation (as indicated by the shallower change in temperature and ice extent on the M-dwarf planet shown in Figures 3.3 and 3.4), habitable M-dwarf planets can be expected to exhibit lower concentrations of CO_2 at a given distance from their host stars than planets orbiting stars with higher visible and near-UV output, essentially requiring lower amounts of CO_2 in order to remain free of global ice-cover at lower values of instellation. We have not explored the effect of decreased CO_2 on the percent of the modern solar constant required for global ice cover on an M-dwarf planet using a GCM. Given the increased atmospheric stability in the troposphere of the M-dwarf planet receiving 73% of the modern solar constant compared to the G-dwarf planet receiving 92% of the modern solar constant (Figure 3.11), we expect the M-dwarf planet to be more resistant to global glaciation with decreased CO_2 than a G-dwarf planet, given an equivalent reduction in atmospheric CO_2 concentration. The difference between M-dwarf planets and planets orbiting hotter main-sequence stars becomes less noticeable at the outer edge of the habitable zone (where the masking effect of high CO_2 becomes more important) than closer in to the star (where CO_2 levels would be lower, and more ice would form on a planet's surface).

Our EBM simulations with 3-bar CO_2 atmospheres indicate that the spectral dependence of surface ice albedo is less important at the outer edge of the habitable zone, as planets remain free of planetary ice cover throughout the majority of the width of the habitable zone, due to large amounts of near-IR absorption by CO_2. We find that M-dwarf planets become ice-covered at $\sim$34% of the modern solar constant with 3 bars of CO_2 in their atmospheres, given the lowest-albedo ice surface. This value, while much smaller than that required for ice-covered conditions given Earth-like CO_2 levels (73% of the modern solar constant, from our GCM results), is still greater than the maximum CO_2 greenhouse limit, derived by Kasting *et al.* (1993) and updated by Kopparapu *et al.* (2013a; 2013b), of 25% of the modern solar constant for a planet orbiting an M0 star. It has been postulated that the OHZ may be 10-30% farther out from an M-dwarf star given the effect of the wavelength-dependent reflectivity of surface ice and snow on planetary albedo (Joshi & Haberle, 2012). However, CO_2 partial pressures of 10 bars or more may be required to maintain atmospheric

stability and surface liquid water at the outer edge of the habitable zone for M-dwarf stars (Wordsworth et al., 2011), and we have shown that high levels of atmospheric CO_2 entirely mask the climatic effect of surface water ice and snow. Therefore, we find the traditional outer edge of the habitable zone to be unaffected by the spectral dependence of ice and snow albedo.

We have shown here that planets orbiting cooler redder stars at equivalent flux distances exhibit higher global mean surface temperatures than planets orbiting stars with more visible and near-UV radiation output. Given that the SED of a host star influences the amount of instellation required for entrance into a snowball state, it stands to reason that exit out of a globally ice-covered state might also be subject to the influences of stellar spectrum, thus allowing us to place constraints on the climate stability of planets as a function of host star spectral class. We explore this prediction in the following chapter.

Chapter 4

APPLICATION II: PLANETARY DEGLACIATION

In this chapter, a GCM was used to explore the effect of the spectrum of a star on an orbiting planet's ability to deglaciate from globally ice-covered conditions. These simulations allowed us to quantify the amount of time required to generate habitable conditions on distant frozen planets that may be discovered in the future, as a function of the spectral type and evolutionary timescale of their host stars. The results presented here, in combination with those presented in Chapter 3 on the effect of stellar SED on the entrance into planetary ice cover, provide a comprehensive assessment of the effect of host star spectrum on climate stability. Portions of this chapter were originally published in collaboration with C. M. Bitz, V. S. Meadows, et al. in the April 2014 edition of Astrophysical Journal Letters (Shields et al., 2014, *ApJ*, Vol. 785, L9;), and are reproduced below with the permission of the American Astronomical Society.

4.1 Introduction

Planets orbiting beyond their host stars' habitable zones may exist in stable, globally ice-covered states (Budyko, 1969; Sellers, 1969), analogous to the "Snowball Earth" episodes (Kirschvink, 1992). As mentioned in Chapter 1, exit out of Snowball Earth is often attributed to the build-up of CO_2 in the atmosphere as a result of volcanic outgassing and decreased silicate weathering (Pierrehumbert et al., 2011). Given that the carbonate-silicate cycle on Earth is sensitive to plate tectonic speeds and mantle degassing rates (Driscoll & Bercovici, 2013), the efficiency of a similar mechanism on other planets may be variable. Without a continuously operating carbon cycle to stabilize the climate, planets may rely on the steady brightening of their host stars over time (Iben, 1967; Gough, 1981) to become hospitable for surface life. Such a scenario has been referred to as a "cold start" (Kasting et al., 1993).

In Chapter 3 we explored the effect of host star SED and ice-albedo feedback on the

susceptibility of orbiting planets to enter snowball states (Joshi & Haberle, 2012; Shields et al., 2013). We found that the large fraction of near-IR radiation received by M-dwarf planets renders them less susceptible to snowball episodes than their counterparts orbiting stars with higher visible and near-UV output. This is due to the lower albedo of ice and snow at near-IR wavelengths (Dunkle & Bevans, 1956), in addition to near-IR absorption by atmospheric CO_2, water vapor and clouds (Shields et al., 2013). Beginning with habitable surface temperatures and low planetary ice cover, a "warm start", much larger decreases in instellation were required to trigger snowball conditions on M-dwarf planets than G- or F-dwarf planets. This lower climate sensitivity, as indicated by smaller, more gradual increases in ice extent for a given decrease in instellation, indicated a greater stability against snowball episodes on M-dwarf planets.

Expanding on this previous work, here we explore a planet's climatic response from a "cold start" to *increases* in instellation as a function of the SED of its host star. From the point where the instellation is just low enough for a planet to freeze into a snowball state, the amount of resistance to melting by increasing instellation is a measure of the hysteresis. In climate science, the degree of hysteresis is explored by forcing a system in two directions to determine if multiple stable states could exist for a given forcing parameter. The amount of increased instellation required to melt a distant planet out of global ice cover as a function of host star SED has not been quantified, and we determine it here.

The range of instellations over which multiple stable equilibria are possible is representative of a planet's climate hysteresis. If a planet's hysteresis is high, its ice extent may remain at the equator despite significant increases in stellar flux. Once this resistance is finally overwhelmed, an abrupt change in ice extent may occur. Whether this would have a positive or negative influence on the development and evolution of life is under debate. Regardless, abrupt climate transitions could have important consequences for life, therefore knowing which planets are more likely to experience them, and which are likely to have more stable climates (with gradual climate transitions), will aid in target selection for follow-up missions.

This study examines how stellar SED influences climate stability, by comparing the amount of instellation required to melt out of a snowball state on planets orbiting M-, G-,

and F-dwarf stars (for details on our setup, see Chapter 2). We also compare how these planets exit a snowball with Earth's present level versus the maximum level of atmospheric CO_2 believed to exist at the end of Snowball Earth (0.1 bar, Pierrehumbert et al., 2011). We discuss the implications of our results for planetary habitability.

4.2 Results

Figure 4.1 shows the latitudinal extent of ice and global mean surface temperature on M-, G-, and F-dwarf planets as a function of percent of the modern solar constant (1360 W/m^2, i.e. the present insolation on Earth), assuming both warm- and cold-start conditions on aqua planets in our GCM (CCSM4). As described in Chapter 3 and Shields *et al.* (2013), the slopes of the lines from warm-start conditions are a measure of the climate sensitivity to decreases in instellation. The shallower slope of the M-dwarf planet's ice line latitude evolution indicates a lower climate sensitivity. While the F- and G-dwarf planets become ice-covered at 98% and 92% of the modern solar constant, respectively, when started in a warm state, global ice cover does not occur on the M-dwarf planet until its instellation has been reduced to 73% of the modern solar constant.

Upon reaching ice-covered conditions in our warm-start simulations, we then increased the instellation on all three snowball planets in intervals of roughly 1%. Open water first appears on the M-dwarf planet with a 9% increase in instellation, to 82% of the modern solar constant. The latitude of the ice line at this point is $\sim 36^\circ$. From that point on, both initial warm- and cold-start conditions yielded similar stable ice lines, as evidenced by the overlapping values at higher instellations for the M-dwarf planet in Figure 4.1. Mean ice line latitudes for warm- and cold-start conditions differed in latitude by less than 0.5° and 0.3° for the M-dwarf planets receiving 85% and 90% of the modern solar constant, respectively.

From a cold start, the G-dwarf planet does not exhibit a non-equatorial ice line until the instellation it receives has been increased by 14% (to 106% of the modern solar constant) relative to the instellation that brought it into a snowball state from a warm start, assuming fixed (PAL) CO_2. At this instellation, the ice line latitude has jumped from 0° to 69°. The F-dwarf planet does not exhibit non-zero ice lines until its instellation has been increased by 16% relative to the instellation that triggered global ice cover. At 114% of the modern solar

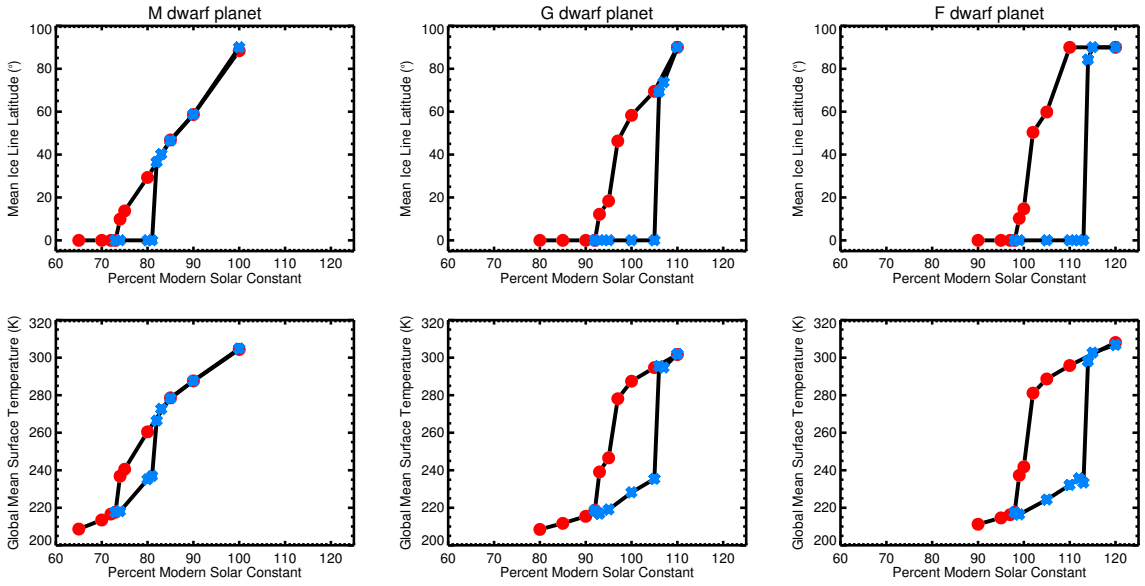

Figure 4.1 Mean ice line latitude (top) and global mean surface temperature (bottom) as a function of stellar flux for an aqua planet orbiting an M-, G-, and F-dwarf star. Simulations assuming an initial warm start are in red (circles). Initial cold start simulations are in blue (asterisks).

constant, the ice line latitude has jumped from 0° to ∼84°. Further increases in instellation yielded ice-free states for both warm- and cold-start conditions.

Figure 4.2 shows northern hemisphere winter surface albedo, cloud parameters and surface temperature on all three planets in hard snowball conditions, and just prior to deglaciating. Cloud radiative forcing is the TOA irradiance difference with and without clouds for the absorbed shortwave, outgoing longwave, or the net radiation. In the snowball state, the shortwave cloud forcing (SWCF) is slightly positive in austral summer over most latitudes because the clouds for all three planets absorb radiation, reducing the amount of shortwave radiation reflected by surface snow and ice (Cogley & Henderson-Sellers, 1984). The SWCF is most positive on the M-dwarf snowball planet, even though it is the least cloudy among the three cases. This is due to clouds absorbing more of the near-IR radiation emitted by the M-dwarf star.

Just prior to deglaciating, the surface albedo drops significantly from ∼20-50°S as the

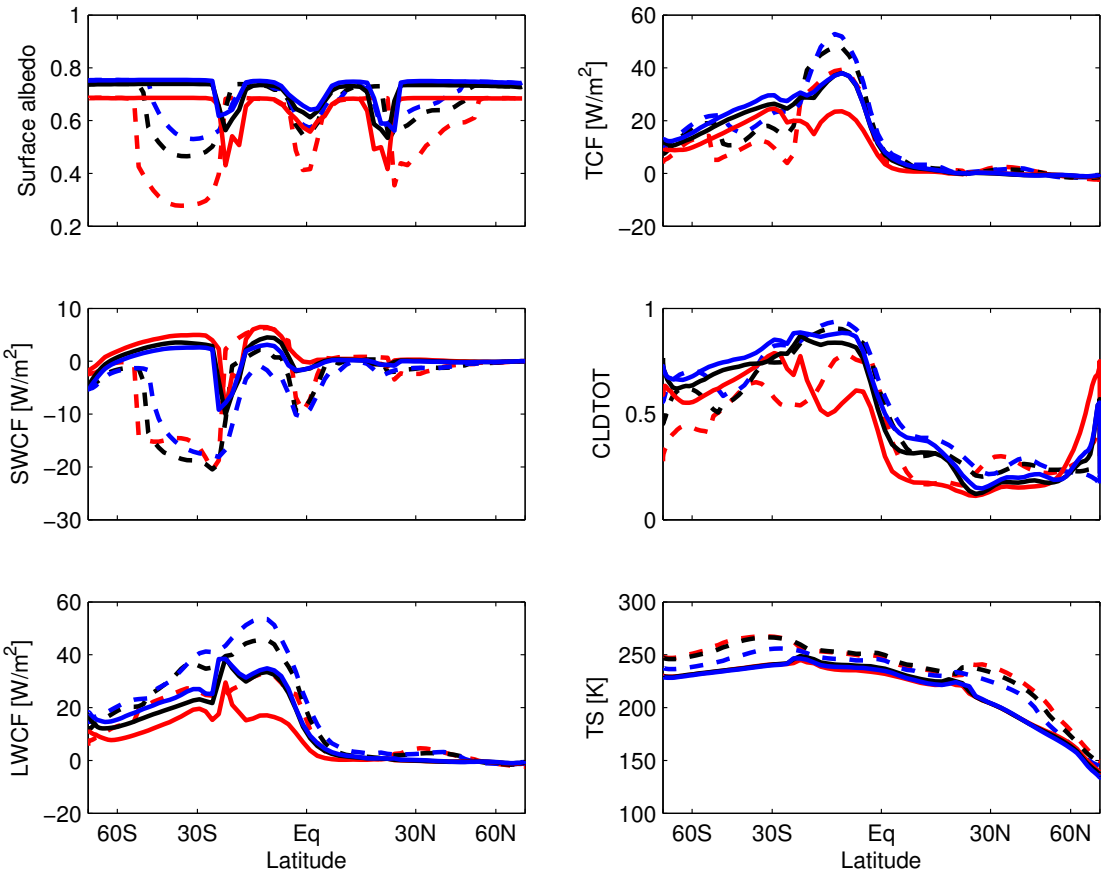

Figure 4.2 Northern winter (December/January/February, DJF) average surface albedo, shortwave (SWCF), longwave (LWCF), and total (TCF) cloud forcing, total cloud fraction (CLDTOT), and surface temperature (TS) versus sin of latitude for M-(red), G- (black) and F- (blue) dwarf planets in a snowball climate (solid) and prior to the appearance of open ocean (dashed).

snow sublimates or melts away in summer months. Here the shortwave effect of clouds is distinctly cooling due to scattering. Because cloud particles are relatively large compared to the wavelengths of radiation from all three stars, the scattering potential does not depend on the stellar SED. Instead, the amount of cloud cover and the surface albedo are the dominant factors controlling the SWCF. The SWCF is similar among the three planets from 20-50°S, owing to compensating effects. The M-dwarf planet is the least cloudy, however its surface is also the least reflective. Fewer clouds on the M-dwarf planet have just as sizeable of an

effect as greater cloud cover on the G- and F-dwarf planets.

The longwave (LWCF) and total (shortwave + longwave, TCF) cloud forcing tend to be smallest for the M-dwarf planet. This is due to the lower amount of cloud cover, which is a consequence of a squatter and weaker Hadley Cell compared to the other planets (Figure 4.3, Table 4.1). This weaker Hadley circulation stems from a more stable atmospheric temperature profile on the M-dwarf planet (Figure 4.4), and limits the transport of heat away from the tropics. This assists thawing in the tropics of the M-dwarf planet compared to the G and F-dwarf planets.

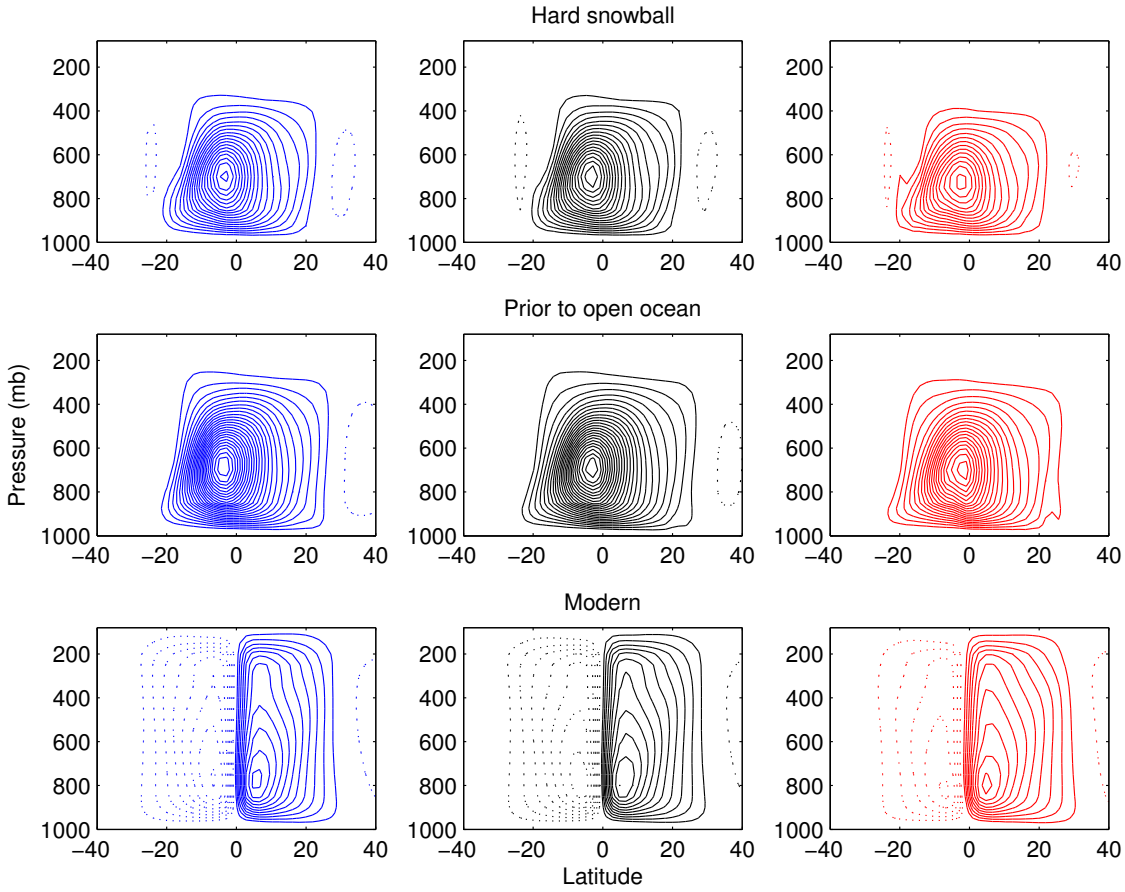

Figure 4.3 DJF Meridional stream function for M- (right), G- (center), and F- (left) dwarf planets with different climates. The contour interval is 25 x 10^9 kg/s. The zero contour interval is not shown. Dotted lines denote counterclockwise circulation.

Table 4.1 Boreal winter (DJF) maximum meridional stream function values for M- G-, and F-dwarf planets with different climates. Units are (kg s^{-1}) $\times 10^9$.

Stellar Type	snowball	prior to open ocean	modern
F-dwarf	459.24	644.95	280.74
G-dwarf	469.60	623.22	275.05
M-dwarf	357.29	489.26	260.50

We also compared the M- and G-dwarf response to raising CO_2 to 0.1 bar—the upper limit of CO_2 expected to build up in the atmosphere as a result of decreased surface temperatures on an ice-covered planet, assuming volcanic outgassing occurs while silicate weathering is inhibited (Walker et al., 1981). This value depends on volcanic outgassing and seafloor weathering rates (Le Hir et al., 2008), surface dust deposition (Le Hir et al., 2010), and model parameterizations (Pierrehumbert, 2004; Hu et al., 2011; Abbot et al., 2012). Regardless, the M-dwarf planet, which requires a much lower instellation to fully glaciate, exhibits a larger radiative response for the same CO_2 increase than the G-dwarf snowball planet receiving much larger instellation, yielding a 12% increase in TOA absorbed shortwave flux for a 250-fold increase in CO_2 concentration, compared with a 7% increase on the G-dwarf planet.

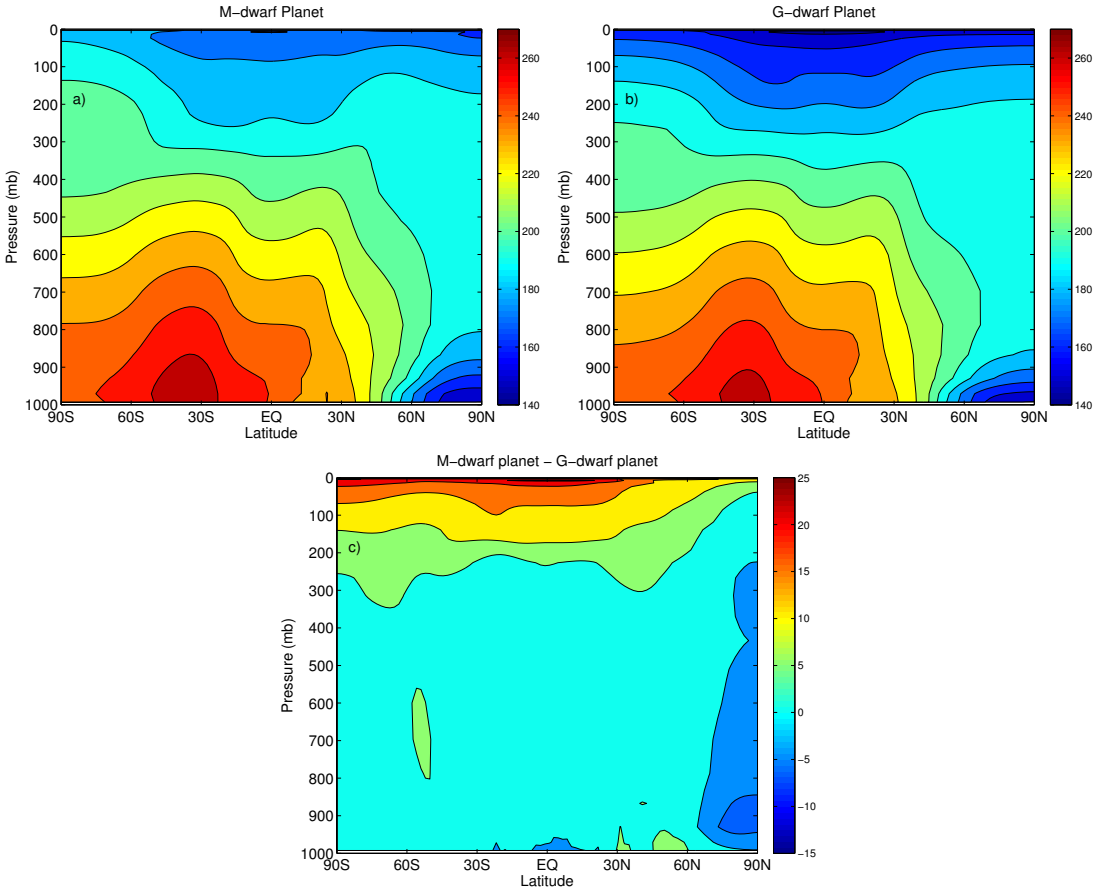

Figure 4.4 Zonal mean DJF vertical temperature for an (a) M- and (b) G-dwarf planet prior to deglaciating; (c) increase in vertical temperature of the M-dwarf planet, calculated by taking the difference between the M- and G-dwarf planets' atmospheric temperature profiles.

4.3 Discussion

The results of our model simulations indicate that the amount of increased instellation required to melt a planet out of a snowball state is highly sensitive to host star SED. The stability and evolution of a planet's climate is likely a function of the spectral properties of its host star.

The range of instellations over which multiple distinct ice line latitudes are possible is indicative of the level of climate hysteresis on these planets. At the upper end of the range

where multiple equilibria occur, the ice edge jumps from the equator to a poleward position. Above this point, a change in instellation yields comparable changes in ice edge for both warm- and cold-start initial conditions, arresting the multiplicity in stable climate states. M-dwarf planets have the smallest hysteresis and ice edge jump, G-dwarf planets exhibit intermediate ice edge jumps, and F-dwarf planets have the greatest jumps in ice line latitude and the largest climate hysteresis.

As a result of the longer-wavelength radiation emitted by the M-dwarf star, more radiation is absorbed by surface ice and atmospheric CO_2 and water vapor, which have strong absorption bands in the near-IR. The greater shortwave heating in the atmosphere of the M-dwarf planet reduces the amount of radiation reaching the surface, providing less relative heat to drive convection and rising plumes of air parcels at the equator. This weakens Hadley circulation on the planet. While the lower Hadley circulation suppresses cloud formation and lowers the total cloud forcing on the M-dwarf planet (which may oppose deglaciation), its larger effect is to reduce heat transport from the tropics to higher latitudes. This causes temperatures to rise above freezing in the sub-tropics and surface melting to occur. The G- and F-dwarf planets, with stronger Hadley circulation and enhanced cloud formation, demonstrated a greater tendency to remain in a snowball state despite increased instellation.

In non-snowball conditions the M-dwarf planet permits a stable ice line that is $\sim 33^\circ$ and $\sim 48^\circ$ closer to the equator than those of the G- and F-dwarf planets, respectively. As snowball deglaciation may be highly sensitive to surface albedo (Lewis et al., 2006), and to ocean-ice albedo differences (Abbot et al., 2011), the smaller difference in ocean-ice albedo contrast likely contributes to the lower stable ice line generated on the M-dwarf planet. We ran sensitivity tests with an energy balance model with albedos and atmospheric absorption determined from a line-by-line radiative transfer model (Meadows & Crisp, 1996), and found both the climate hysteresis and the latitude of stable ice lines to be lower for smaller ocean-ice albedo differences, and more sensitive to ice albedo differences than changes in atmospheric absorption. The inclusion of ocean heat transport, which has been shown to hasten the retreat of sea ice with increased instellation on M-dwarf planets (Hu & Yang, 2014), may increase the stable ice line latitudes that we have calculated here for the deglaciating M-dwarf planet.

We have assumed an eccentricity of zero and an Earth-like obliquity in this work. High-eccentricity planets receiving instellation from the Sun melt out of snowball states more easily (Spiegel et al., 2010). And planets with high obliquities (Williams & Kasting, 1997; Spiegel et al., 2009) or high-frequency obliquity oscillations (Armstrong et al., 2014) are less susceptible to snowball episodes. Therefore the trend of a smaller climate hysteresis for planets orbiting cooler stars may be further amplified at high obliquity and eccentricity.

Simulations with higher CO_2 resulted in a larger radiative response for the same increase in CO_2 on the M-dwarf snowball planet than on its G-dwarf counterpart. If a carbon cycle operates on distant planets, ice-covered M-dwarf planets would likely exhibit a greater atmospheric response to the steady build-up of volcanically-outgassed CO_2, and may require less CO_2 to deglaciate. This would lower the climate hysteresis of M-dwarf planets even further compared to planets orbiting brighter stars. Our fixed-CO_2 results therefore represent a lower limit on the difference in climate hysteresis as a function of stellar spectral type.

Climate hysteresis will affect the fraction of a planet's lifetime over which it can maintain habitability. As a main-sequence (core hydrogen-burning) star ages, its luminosity increases (Gough, 1981). Standard solar evolution models indicate that the Sun's luminosity has increased by ∼30% since its arrival on the main-sequence (Newman & Rood, 1977; Feulner, 2012). The Sun's luminosity is estimated to increase by ∼9% over the next billion years (Gough, 1981), and the 14% increase in instellation to melt out of global ice cover (in the absence of an active carbon cycle) would require 1.4 Gy of stellar evolution, assuming no significant changes to the atmospheric composition of the planet. This is approximately 13% of the main-sequence lifetime of the Sun (Sackmann et al., 1993).

M-dwarf stars, given their smaller masses (0.08-0.5 $M_\odot$), burn their fuel at much lower rates (Iben, 1967; Laughlin et al., 1997; Tarter et al., 2007) than G- or F-dwarf stars, and so brighten more slowly. Recent models of low-mass stellar evolution predict modest luminosity increases of ∼0.5-1% per billion years for a 0.4 $M_\odot$ star, depending on its age (Rushby et al. 2013; Andrew Rushby, priv. comm.). Given this range and the 9% increase in instellation required to generate open ocean on a frozen M-dwarf planet, thawing would occur in ∼9-18 billion years. However, this is less than 8% at most of the main-sequence lifetime of a 0.4 $M_\odot$ star (∼225 Gyr, Guo et al., 2009). Therefore a frozen M-dwarf planet would thaw out

earlier in the evolutionary path of its host star than ice-covered planets orbiting hotter, brighter stars, providing a longer timescale for biological evolution to evolve from frozen surface conditions.

Our work exploring the interaction between the spectrum of a host star and the atmosphere and surface of an orbiting planet has enabled us to quantify its effect on planetary climate. We are now ready to apply our tested methods to actual observed systems, and to examine the effect of additional star-planet interactions on our results. Our simulations thus far have assumed a single planet orbiting its star. As mentioned in Chapter 1, multiple-planet systems are more prevalent around lower-mass stars (Swift et al., 2013), and the presence of additional planetary companions can influence the orbital evolution of a planet in distinct ways (Mardling, 2007; Correia et al., 2012). In the next chapter, we explore how changes in the orbital dynamics of an observed multiple-planet system may affect the climate of the system's likeliest candidate for habitability, given what we have learned thus far about the interplay between stellar spectrum and planetary atmospheres and surfaces.

Chapter 5

METHODS II: INCORPORATING THE EFFECT OF PLANET MULTIPLICITY ON CLIMATE AND HABITABILITY

This chapter describes our method for exploring and assessing the habitability potential of observed planets in systems with additional planetary companions. A model is described that uses the transit timing data for planets in a system as input, and determines the location of each planet in a system at the same point in time. With this information an n-body model can be used to calculate the orbital evolution of all planets in a system over long timescales, and identify the maximum values of orbital parameters (such as eccentricity) for the most scientifically interesting planets in the system, without threatening the dynamical stability of the system itself. A climate model can then be used to explore the resultant possible climate range consistent with the orbital constraints of potentially habitable worlds in multiple-planet systems. This strategy enabled the application of the climate model methodology outlined in Chapter 2, and applied in Chapters 3 and 4 for theoretical single-planet systems orbiting stars of different spectral types, to actual observed multiple-planet systems. This is the first time that n-body models have been used to constrain 3-D climate model simulations. As a case study of these new techniques, we apply them to the potentially habitable planet Kepler-62f in Chapter 6.

5.1 Introduction

In Chapters 3 and 4 we used climate models to explore the effect on planetary climate of the interaction between the SED from different types of stars and a hypothetical, single orbiting planet. We found that the spectrum of a star, through its interaction with a planet's atmosphere and surface, can significantly affect the climate of an orbiting planet. But what if the star is host to multiple planets? How might the orbital changes that can be experienced by a planet in the presence of additional companions in the system (Mardling, 2007; Correia et al., 2012) affect that planet's climate and habitability? With the discovery

of numerous confirmed multiple-planet systems containing potentially habitable planets (Vogt et al., 2010; Muirhead et al., 2012; Swift et al., 2013; Anglada-Escudé et al., 2013; Quintana et al., 2014), it is crucial to develop a method to assess the range of possible climates of potentially Earth-like worlds in these systems. Given the dearth of available telescope time for follow-up exoplanet characterization, priority can then be given to the most promising candidates for habitable planets, with conditions likely to support surface liquid water.

As discussed in Chapter 1, planetary habitability depends on a number of factors that have been explored using climate models, including atmospheric composition (Pierrehumbert et al., 2011), host star spectral energy distribution (Shields et al., 2013, 2014), orbital dynamics (Spiegel et al., 2009, 2010; Armstrong et al., 2014), and planetary rotation rate (Yang et al., 2013, 2014). Here we develop a model that also includes the effect of planet multiplicity on habitability. By using the constraints from an orbital dynamics model as input to a climate model, we can use observational data to constrain the possible climate of a planet of interest in a multiple-planet system. Identifying the evolution of an orbital parameter such as eccentricity for input into a climate model will then allow us to understand the annual distribution of insolation on a planet (Hays et al., 1976; Berger et al., 1990), and to identify the habitable surface fraction (where surface liquid water may be possible) for different atmospheric compositions.

Here I describe my method for calculating the positions of multiple planets in a system at the same point in time using transit timing data. The output from this model is used as the primary input for an existing n-body model, which integrates the orbits of multiple planets in a system orbiting a central, dominant body (in this case a star). Output from the n-body model is then used as input to a GCM to run climate simulations (as outlined in Chapter 2) of the most scientifically interesting candidates for habitability in a given system. This is the approach we employ in Chapter 6 as a case study of the potentially habitable planet Kepler-62f.

5.2 HNBody: Modeling the Orbital Evolution of Multiple-Planet Systems

The Hierarchical N-Body (HNBody) package (Rauch & Hamilton, 2002), a set of software utilities we employed as our n-body model, integrates the orbits of astronomical bodies governed by a dominant central mass. It is based on the technique of symplectic integration, an n-body mapping method, developed by Wisdom and Holman (1991), and performs standard point mass orbital integrations for a given number of planets in a system.

In the n-body mapping method, the Hamiltonian—a mathematical function used to generate the equations of motion for a dynamical system—is the sum of the Keplerian and the interacting contributions to the motion of orbiting planetary bodies (Wisdom & Holman, 1991). The former describes the Keplerian motion of the orbiting planetary bodies around a central mass (the host star), and the latter describes the gravitational interactions between the planets themselves.

The evolution of the complete Hamiltonian is determined by alternately evolving the Keplerian and interacting parts separately in a sequence of steps leading to new n-body maps of the system, which are composed of the individual Keplerian evolution of the planets and the kicks due to the perturbations the planets inflict on one another. The output from HNBody consists of a series of data files that describe the evolution of selected orbital parameters over time. In the next section I describe the inputs that HNBody requires to generate this information, and the method employed to produce these necessary inputs.

5.3 HNBody: Model Inputs

While we know from transit timing data where each planet is relative to our line of sight when it transits its host star, we do not know where the other four planets (in the case of the Kepler-62 system) are at each planet's individual transit time. To analyze what might happen to these planets and their orbits as time progresses, we must determine the location of all planets at the same epoch (point in time) using a number of key equations. From this point, we can then begin orbit integration.

The Keplerian orbit of a planetary body can generally be described by a set of six parameters that characterize the orbit. The parameters we chose as input to HNBody for

each of the five planets in the Kepler-62 system were the semi-major axis a, the orbital eccentricity e, the inclination of the orbit i, the longitude of the ascending node Ω, the longitude of pericenter ω, and the true anomaly f (see Figure 5.1 and Table 5.1 for definitions of these parameters).

While a and i are constrained from transit observations of the Kepler-62 system (Borucki et al., 2013), e, Ω, ω, and f are not. Given the close proximities of planets 62b-e (0.05-0.43 AU), which are all within their tidal circularization orbital radii after 4.5 Gyr (Kasting et al., 1993), we assumed $e = 0$ for these inner four planets. Following from this assumption, ω is undefined given that the planets' orbits are assumed to be circular (there is no preferential pericenter, as all points along the orbit are equidistant from the star). We also assumed $\Omega = 0$ for all planets. This is reasonable given that $i \sim$89-90° for all planets, thus constituting an edge-on orbit capable of yielding a transit observable by the Earth. We determined the locations of Kepler-62b-e relative to Kepler-62f at the same point in time, assuming a range of possible eccentricities between 0 and 0.9 and a range of longitudes of pericenter ω between 0° and 2π° for Kepler-62f. In the following section I outline the equations that were used to generate the locations of all planets in the system, using transit data for these planets (Borucki et al., 2013), and the aforementioned values for the other orbital elements.

5.3.1 Putting the Planets on the Same Timeline

The location of a planet can be expressed in terms of the planet's true anomaly (see Figure 5.1), the longitude (angle) measured from the direction of the pericenter of the planet's orbit. I developed a method that uses the transit times for each of the five Kepler-62 planets and calculates the true anomaly values for all five planets at the same epoch, using one planet's location as a reference point.

As stated earlier, we do not have the eccentricities of the planets. The angular velocity and location of a planet in its orbit depends on its eccentricity, per Kepler's second law; therefore, we do not know the pericenter of each planet's orbit. We can determine what the true anomaly might be for a range of possible eccentricities for Kepler-62f. Here I outline the equations used in our model to generate the true anomaly values, given assumed values for other key orbital parameters.

Table 5.1 Orbital elements used to describe Kepler-62 planetary orbits. Angles here are in radians except for the orbital inclination, which is listed in degrees. In exoplanet geometry, $i = 90°$ constitutes an edge-on orbit capable of yielding a transit observable by the Earth. Data for the semi-major axis and the orbital inclination is from Borucki *et al.* (2013), though we have omitted the error bars here for ease of reading.

Parameters	Definition	Initial Values (Kepler-62b, 62c, 62d, 62e, 62f)
Semi-major Axis a (AU)	The planetary orbital distance from the star	0.0553, 0.0929, 0.120, 0.427, 0.718
Eccentricity e	The degree of ellipticity (oval shape) of an orbit ($e = 0$ - circular; $e = 1$ - parabolic)	0.0, 0.0, 0.0, 0.0, 0.0–0.9
Inclination i (°)	The angle between the planet's orbital plane and the sky plane	89.2, 89.7, 89.7, 89.98, 89.90
Longitude of Ascending Node Ω	The angle between a reference direction and the point of intersection between the plane of the orbit and the plane perpendicular to the reference direction (the sky plane)	0.0, 0.0, 0.0, 0.0, 0.0
Longitude of Pericenter ω	The angle between a reference direction and the point of closest approach of a planet to its star (pericenter)	0.0, 0.0, 0.0, 0.0, $0.0 \rightarrow 2\pi$ ($\Delta\omega = \pi/6$)
True Anomaly f	The angle between a radius vector through pericenter and the planet's location on an orbital ellipse around its host star	Calculated in Section 5.3

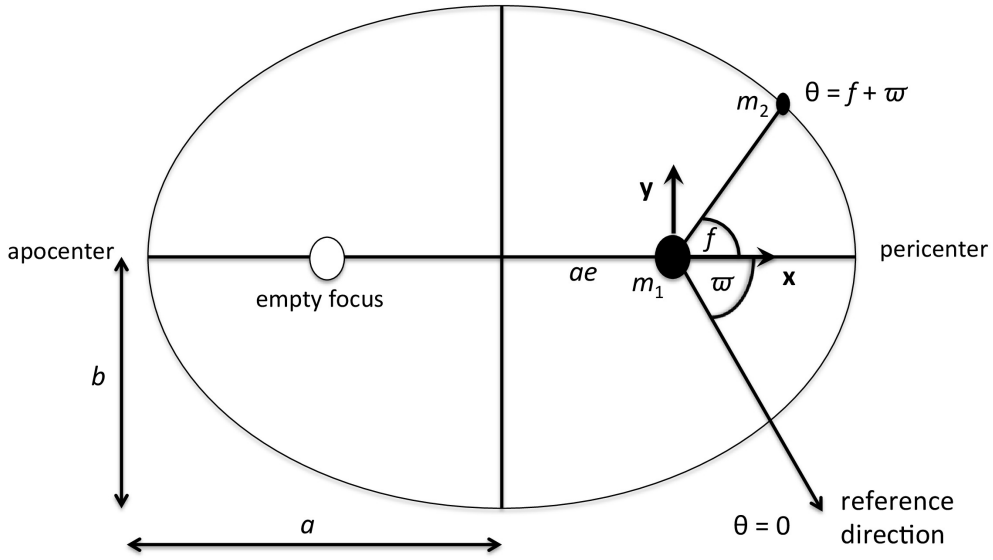

Figure 5.1 Geometry of the elliptical orbit of a body of mass m_2 around m_1, based on Figure 2.5 in *Solar System Dynamics*, C. D. Murray and S. F. Dermott, Cambridge University Press, pg. 27 (2000). The ellipse has semi-major axis a, semi-minor axis b, eccentricity e, and longitude of pericenter w. The true anomaly f denotes the angle subtended by an imaginary line connecting m_1 with the location of m_2 in its orbit and one connecting m_1 with pericenter (the point of closest approach to m_1).

5.3.1.a Time of pericenter passage

The time $t(f_i)$ that it takes for a planet to go from some initial reference point (to which it arrives at t_o) to the point of closest approach (where it arrives at t_{peri}), can be calculated using the following formula given by Sudarsky *et al.* (2005):

$$t(f_i) = \frac{-(1-e^2)^{1/2}P}{2\pi}\left\{\frac{esinf_i}{1+ecosf_i} - 2(1-e^2)^{-1/2}tan^{-1}\left[\frac{(1-e^2)^{1/2}tan(f_i/2)}{1+e}\right]\right\} \quad (5.1)$$

Taking the relation that $t(f_i) = t_o - t_{peri}$, we can rearrange (5.1) to yield an expression for t_{peri}:

$$t_{peri} = t_o + \frac{(1-e^2)^{1/2}P}{2\pi}\frac{esinf_i}{1+ecosf_i} - \frac{P}{\pi}tan^{-1}\left[\frac{(1-e^2)^{1/2}tan(f_i/2)}{1+e}\right] \quad (5.2)$$

To find each planet's true anomaly, we need to find a value, f_i, the location of each planet when it transits its star. Using Figure 5.1 for reference, if we assume that $\Theta = f + \omega = 0$ when the planet m_2 passes through the sky plane (the plane perpendicular to the reference direction), then at the time the planet passes behind the star, $\Theta = \pi/2$. By extension, the planet is in front of the star and transiting at $\Theta = 3\pi/2$. Therefore, for any value of ω, $f_i = 3\pi/2 - \omega$. Since we have assumed $\omega = 0$ for all planets except Kepler-62f, $f_i = 3\pi/2$ for these planets. Values of f_i for Kepler-62f varied depending on the value of ω. Values used in Equation (5.2) for the orbital period P, the transit time for each planet t_o, e, and f_i are given in Table 5.2. With these values, t_{peri} was calculated for each planet.

5.3.1.b From Mean Anomaly to True Anomaly

The location of a planet in its orbit around a central star can be described generally by three angular parameters: the *mean anomaly*, the *eccentric anomaly*, and the *true anomaly*. The mean anomaly is a function of the average angular velocity of the planet, and the time the planet takes to go from a reference point to the pericenter of its orbit, based on Kepler's first law. However, as it is dependent on the average orbital velocity, the mean anomaly does not give us a precise location of all five planets at one time, since not all orbits are circular. Rather, the calculation of the mean anomaly is a stepping stone to getting to the true anomaly, which gives us a precise location for each planet.

Table 5.2 Key parameters used as inputs to Eq. (5.2) for Kepler-62b-f.

	Kepler-62b	Kepler-62c	Kepler-62d	Kepler-62e	Kepler-62f
P (days)	5.714932	12.4417	18.16406	122.3874	267.291
t_o (BJD[1]-2454900)	103.9189	67.651	113.8117	83.404	522.710
e	0.0	0.0	0.0	0.0	0.0–0.9
f_i	$3\pi/2$	$3\pi/2$	$3\pi/2$	$3\pi/2$	$-\pi/2 \rightarrow 3\pi/2$

The mean anomaly M, is calculated using the following relation, taken from Murray and Dermott (2000):

$$M = n(t_o - t_{peri}) \tag{5.3}$$

where $n = 2\pi/P$. Here we used the location and transit time for Kepler-62f as the reference point t_o (see Table 5.2 for the value of t_o for Kepler-62f). This is a crucial step in getting the location of the other four planets at the time of Kepler-62f's transit.

The eccentric anomaly E is an angle measured from a line through the focus of the planet's elliptical orbit to the radius of a circle that passes through the pericenter of the ellipse. It is related to the mean anomaly and the orbital eccentricity e through Kepler's equation:

$$M = E - esinE \tag{5.4}$$

As this equation cannot be solved analytically, we solved it numerically following the method provided by Danby and Burkardt (1983). With calculated values of E for our assigned eccentricities, the true anomaly was calculated using the following relation:

$$f = 2tan^{-1}\left[\left(\frac{1+e}{1-e}\right)^{1/2} tan(E/2)\right] \tag{5.5}$$

With these values of f we had the locations of the other planets relative to Kepler-62f, and the sixth orbital parameter for input into HNBody. This allowed us to run accurate HNBody integrations for all possible values of e and ω for Kepler-62f, assuming circular orbits for the other four planets.

[1]BJD (Barycentric Julian Date) is the Julian date (the number of days since the beginning of the Julian period, ca. 4713 BC) corrected for Earth's changing position relative to the center of mass (barycenter) of the Solar System.

5.3.2 Planetary masses of the Kepler-62 system

HNBody also requires a seventh parameter as input—the planet's mass relative to its host star. As there are no R/V data on this system to accompany the transit data, the masses of all planets are unknown. There are several mass-radius relations in the literature, and we chose two, to explore the effect of planetary mass on the orbital evolution of the Kepler-62 system. We used the following mass-radius relation determined by Kopparapu *et al.* (2014) using data from the exoplanets.org database (Wright et al., 2011):

$$\frac{M_p}{M_\oplus} = 0.968(\frac{R_p}{R_\oplus})^{3.2}, \qquad M_p < 5M_\oplus \tag{5.6}$$

This yields a planetary mass of $\sim$3M$_\oplus$ for Kepler-62f. We also ran HNBody integrations with planet masses derived using the following mass-radius (for Kepler-62d, e, and f) and density ρ (for Kepler-62b and c) relations from Weiss *et al.* (2014):

$$\frac{M_p}{M_\oplus} = 2.69(\frac{R_p}{R_\oplus})^{0.93}, \qquad 1.5 \leqslant \frac{R_p}{R_\oplus} < 4 \qquad \text{(gaseous)} \tag{5.7}$$

$$\rho = 2.43 + 3.39(\frac{R_p}{R_\oplus}) \quad g/cm^3, \qquad R_p < 1.5R_\oplus \qquad \text{(rocky)} \tag{5.8}$$

The Weiss et al (2014) relationship resulted in higher masses for Kepler-62b and f, and lower masses for Kepler-62c, 62d, and 62e, compared to those using the Kopparapu *et al.* (2014) treatment. Finally, we ran additional orbit integrations with the maximum mass limits for all planets, as determined by Borucki *et al.* (2013). The masses for all five Kepler-62 planets used as input to HNBody integrations are given in Table 5.3.

Table 5.3 Masses (M$_\oplus$) used as inputs to HNBody for different sets of orbital integrations of the planets Kepler-62b-f.

Kepler-62b	Kepler-62c	Kepler-62d	Kepler-62e	Kepler-62f	Relation/Source
2.3	0.1	8.2	4.4	2.9	Kopparapu *et al.* (2014)
2.8	0.1	5.0	4.2	3.7	Weiss *et al.* (2014)
9.0	4.0	14	36	35	Borucki *et al.* (2013)

Additional model specifications include the preferred coordinate system, the class of particles (based on the scale of the masses and how their interaction is to be taken into

account), and the timestep and total length of integration. We specified a bodycentric coordinate system, which treats the system as dominated by the mass of the central star. We ran our HNBody integrations for "heavy weight particles" (which includes the dominant mass plus the planets) for 10^6 years, with a time step equal to 1/20th of the orbital period of the innermost planet in the Kepler-62 system. As Kepler-62b has an orbital period of 5.7 days, we used a time step of 0.29 days.

The evolution of the semi-major axis and eccentricity of the five planets were calculated over the prescribed length of integration of their orbits, and written to files at defined output intervals. We defined orbital stability as a successful integration in which stable, periodic amplitude oscillation was present for all planets throughout the entire million years, the energy was conserved to better than one part in 10^4, and no planets were ejected from the system. Eccentricities spanning the full range of stability for the outermost potentially habitable planet Kepler-62f were then used as input to our GCM. We then ran climate simulations of this planet with a variety of atmospheric compositions, orbital configurations and rotation rates to explore and assess its possible climate states, and to determine the best possible combination of these parameters for surface habitability. These results are presented in Chapter 6.

5.4 Climate Modeling of Kepler-62f: Model Inputs to CCSM4

Our primary goal in the climate modeling of Kepler-62f was to identify the most favorable combination of planetary parameters that would result in areas of the planet with warm enough surface temperatures for liquid water. To determine the best possible scenario for habitability, we varied the atmospheric composition, orbital eccentricity, planetary obliquity, the angle of the vernal equinox relative to pericenter, and the rotation rate of the planet in our GCM simulations.

Kepler-62f receives 41% of the modern solar constant from its star, therefore significant amounts of CO_2 may be required to keep temperatures above the freezing point of water on the surface. An active carbon cycle capable of generating increased amounts of atmospheric CO_2 in response to decreasing surface temperatures (Walker et al., 1981) would be a relatively straightforward means of maintaining habitable surface temperatures on the planet.

More than ∼2 bars of CO_2 could accumulate in the atmosphere of a planet with an active carbon cycle before the maximum greenhouse limit for CO_2 is reached (Pierrehumbert, 2010). Large increases in atmospheric CO_2 concentration begin to have significant effects on convection, and the manner in which it adjusts the temperature lapse rate on a planet. Additionally, CO_2 condensation becomes likely at levels of 1 to 2 bars, and collisional line broadening becomes important (Pierrehumbert, 2005). These effects are neglected in Earth-oriented GCMs such as CCSM4. We therefore assumed an Earth-like atmospheric CO_2 concentration (400 ppmv) in CCSM4, and used an additional GCM—the LMDZ Generic GCM—to simulate the climate of Kepler-62f with 1-12 bars of CO_2, as LMDZ contains parameterizations for addressing atmospheres with high-CO_2 content.

It was important to consider the possibility that Kepler-62f may not have sufficient atmospheric CO_2 to keep surface temperatures above freezing. We therefore explored alternate means of creating habitable areas of the planet with lower, Earth-like CO_2 levels. Given the effects of planetary obliquity (Ward, 1974; Williams, 1975) and eccentricity (Berger et al., 1993; Berger et al., 2006) on seasonality and annual global insolation, the best possible scenario for habitability in the low-CO_2 case may be one in which Kepler-62f has a high obliquity and a high eccentricity. Additionally, an orbital configuration in which the hotter, summer months in a given hemisphere coincide with the pericenter of the planet's orbit could amplify the effects of high obliquity and eccentricity. To test this prediction, we ran simulations with CCMS4, assuming an aqua planet as in Chapters 3 and 4, with a range of different values for these parameters.

We ran 30-year GCM simulations using CCSM4 with the input maximum initial eccentricity for stable HNBody integrations for Kepler-62f, $e = 0.32$ (see Chapter 6). We also ran additional simulations with $e = 0.0, 0.1$ and 0.2 to explore the effect of eccentricity on incoming stellar insolation and planetary surface temperature. We used a synthetic stellar spectrum from the Pickles Stellar Atlas (Pickles, 1998), with flux in the range of 1150-25000 Angstroms, and an effective photospheric temperature of 4887 K, which is close to the estimated effective temperature of Kepler-62 (4925 K, Borucki et al., 2013). As described in Chapter 2, the percentage of the total flux from the star was specified in each of the twelve incident wavelength bands in CAM4 (see Table 5.4).

We also ran 40-yr CCSM4 simulations with an Earth-like obliquity of 23°, and with an obliquity of 60°. To explore the influence of the location of summer solstice relative to pericenter, we varied the angle of the vernal equinox relative to the longitude of perihelion (VEP), which governs the difference in insolation between southern hemisphere summer and northern hemisphere summer. Because CCSM4 is parameterized for Earth-like conditions, we kept the radius and mass of the planet equal to those of Earth in these simulations. The orbital period was set equal to 365 days in our CCSM4 simulations instead of 267 days (the actual orbital period of Kepler-62f) so that our model would simulate a full annual cycle. As atmospheric radiative and convective adjustment timescales are short compared to either orbital period, we do not expect this to make much difference in the overall climate. A comparison of LMDZ sensitivity tests run with 267- and 365-day orbital periods showed negligible differences in global mean surface temperatures between the two cases. We used CCSM4 for continuity with our previous work, to evaluate the general trends in climate given changes in orbital parameters, and used LMDZ to simulate the climate of a planet with physical characteristics more closely like those of Kepler-62f. The details of the LMDZ GCM are given in the following section.

Table 5.4 CAM4 spectral wavelength bands specifying shortwave (stellar) incoming flux into the atmosphere, and the percentage of flux within each waveband for a synthetic spectrum of a K-dwarf star with a similar photospheric temperature to Kepler-62, from the Pickles Stellar Atlas (Pickles, 1998).

Band	λ_{min}	λ_{max}	K2V star % flux
1	0.200	0.245	0.128
2	0.245	0.265	0.075
3	0.265	0.275	0.054
4	0.275	0.285	0.056
5	0.285	0.295	0.070
6	0.295	0.305	0.091
7	0.305	0.350	1.076
8	0.350	0.640	27.33
9	0.640	0.700	6.831
10	0.700	5.000	64.35
11	2.630	2.860	0.000
12	4.160	4.550	0..000

5.5 Climate Modeling of Kepler-62f: LMDZ

We used a generic version of the "Laboratoire de Météorologie Dynamique" (LMD) GCM (Hourdin et al., 2006), developed to simulate a wide range of planetary atmospheres and climates. LMDZ[2] has been used in studies of the early climates of solar system planets (Forget et al., 2013; Wordsworth et al., 2013), and in previous studies of the climates of extrasolar planets (Wordsworth et al., 2011; Leconte et al., 2013).

Like CCSM4, LMDZ solves the primitive equations of fluid dynamics using a finite difference method and a 3-D dynamical core. The radiative transfer scheme is based on a correlated-k method, with absorption coefficients calculated from high-resolution spectra generated using the HITRAN 2008 database (Rothman et al., 2009). A smaller database of correlated-k coefficients was then generated from this spectra using 12x9x8 temperature (T=100, 150, ...600, 650 K, in 50 K steps), log-pressure (p=0.1, 1, 10, ..., 10^7 Pa), and water vapor mixing ratio (q_{H_2O}=10^{-7}, 10^{-6}, ..., 1) grids. These correlated-k coefficients ensure expedient radiative transfer calculations in the GCM. The spectral intervals included 38 shortwave bands and 36 longwave bands, with a sixteen-point cumulative distribution function for integration of absorption data within each band. The radiative transfer equation is then solved in each atmospheric layer using a two-stream approximation (Toon et al., 1989). Parameterizations for convective adjustment, and CO_2 collision-induced absorption are included based on work by Wordsworth *et al.* (2010). Simulations were run with a two-layer ocean, including a 50m-deep top layer and an underlying 200m-deep second layer. Both layers are assumed to be well-mixed, with horizontal diffusion used to approximate ocean heat transport by large-scale eddies (circular water currents). Adiabatic adjustment is also included, whereby the ocean lapse rate is adjusted to maintain a warmer top ocean layer at all times.

We ran our LMDZ simulations with a horizontal spatial resolution of 64x48 (corresponding to 5.625° longitude x 3.75° latitude), with 20 vertical levels. A blackbody spectrum with the stellar effective temperature of Kepler-62 (4925K, Borucki et al., 2013) was used as the

[2]The "Z" stands for "zoom" capability, as LMDZ includes a stretchable grid to allow for simulations of the Earth on both global and regional scales.

Table 5.5 Input parameters used in CCSM4 climate simulations of Kepler-62f. Here the parameter "VEP" is the angle of the vernal equinox relative to pericenter. Run7 is the synchronous rotation rate case, where the planet's rotation period is equal to its orbital period (1 day = 1 year).

Parameter	Run1	Run2	Run3	Run4	Run5	Run6	Run7
Orbital eccentricity	0.0	0.1	0.2	0.32	0.32	0.32	0.0
Obliquity (°)	23	23	23	23	60	23	0
CO_2 (ppmv)	400	400	400	400	400	400	400
H_2O	variable	variable	variable	variable	variable	variable	variable
Radius ($R_\oplus$)	1	1	1	1	1	1	1
Surface gravity (m/s^2)	9.8	9.8	9.8	9.8	9.8	9.8	9.8
Rotation rate	24 hrs	24 hrs	24 hrs	24 hrs	24 hrs	24 hrs	365 days
VEP (°)	90	90	90	90	90	0	90

host star spectrum. The albedo of snow was set to 0.55, and the albedo of sea ice was allowed to vary between a minimum of 0.20 and a maximum of 0.65, depending on ice thickness. We assumed an aqua planet with different amounts of atmospheric CO_2, water vapor that varied throughout each simulation according to evaporation and precipitation processes, a 267-day year, Earth-like (24-hr) and synchronous rotation rates, and eccentricities of 0 and 0.32. Input parameters for simulations using CCSM4 and LMDZ for our work on Kepler-62f are given in Tables 5.5 and 5.6. The results of these simulations, and the implications for the habitability of Kepler-62f are presented and discussed in the following chapter.

Table 5.6 Input parameters used in LMDZ climate simulations of Kepler-62f. Here the parameter "VEP" is the day of year when vernal equinox occurs relative to the day of year when the planet is at pericenter.

Parameter	Run1	Run2	Run3	Run4	Run5	Run6	Run7	Run8	Run9	Run10	Run11
Orbital eccentricity	0.32	0.00	0.32	0.32	0.32	0.32	0.32	0.00	0.00	0.00	0.00
Obliquity (°)	23.5	23.5	23.5	23.5	23.5	23.5	23.5	0.00	0.00	0.00	0.00
CO_2 (bars)	1	3	3	5	8	10	12	1	1	3	3
H_2O	variable	variable	variable	variable	variable	variable	variable	variable	variable	variable	variable
Radius ($R_\oplus$)	1.41	1.41	1.41	1.41	1.41	1.41	1.41	1.41	1.41	1.41	1.41
Surface gravity (m/s^2)	14.3	14.3	14.3	14.3	14.3	14.3	14.3	14.3	14.3	14.3	14.3
Rotation rate	24 hrs	24 hrs	24 hrs	24 hrs	24 hrs	24 hrs	24 hrs	24 hrs	267 days	24 hrs	267 days
VEP (day)	0	0	0	0	0	0	0	0	0	0	0

Chapter 6

CASE STUDY: THE HABITABILITY OF KEPLER-62F

In this chapter, the gravitational interactions between a star, a potentially habitable orbiting planet, and additional planetary companions in the system were explored to determine their effect on climate and habitability. We used a symplectic integrator to calculate the orbital evolution of the five-planet system orbiting the K-dwarf star Kepler-62, and a GCM to explore the potential climatic impact on the outermost planet and the system's most likely candidate for habitability, Kepler-62f. These simulations allowed us to apply the methods presented in Chapter 2, and employed in Chapters 3 and 4 for theoretical single-planet systems, to an observed system, and to determine the effect of planet multiplicity on our previous results. This work also allowed us to explore how changes in rotation rate affect planetary climate.

6.1 Introduction

NASA's *Kepler* mission (Borucki et al., 2006), launched in 2009, has identified over 4200 transiting planet candidates—nearly 1000 of which have been confirmed as planets—in its first five years of observations[1]. Recent statistical surveys estimate ∼40% of planetary candidates to be members of multiple-planet systems (Rowe et al., 2014). Analyses also suggest a low false-positive probability of discovery, indicating that the clear majority of these multiple-planet candidates are indeed real, physically associated planets (Lissauer et al., 2012, 2014). Analyses of the Kepler data have also shown that smaller stars are more likely to host a larger number of planets per star (Swift et al., 2013), and smaller planets are more abundant around smaller stars (Howard et al., 2012). These statistical data suggest that multiple-planet systems of small planets orbiting late-type stars are a major new planetary population, and one that is likely to be the first type of environment

[1]http://kepler.nasa.gov/ as of August 20, 2014

that we look at in the search for a habitable, Earth-like planet.

One of the systems of particular interest for habitability is the system orbiting Kepler-62 [Kepler Input Catalog (KIC) 9002278, Kepler Object of Interest (KOI) 701], a star of the K2V spectral class (temperature and luminosity between that of an M-dwarf star and the Sun). With a mass of $0.69M_{\odot}$ and a radius of $0.63R_{\odot}$, Kepler-62 hosts five planets—Kepler-62b-f—with orbital periods ranging from ∼5 to ∼267 days, and radii from 0.54 to $1.95R_{\oplus}$. The inclinations of all five planets are edge-on (i∼89-90°). However, neither their orbital eccentricities nor their planetary obliquities are constrained. The two outermost planets, Kepler-62e ($1.61R_{\oplus}$) and Kepler-62f ($1.41R_{\oplus}$), receive 120% and 41% of the amount of flux that Earth receives from the Sun, respectively. Kepler-62e, with an equilibrium temperature of ∼270 K without an atmosphere, is likely to be too hot (with an atmosphere) to have liquid water on its surface, unless it has a significant amount of cloud cover and is synchronously rotating. The cloud cover could increase the albedo of the planet at its substellar point; a proposed mechanism for cooling planets at or near the traditional inner edge of the habitable zone (Yang et al., 2013). Kepler-62f, given its low instellation, could sustain surface liquid water if its atmosphere has a large concentration of a greenhouse gas such as CO_2 (Kaltenegger et al., 2013).

While Kepler-62f has a radius of 1.41 $R_{\oplus}$, its mass is unknown, leaving its density also unconstrained. However, both transit and R/V observations of planets Kepler-36b (Carter et al., 2012), Kepler-10b (Batalha et al., 2011; Dumusque et al., 2014), and Corot-7b (Hatzes et al., 2011) have been combined to show that planets with radii smaller than $1.6R_{\oplus}$ have densities indicative of a rocky composition. A recent statistical survey of a population of Kepler planets with known masses (from companion R/V surveys) found that only planets with radii less than 2 $R_{\oplus}$ have a rocky composition (Marcy et al., 2014). And surveys with transit timing variation data have found that for planets with radii up to $R_p = 1.5R_{\oplus}$, density increases with planet radius, while above $1.5R_{\oplus}$, average planet density begins to rapidly decrease with increasing radius. This behavior indicates the presence of a larger volatile inventory for larger planets (Weiss & Marcy, 2014). Indeed, estimates based on measured planetary masses and radii, in concert with models of atmospheric evolution, identify the transition between rocky and gaseous planets to occur near $R_p = 1.75R_{\oplus}$ (Lopez & Fortney,

2013). Based on these results to date, as well as the lower amount of instellation received from its star at its present orbital distance compared to the high levels received by Kepler-62e (Borucki et al., 2013), Kepler-62f is the most likely candidate for a rocky, potentially habitable world in this system.

Previous work on the climate modeling of Kepler-62f found that 1.6-5 bars of CO_2 would yield surface temperatures above the freezing point of liquid water, depending on the planetary mass and surface albedo of the planet (Kaltenegger et al., 2013). However, this work was done using a 1-D radiative-convective atmospheric code, and neglected the presence of clouds (other than by a scaling of surface albedo). Additionally, the effect of the orbital architecture and evolution of this multiple-planet system on the climate of Kepler-62f was not explored. The eccentricity of a planet could be pumped to high values in the presence of additional companions in the system (Mardling, 2007; Correia et al., 2012). The effect of different rotation rates on atmospheric circulation was also not examined. With an orbital period of $\sim$267 days, tidal effects are expected to be weak, but could affect the rotation rate of the planet (Heller et al., 2011), therefore a variety of rotation rates is possible for Kepler-62f (Rory Barnes, priv. comm.). As changes in eccentricity will affect the amount of instellation received by a planet throughout its orbit (Berger et al., 1993; Berger et al., 2006), and planetary rotation rate has been shown to affect atmospheric circulation (Joshi et al., 1997; Merlis & Schneider, 2010; Showman et al., 2011; Showman & Polvani, 2011; Showman et al., 2013), quantifying the effect of orbital and rotational dynamics on the climate of Kepler-62f using a 3-D GCM is crucial to a more accurate assessment of its habitability.

In this chapter the effect of planet multiplicity on the eccentricity, climate, and habitability of Kepler-62f is explored, for different atmospheric compositions and planetary rotation rates. I developed a method that calculated the orbital locations of the other four planets in the system relative to the position of Kepler-62f, for a range of possible initial eccentricities and longitudes of pericenter for this planet. HNBody was then used to integrate the orbits of all five planets given different planetary masses, to identify the maximum eccentricity attainable by Kepler-62f while still maintaining stability within the planetary system (as described in Section 5.3). The potential habitability of this planet as a function of its stable

eccentricity was explored with a GCM, for atmospheres with Earth-like and high CO_2 levels, focusing on the presence of surface liquid water on the planet over an annual cycle.

6.2 Results

Figure 6.1 shows the fraction of stable orbital integrations performed using HNBody, assuming different initial eccentricities for Kepler-62f, and zero eccentricities for Kepler-62b-e. Here we define a stable integration as one in which no planets experienced large shifts in orbital distance leading to ejection from the system, the energy was conserved to better than one part in ten thousand, and eccentricity oscillations exhibited a regular period throughout the entire integration time (10^6 years). The maximum initial eccentricity for which stable integrations were possible for greater than 90% of the simulated longitudes of pericenter, was $e = 0.32$, assuming the Kopparapu *et al.* (2014) mass-radius relation. This value decreased by ∼3%, to $e = 0.31$, when the Weiss *et al.* (2014) mass-radius and density relations were used, and decreased by 28%, to $e = 0.23$, using the maximum mass limits for all planets (Borucki et al., 2013). The evolution of the eccentricities of all five planets for a stable integration at $e = 0.32$ for Kepler-62f is shown in Figure 6.2. All planets exhibited eccentricity oscillations—a characteristic of multiple-planet systems (Mardling, 2007)—with a regular period that remained constant over the entire 10^6-year integration. An integration assuming a higher initial eccentricity for Kepler-62f ($e = 0.34$) yielded eccentricity evolution that eventually settled into quasi-periodic oscillation after ∼500,000 years (Figure 6.3). However, due to the irregularity of the oscillatory motion for the first half of the simulation, the integration was deemed unstable, as significant orbital shifts occurred during that time. Consequently, we considered $0.0 \leqslant e \leqslant 0.32$ to be the maximum allowable range of initial eccentricities for Kepler-62f. We therefore ran simulations for $e = 0.0$, 0.1, 0.2, and 0.32 to explore the range of possible surface conditions for Kepler-62f as a function of eccentricity.

With an Earth-like atmospheric concentration of CO_2 (400 ppmv), all CCSM4 simulations of a planet with eccentricity $e = 0.00 - 0.32$ resulted in completely ice-covered conditions, with global mean surface temperatures below 190 K. Figure 6.4 shows the annual mean insolation as a function of latitude for these different eccentricities, assuming an obliquity of 23°. The average insolation over an annual cycle increases with eccentricity,

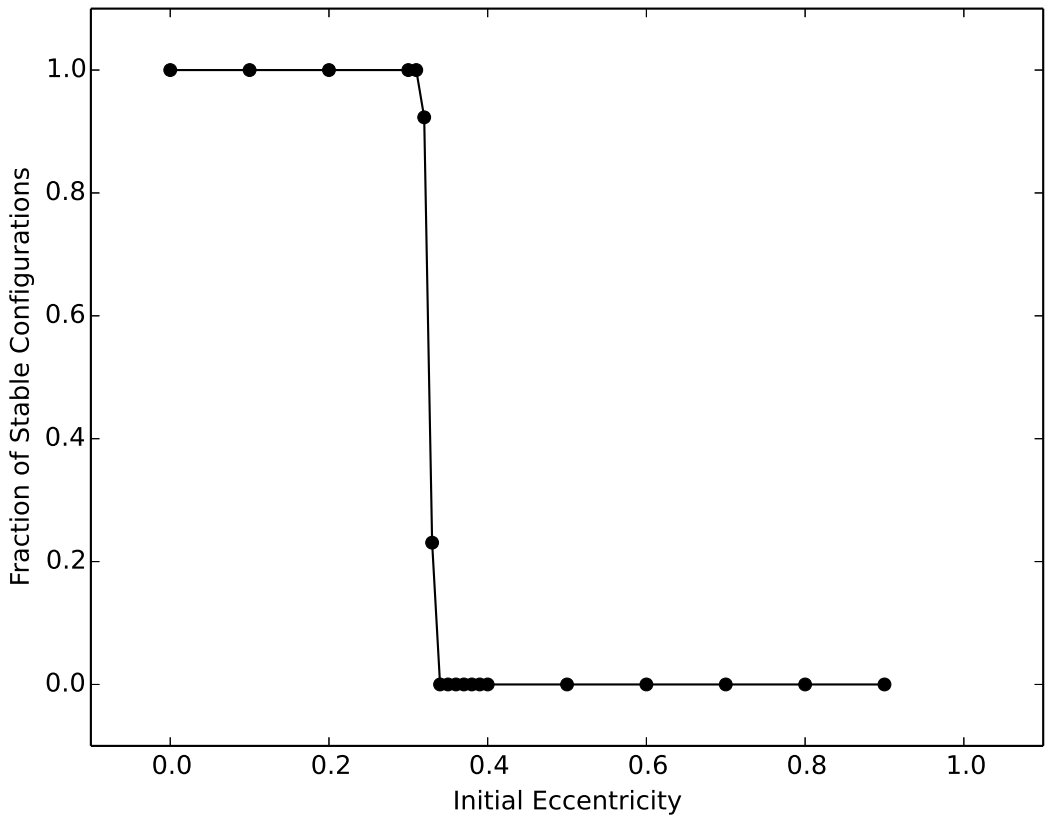

Figure 6.1 Fraction of stable configurations after a 10^6-yr HNBody integration for initial eccentricities between 0 and 0.9 for Kepler-62f, assuming the Kopparapu *et al.* (2014) mass-radius relationship. The eccentricities of all other planets in the Kepler-62 system were set to zero.

following Equation (1.5).

Since PAL CO_2 was clearly insufficient to yield habitable surface temperatures for Kepler-62f at its value of incoming stellar flux, we ran simulations using LMDZ with large amounts of atmospheric CO_2 and the highest possible eccentricity for Kepler-62f that satisfied our stability criteria. Figure 6.5 shows the surface temperature as a function of latitude and longitude for an LMDZ simulation with 3 bars of CO_2, variable water vapor, and $e = 0.32$. With a global mean surface temperature of 271 K, ∼34% of the planet is ice-

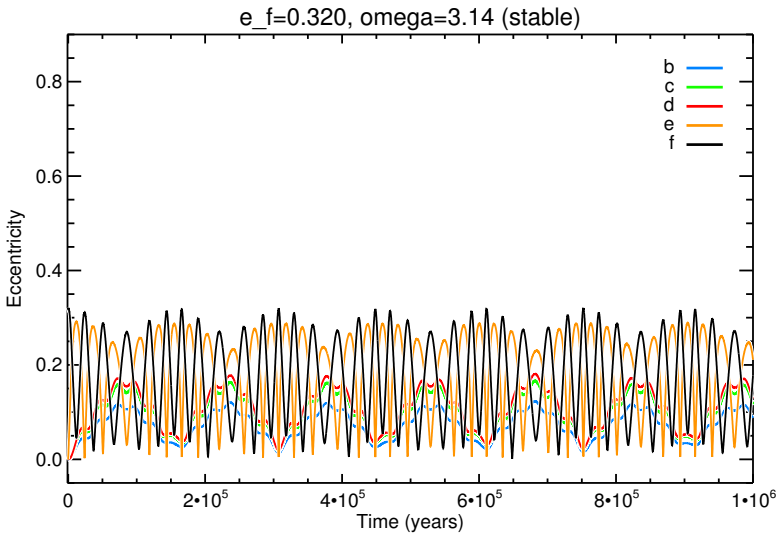

Figure 6.2 Evolution of the eccentricities of Kepler-62b-f as a function of time calculated with HNBody. Initial eccentricities and longitudes of pericenter for Kepler-62b-e were set to zero. The initial eccentricity of Kepler-62f was set to 0.32 with a longitude of pericenter equal to π.

covered. However, there is a wide swath of open water in the tropics where temperatures are solidly above freezing. Simulations run at $e = 0$—the lower limit of the stable range of initial eccentricities for Kepler-62f—resulted in a lower global mean surface temperature by $\sim$5 K, and $\sim$10% more sea ice cover on the planet (Figure 6.6).

If Kepler-62f has an active carbon cycle, depending on the silicate weathering rate on the planet, higher levels of CO_2 may be expected to accumulate in the planet's atmosphere prior to reaching the maximum greenhouse limit (Kopparapu et al., 2013a,b). We ran simulations using LMDZ with CO_2 concentrations of up to 12 bars, and let the amount of water vapor vary (through evaporation and precipitation) during the course of each simulation. Global mean, minimum, and maximum surface temperatures for each simulation are plotted in Figure 6.7. Surface temperature increases with CO_2 concentration up to 10 bars, where the global mean surface temperature is 303.9 K, and the maximum temperature reached is 313.1 K. At 12 bars of CO_2, the global mean surface temperature has decreased by 0.4 K, and the maximum temperature reached on the planet has decreased by $\sim$2 K. This implies that

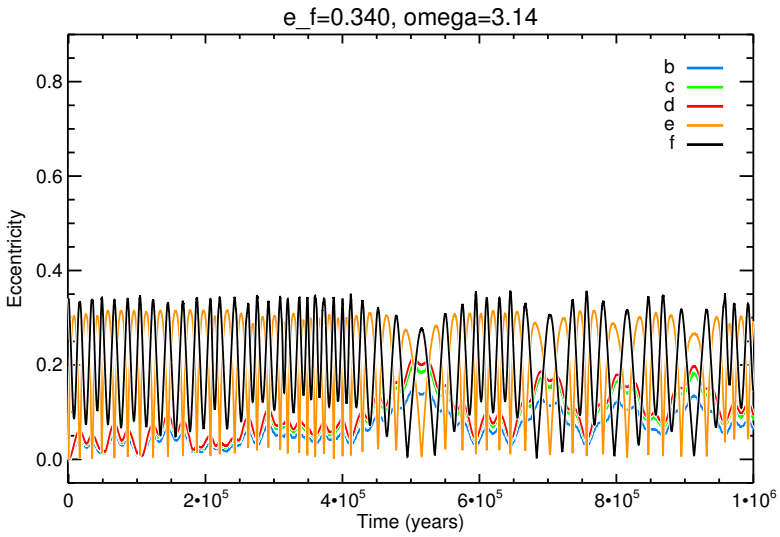

Figure 6.3 Evolution of the eccentricities of Kepler-62b-f as a function of time calculated with HNBody. Initial eccentricities and longitudes of pericenter for Kepler-62b-e were set to zero. The initial eccentricity of Kepler-62f was set to 0.34 with a longitude of pericenter equal to π. Significant orbital shifts occurred during the first 500,000 years of the model integration as indicated by the irregular amplitudes of oscillations, shown here. This rendered the integration unstable for the planetary system.

at this level of atmospheric CO_2 we have reached the point where the effects of Rayleigh scattering begin to dominate over the greenhouse effect of CO_2.

High amounts of CO_2 would be a relatively straightforward means of generating habitable surface temperatures on a planet receiving low instellation from its star. However, the efficiency of the carbonate-silicate cycle—which has been shown to be sensitive to a variety of factors, including the mantle degassing rate of a planet (Driscoll & Bercovici, 2013)—is unknown for Kepler-62f. If the planet has a low amount of CO_2 in its atmosphere, and lacks an active carbon cycle to adjust the silicate weathering rate with temperature (Walker et al., 1981), the fraction of habitable surface area may decrease significantly compared to our simulated cases with 3 bars and higher CO_2.

We therefore explored different orbital configurations which could improve conditions for habitability on a planet that did not have an effective means of increasing its concentration of greenhouse gases. Since we do not know the location of pericenter for the orbit of

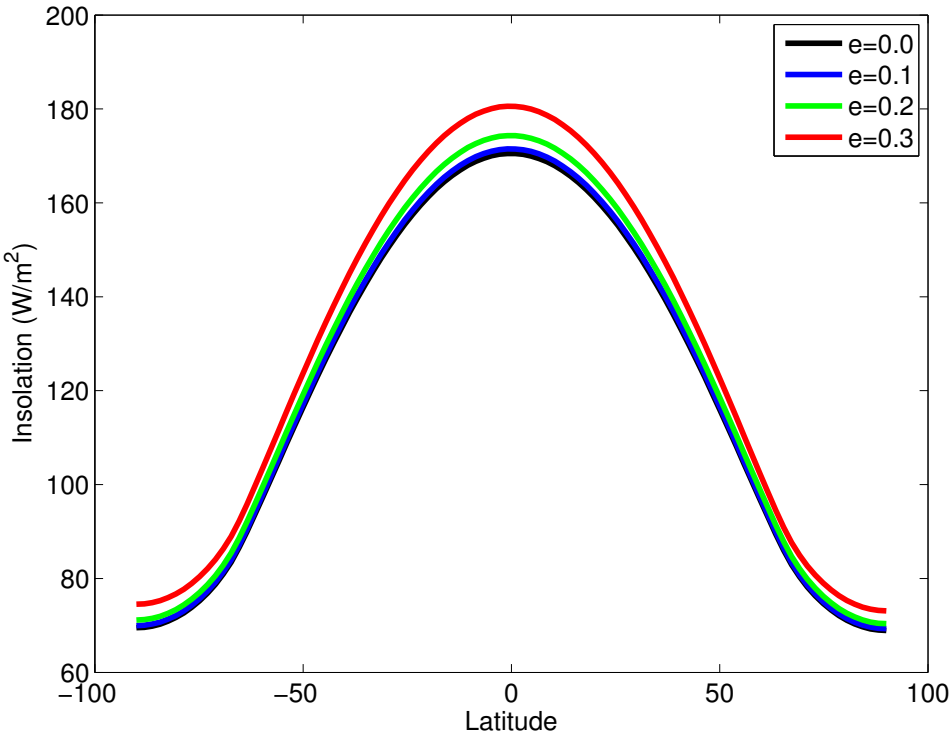

Figure 6.4 Insolation as a function of latitude for Kepler-62f, after a 30-year CCSM4 simulation, assuming $e = 0.0$ (black), $e = 0.1$ (blue), $e = 0.2$ (green), and $e = 0.32$ (red). The plots show 12-month averages. The obliquity of the planet was set to 23°. The angle of the vernal equinox relative to pericenter was set to 90°, similar to the Earth (102.7°). The larger the eccentricity, the larger the annually-averaged insolation received at a given latitude.

Kepler-62f, we explored the effect on insolation due to changes in the angle of the vernal equinox relative to the location of the pericenter (VEP) of a planet's orbit, as this can affect the hemispherical annually-averaged insolation on a planet. Figure 6.8 shows the results of simulations assuming a VEP of 0° and 90°, with the obliquity held fixed at 23°. At VEP=0°, the point where both hemispheres receive equal amounts of insolation coincides with the planet's closest approach to its star. The difference in monthly insolation is relatively small in the southern hemisphere, as it receives equal insolation to that received by the northern hemisphere at pericenter. At an angle of 90°, the southern hemisphere receives a significantly higher percentage of insolation compared to the northern hemisphere during its

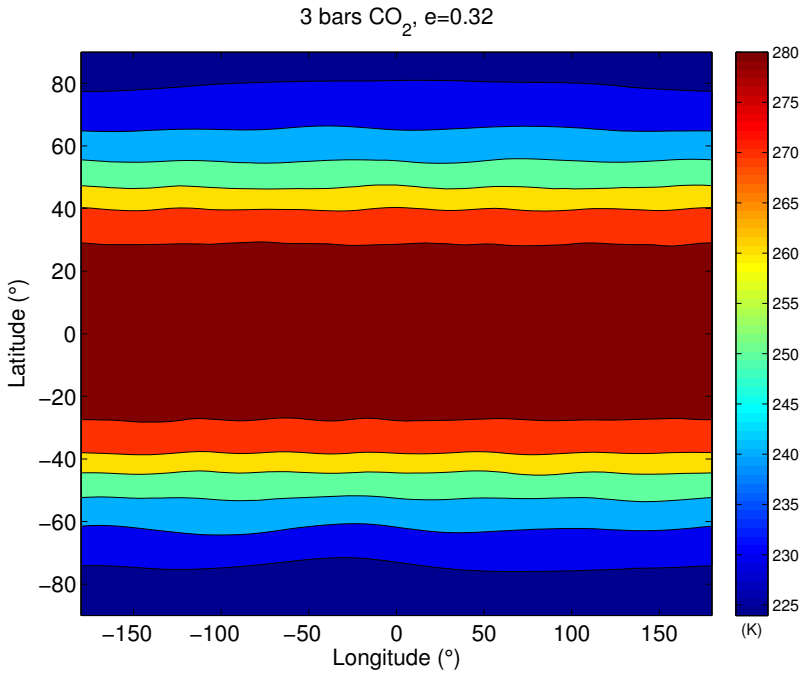

Figure 6.5 Surface temperature as a function of latitude for Kepler-62f after a 40-year LMDZ simulation, assuming $e = 0.32$, an obliquity of 23.5°, and 3 bars of CO_2. The angle of the vernal equinox relative to the pericenter (VEP) of the planet's orbit is 0°.

summer months when the planet is at or near pericenter. Because of the planet's obliquity, this is when the southern hemisphere is angled toward the star.

The obliquity of Kepler-62f is observationally unconstrained, so we also explored how different obliquities might affect the planet's climate. As shown in Figure 6.9, at an obliquity of 60°, the high-latitude regions of the planet receive more insolation than the tropics. The global mean surface temperature is still significantly below freezing at both of the simulated obliquities (23° and 60°), given the Earth-like CO_2 levels and low stellar flux. However, surface temperatures do get above freezing in the southern hemisphere during its summer months in the high-obliquity case. This is because the VEP has been set to 90°. This means that summer in the southern hemisphere occurs near the planet's closest approach to its star, as shown in the schematic diagram in Figure 6.10. This results in higher annual mean surface temperatures in this hemisphere during its summer months, compared to the

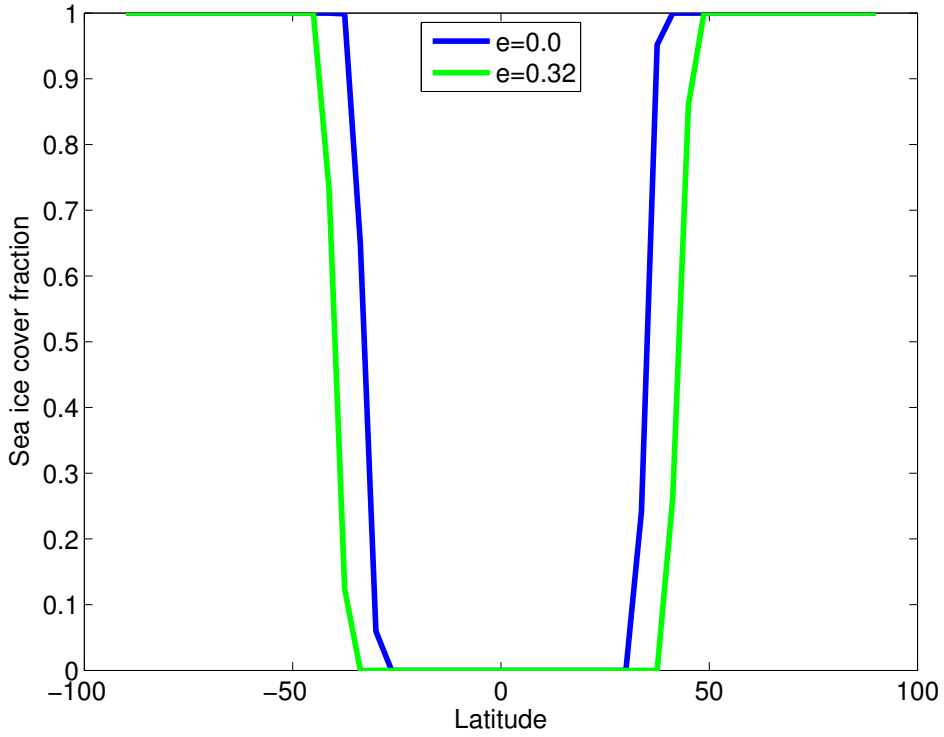

Figure 6.6 Sea ice cover fraction as a function of latitude for Kepler-62f for the minimum and maximum stable initial eccentricities possible for Kepler-62f, after a 40-year LMDZ simulation, with 3 bars of CO_2 in the atmosphere. An obliquity of 23.5° and VEP = 0° is assumed.

northern hemisphere. An orbital configuration that places the summer solstice near the pericenter of the planet's orbit could therefore amplify the effects of high obliquity and eccentricity, and cause surface melting to occur during an annual cycle.

Given that Kepler-62f could have a wide range of rotation periods, including a synchronous rotation rate (Rory Barnes, priv. comm.), using CCSM4 and LMDZ we ran simulations of the planet assuming an Earth-like rotation rate (24 hrs), and a synchronous rotation period, for 400 ppmv (Earth-like), 1-bar, and 3-bar CO_2 atmospheres, with both the eccentricity and obliquity set to zero. Our CCSM4 simulations with Earth-like CO_2 levels were completely ice covered. Figure 6.11 shows the surface temperature as a function of latitude and longitude for the LMDZ 1-bar and 3-bar CO_2 cases. The synchronous case with 1-bar of CO_2 has a global mean surface temperature of ∼207 K, with 99.6% of the

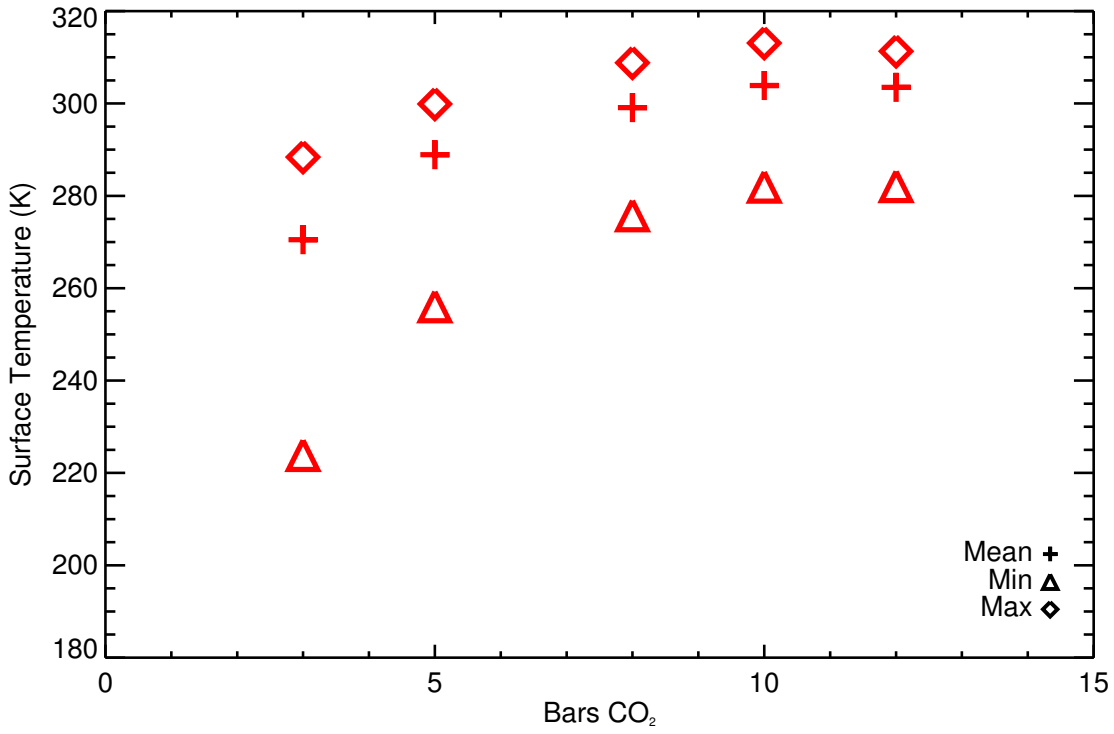

Figure 6.7 Mean (plus symbols), minimum (triangles), and maximum (diamonds) surface temperature for Kepler-62f, assuming $e = 0.32$, an obliquity of 23.5°, and different levels of atmospheric CO_2. The mean values take into account the location of measured surface temperature values relative to the total surface area of the planet. An obliquity of 23.5° and VEP = 0° is assumed.

planet covered in ice. There is a small circular region of open water at the substellar point on the planet (Fig. 6.11). The non-synchronous case with the same CO_2 level has a global mean surface temperature that is ∼35 degrees warmer (∼241 K), with ∼65% of the planet covered in ice. The 3-bar CO_2 cases, while ∼30-40 K warmer, exhibit a similar trend, with the non-synchronous case yielding a global mean surface temperature (∼273 K) that is ∼25 K warmer than the synchronous case (∼248 K).

We also compared the cloud cover fraction for the 1-bar CO_2 simulations. As shown in Figure 6.12, ∼81% of the day side of the synchronously-rotating planet is covered by clouds, compared with ∼53% of the planet with a 24-hr rotation period. This is due to the larger

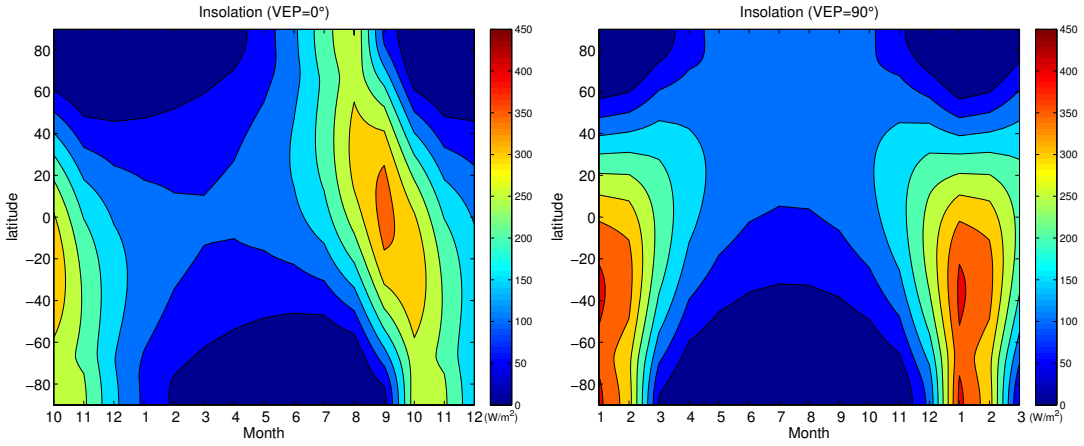

Figure 6.8 Annual mean insolation as a function of latitude for Kepler-62f as a function of the month of the year after a 30-year CCSM4 simulation, assuming a 12-month annual cycle and a VEP of 0° (left), and 90° (right). The obliquity and eccentricity of the planet was set to 23° and 0.32, respectively.

amount of instellation received at the planet's non-varying substellar point, which is ocean-covered. This causes strong convection leading to large amounts of water cloud cover, resulting in a higher planetary albedo (Yang et al., 2013). We found that the planetary albedo was 30% greater on the day side of our simulated synchronously-rotating planet compared to the planet with an Earth-like rotation rate (0.48 vs. 0.37, respectively). This causes more radiation to be reflected back to space by the planet, and leads to cooler surface temperatures compared to the non-synchronous case.

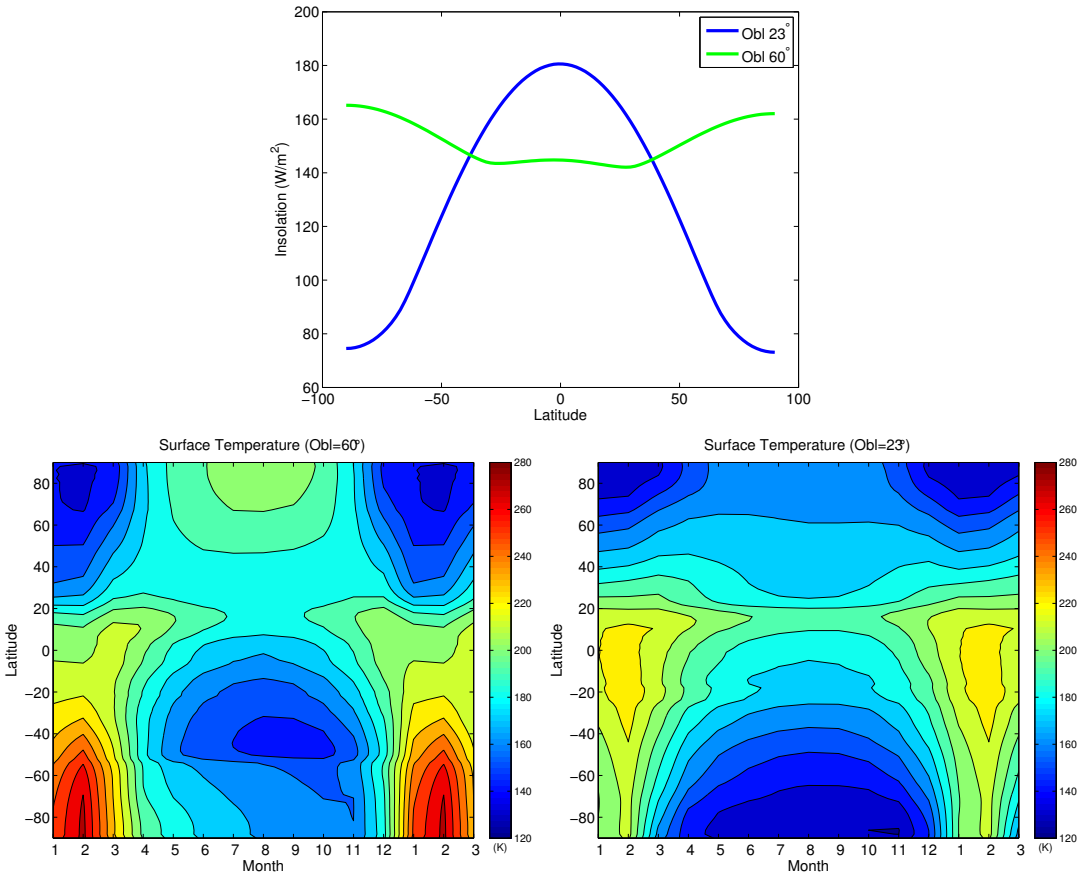

Figure 6.9 Top: Annual mean insolation as a function of latitude for Kepler-62f after a 40-year CCSM4 simulation, assuming an obliquity of 23° (blue) and 60° (green). Bottom: Surface temperature as a function of the month of the year, assuming a 12-month annual cycle, for an obliquity of 60° (left) and 23° (right). Here VEP was set to 90°, similar to the Earth (102.7°). The eccentricity was set to 0.32.

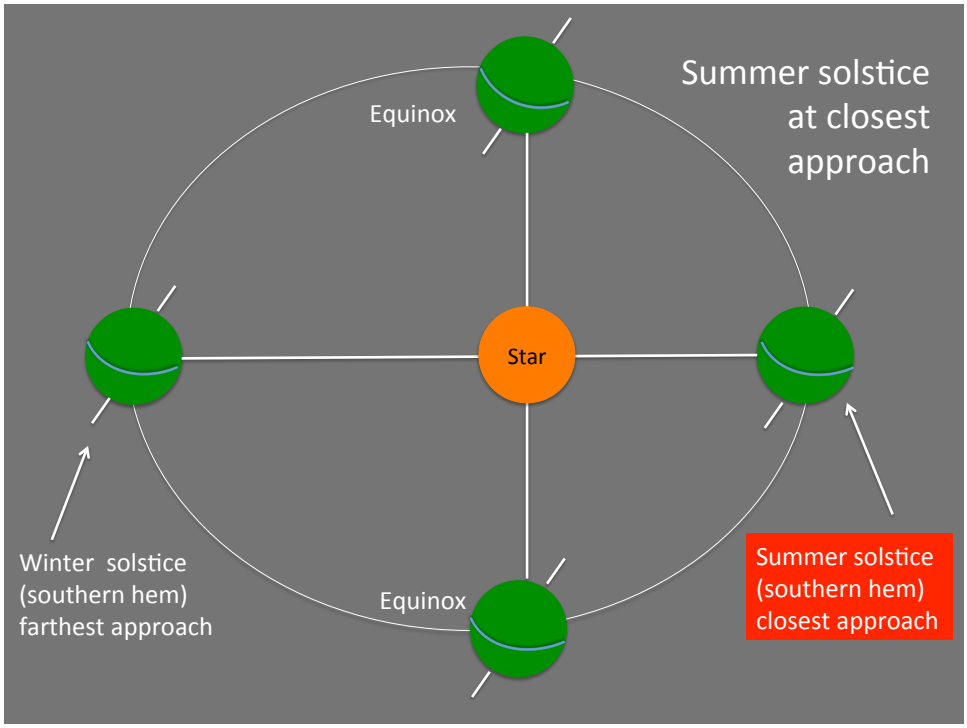

Figure 6.10 Schematic diagram of assumed orbital configuration for CCSM4 simulations of Kepler-62f. The angle of the vernal equinox with respect to pericenter was set to 90°, similar to the Earth (102.7°).

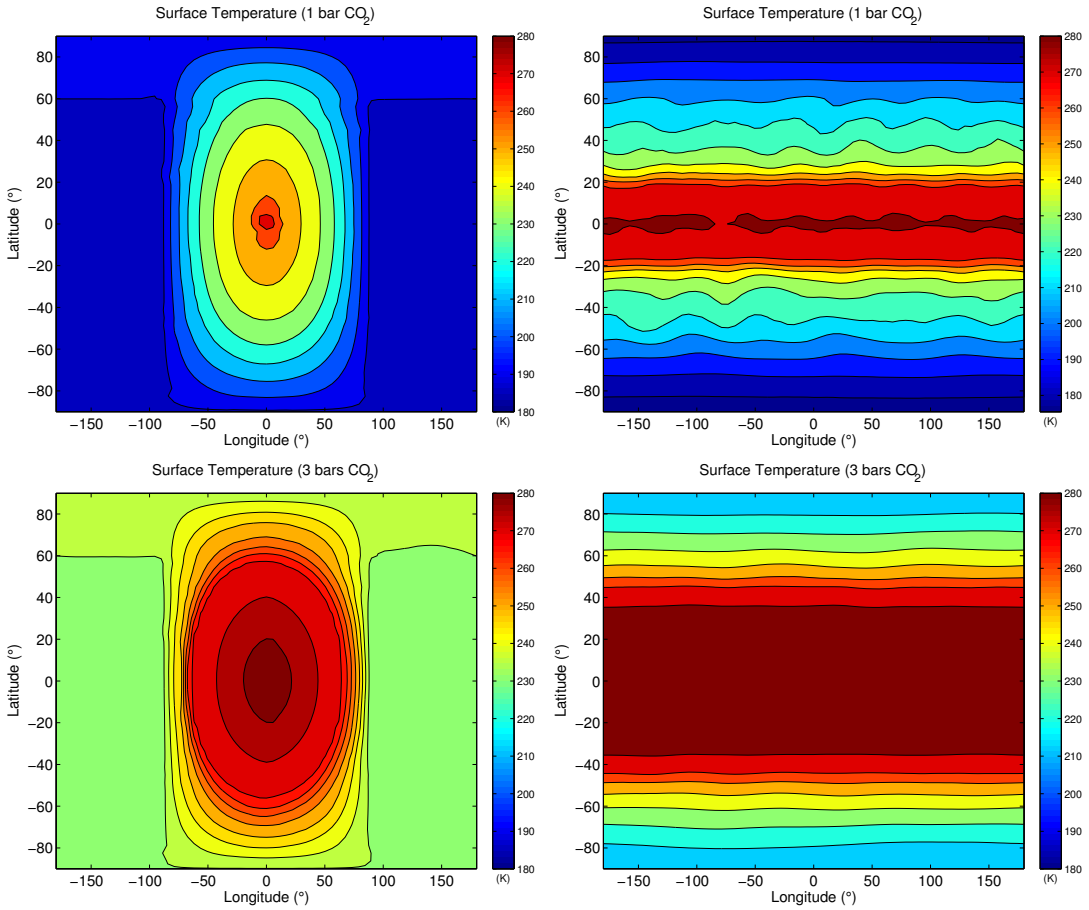

Figure 6.11 Surface temperature for a synchronous (left) and Earth-like (24-hr) rotation rate for Kepler-62f, after a 20-year LMDZ simulation with 1 bar (top) and 3 bars (bottom) of CO_2 in the atmosphere. We assumed $e = 0$, VEP $= 0°$ and an obliquity of $0°$ for both simulations.

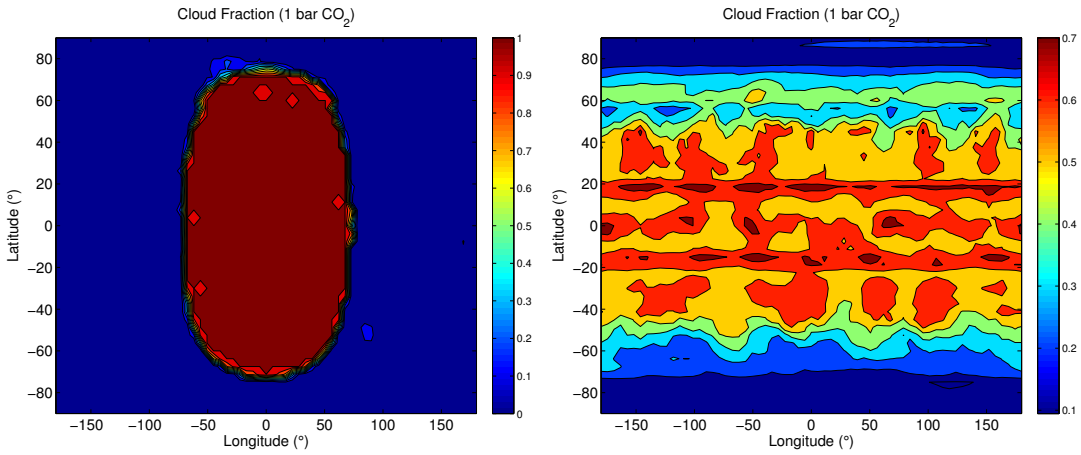

Figure 6.12 Cloud fraction for a synchronous (left) and an Earth-like, 24-hr (right) rotation rate for Kepler-62f, after a 20-year LMDZ simulation with 1 bar of CO_2 in the atmosphere. We assumed $e = 0$, VEP $= 0°$, and an obliquity of $0°$ for both simulations.

6.3 Discussion

Using n-body orbit integrations, we have identified the maximum initial eccentricity possible for Kepler-62f while maintaining dynamical stability, and find that at this value of eccentricity ($e = 0.32$), with 3 bars of CO_2 in its atmosphere, Kepler-62f exhibits surface temperatures above the freezing point of water over a large fraction of the planet. Our simulations with $e = 0$, yielding slightly lower maximum surface temperatures, are consistent with average insolation decreasing with decreasing eccentricity. However, surface temperatures are still clement on the planet at $e = 0$. This indicates that if Kepler-62f has an active carbon cycle, where CO_2 is allowed to build up in the atmosphere as silicate weathering decreases at lower surface temperatures (Walker et al., 1981), Kepler-62f could yield habitable surface conditions over more than 50% of the planet for the full range of gravitationally stable eccentricities possible, $0 \leqslant e \leqslant 0.32$. The maximum CO_2 greenhouse limit for stars with the effective temperature of Kepler-62 occurs at a stellar flux[2] that is well below that received by Kepler-62f (41% of the modern solar constant, Borucki et al., 2013). Given that 3 bars of CO_2 is significantly below this limit (∼7-8 bars, Kopparapu et al., 2013a,b), this level of CO_2 is plausible for this planet.

Our simulations with higher levels of CO_2 resulted in increasingly higher surface temperatures on the planet, up to a level of ∼10 bars. At 12 bars of CO_2, temperatures began to decrease, indicating that the greenhouse effect was no longer sufficient on its own to maintain habitable surface temperatures. CO_2 is 2.5× more effective as a Rayleigh scatterer than Earth's air (Kasting, 1991; Forget & Pierrehumbert, 1997), and this behavior likely contributes to the loss of warming at higher CO_2 concentrations (Kasting, 1991; Kasting et al., 1993; Selsis et al., 2007). Given that we assumed a VEP of 0° in all of our LMDZ simulations, and our CCSM4 simulations resulted in higher surface temperatures in the summer hemisphere with a higher VEP of 90° compared to 0°, surface temperatures can be expected to increase relative to the results presented here if Kepler-62f has a VEP like the Earth's, along with a moderate to high obliquity, which will increase seasonality on the planet.

---

[2] ∼30% of the modern solar constant (Kopparapu et al., 2013a,b)

We have not included the effect of CO_2 condensation in our simulations, which will likely affect the maximum CO_2 limit we found ($\sim$10 bars). As discussed in Chapter 5, at levels of 1-2 bars, CO_2 condensation is likely to occur in the upper atmosphere (Pierrehumbert, 2005). Depending on the particle size of CO_2 ice grains, this could result in cooling of the planet due to the albedo effect of CO_2 ice clouds (Kasting, 1991), or warming by scattering outgoing thermal radiation back towards the surface of the planet (Forget & Pierrehumbert, 1997). Including CO_2 condensation in these simulations is a topic for future work.

Kopparapu *et al.* (2013a; 2013b) found that the maximum CO_2 greenhouse limit is $\sim$7-8 bars for a star with a similar effective temperature to that of Kepler-62 (Kopparapu et al., 2013a,b) compared to our observed 12-bar value. However, they used a 1-D radiative-convective model in their work, and did not include the effect of water clouds or CO_2 clouds in their calculations. While water clouds could increase the planetary albedo, thereby cooling the planet further, they may also contribute to the greenhouse effect, as both H_2O and CO_2 have strong absorption coefficients in the near-IR, which increase the amount of radiation absorbed by planets with lower-mass host stars that emit strongly in the near-IR (Kasting et al., 1993; Selsis et al., 2007; Kopparapu et al., 2013a,b; Joshi & Haberle, 2012; Shields et al., 2013, 2014). Our results with a 3-D GCM do include water clouds, though not CO_2 clouds. As previously mentioned, CO_2 clouds may warm or cool, depending on particle size. However, dense CO_2 atmospheres can be expected to cause more even distributions of heat across a planet, reducing the contrast between maximum and minimum surface temperatures. This is particularly important on synchronously-rotating planets (Joshi et al., 1997; Edson et al., 2011), where the difference in instellation on the day and night sides of the planet is large. We also see this result in our simulations, which show smaller maximum/minimum surface temperature contrasts with larger amounts of CO_2.

The addition of a large eccentricity ($e = 0.32$) into our high-CO_2 simulations also may contribute to the higher CO_2 limit observed here. Planetary habitability throughout the course of an eccentric orbit has been shown to be most strongly affected by the time-averaged global insolation—provided there is an ocean to contribute to the planet's heat capacity—which is greater at higher eccentricities (Williams & Pollard, 2002). Therefore, although high-eccentricity planets may spend significant fractions of an orbit in or outside

of their stars' habitable zones, high eccentricity may help these planets maintain habitable surface conditions over an annual cycle (Kopparapu et al., 2013a,b).

6.3.1 Additional orbital influences on the climate of Kepler-62f

Given that the obliquity, rotation rate, and the VEP for Kepler-62f are unknown, we explored how these factors might influence surface habitability on this planet. Our results indicate that high obliquity, which has been shown to increase seasonality and stability against snowball episodes (Williams & Kasting, 1997; Williams & Pollard, 2003; Spiegel et al., 2009), results in even higher seasonality at high eccentricity, due to the larger difference between the orbital distance at pericenter and apocenter (Williams & Pollard, 2002). This effect is more pronounced in the southern hemisphere during its summer months, when the angle of vernal equinox relative to pericenter is 90°, so that the planet's high obliquity significantly increases the instellation received by this hemisphere. Even on an ice-covered planet, surface temperatures reach above the freezing point of water during southern hemisphere summer months, which could cause surface melting. The VEP can therefore amplify the warming effects of high obliquity and eccentricity, keeping ice from forming at the poles, or reducing an ice sheet formed during the planet's orbit. If the planet experiences large oscillations in obliquity, polar ice could be prevented from forming on both hemispheres over an annual cycle, allowing habitable surface conditions to be maintained on planets with large eccentricities (Armstrong et al., 2014).

Our simulations of a synchronous rotation period for Kepler-62f indicate that much larger cloud cover is likely to form on a planet with an ocean when the incident stellar radiation is focused on its non-varying substellar point, compared to that formed on a planet whose substellar point rotates relative to its host star. This larger amount of cloud cover increases the overall albedo of the planet, resulting in more shortwave radiation reflected back to space. While this cloud feedback has been proposed as a stabilizing mechanism to cool planets near the traditional inner edge of their stars' habitable zones, keeping them habitable at shorter distances from their stars (Yang et al., 2013, 2014), this could adversely affect habitability on planets near the outer edge of the habitable zone like Kepler-62f, by further reducing surface temperatures.

The weaker Coriolis force present on synchronously-rotating planets leads to an advection-dominated dynamics regime governing atmospheric circulation (Showman et al., 2013). Combined with sufficient greenhouse gas concentration levels (Joshi et al., 1997), this may prevent atmospheric freeze out on the night side of the planet, through the transport of high amounts of heat from the day side to the night side, thus reducing horizontal temperature contrasts (Pierrehumbert, 2011). Given that the required CO_2 levels for clement conditions for surface liquid water (1-3 bar) are well within the habitable zone limit for CO_2, a synchronously-rotating Kepler-62f with an active carbon cycle, as well as one with a slow, non-synchronous rotation rate, could have an ample amount of the necessary greenhouse gas concentrations for atmospheric stability and habitable surface conditions.

It should be noted that our high-CO_2 runs with LMDZ had not yet reached full equilibration at the time of writing, therefore we expect there to be adjustments to these results in the future. However, given that we have compared simulations of equal model integration lengths, we expect the general trends we have shown here to be robust.

Chapter 7

CONCLUSIONS

We are living in an era where new planets are discovered almost daily. In the last twenty years, the nature of observed exoplanets has changed significantly, from large, Jupiter-sized planets orbiting extremely close to their stars (Mayor & Queloz, 1995), to worlds similar in size to the Earth (Borucki et al., 2013; Quintana et al., 2014), located in their stars' habitable zones and carrying the potential to sustain liquid water on their surfaces. Here on Earth, where there is water, there is life. Therefore the search for life elsewhere begins with identifying which among the thousands of planets discovered are capable of having and maintaining liquid water on their surfaces. Statistical surveys have demonstrated that small planets are common, especially around smaller, lower-mass stars (Howard et al., 2012). Of these, M-dwarf stars are currently the likeliest hosts for planets similar in size to the Earth (0.5-1.4 $R_{\oplus}$) orbiting in their stars' habitable zones (Dressing & Charbonneau, 2013; Kopparapu, 2013), and frequently as members of multiple-planet systems (Swift et al., 2013). As we move from an era of observational discovery alone to one in which we have numerous, potentially habitable worlds awaiting closer study, we need to understand the interactions between the unique stellar and planetary environments in which these planets reside, and how these interactions could influence a planet's climate and habitability.

In this work I have highlighted key interactions between stars and orbiting planets, and explored their effects on planetary climate and habitability using a hierarchy of models taken from a number of disciplines that I developed and modified. I have shown that these interactions have significant effects on planetary climate and surface habitability, and they should be considered in future modeling efforts.

Given that potentially habitable planets have been found around stars of different stellar types, the interaction between a host star's spectrum and an orbiting planet's atmosphere and surface will affect the manner in which the planet achieves global energy balance, and

its overall climate and habitability. Using 1-D and 3-D climate simulations, we find that planets orbiting cooler, redder stars at equivalent flux distances exhibit higher global mean surface temperatures than planets orbiting stars with more visible and near-UV radiation output (Shields et al., 2013). The increased surface temperatures are in large part due to atmospheric gas absorption of near-IR radiation emitted by M-dwarf stars, which is a much higher percentage of their emitted radiation when compared to stars like our Sun. However, we have shown that the spectral dependence of water ice and snow albedo also plays a role in affecting climate for moderate to low levels of atmospheric CO_2. Changes to planetary climate appear to be less sensitive to M-dwarf SED than G- and F-dwarf SED, as evidenced by the smaller change in ice extent for a given change in stellar flux for M-dwarf planets. M-dwarf planets may therefore be more stable against snowball episodes over the course of their history than planets orbiting hotter, brighter stars. If M-dwarf planets are less likely to enter snowball states, than it might be easier for life to develop and evolve on these planets.

We also explored the effect of stellar SED on a planet's ability to exit out of a snowball state. The results of our 3-D climate simulations, in concert with our previous results for snowball entrance, have demonstrated that the climate stability and evolution of a planet depend on the spectral energy distribution of its host star. M-dwarf planets exhibit climate hysteresis (i.e., multiple possible climate states) over a smaller range of incident stellar radiation than planets orbiting stars with higher visible and near-UV output (Shields et al., 2014). A consequence of small hysteresis is that starting at the coldest state with multiple possible climate states, the tropics melt more readily from increasing instellation. This is due to the combined effects of high near-IR absorption of surface ice and snow and atmospheric greenhouse gases and clouds, and the weaker Hadley circulations, which allow more heat to be retained at the tropics. If a silicate weathering feedback operates, increased CO_2 would further reduce the climate hysteresis on M-dwarf planets with equivalent surface temperatures to G-dwarf planets, providing increased stability against permanent low-latitude glaciation. In short, M-dwarf planets appear harder to freeze, and easier to thaw out of snowball states, due to the large amount of near-IR radiation emitted by these stars. Earth-sized planets orbiting in the habitable zones of lower-mass stars may therefore be the best

candidates for worlds with stable climates conducive to the long-term presence of surface liquid water and perhaps life, and the most important targets for characterization missions such as *TESS*.

Given our results showing greater climate stability for theoretical single planets orbiting lower-mass stars, we demonstrated the widespread application of these methods by applying them to an actual, observed multiple-planet system orbiting a low-mass star —the K-dwarf star Kepler-62—which hosts one of the smallest potentially habitable planets discovered to date: Kepler-62f. We carried out a comprehensive exploration of the orbital evolution of Kepler-62f using an n-body model. The inputs to the n-body model were provided using a method I developed to determine the locations of all planets in a system at the same epoch based on transit timing data. We found that the maximum eccentricity that Kepler-62f could have while maintaining dynamical stability within the system was 0.32 given a wide range of possible locations for pericenter.

At 41% of the modern solar constant, this planet will likely require an active carbonate-silicate cycle (or some other means by which to produce high greenhouse gas concentrations) to maintain clement conditions for surface liquid water. With 3 bars of CO_2 in its atmosphere, 3-D climate simulations of Kepler-62f yielded surface temperatures above the freezing point of water across ∼55-65% of the planetary surface and within the full range of stable eccentricities possible for the planet, $0.0 \leqslant e \leqslant 0.32$. Simulations with just 1 bar of CO_2 also exhibited habitable surface temperatures, though over a smaller area of the planet ($< 35\%$). Given that the required CO_2 levels for surface liquid water are well below the maximum CO_2 greenhouse limit (Kopparapu et al., 2013a,b), they would provide a plausible means of maintaining habitable conditions for surface liquid water on Kepler-62f throughout one million years of orbital evolution.

Assuming that Kepler-62f was synchronously rotating, this reduced the area of open water to a small circular region at the planet's substellar point. This was due to increased cloud cover, which led to a higher planetary albedo and cooler surface temperatures in the synchronous case, as has been seen previously for planets at the inner edge of the habitable zone (Yang et al., 2013). Near the outer edge of the habitable zone, however, synchronous rotation may reduce the amount of habitable surface area on a planet compared

to a planet with a shorter rotation rate, depending on the greenhouse gas concentration and the behavior of the hydrological cycle on distant outer worlds.

We have also shown that surface temperatures above the freezing point of water during an annual cycle are possible on a planet with a low (Earth-like) level of CO_2, provided that the obliquity is high (60°) compared to an Earth-like obliquity (23°), and the summer solstice at a given hemisphere occurs at or near the planet's closest approach to its star. This is a rare but possible orbital configuration that could cause surface melting of an ice sheet, and if a planet undergoes obliquity oscillations, may help prevent its formation (Armstrong et al., 2014).

The n-body model used in this work does not include the effect of tides. With an orbital period of 267 days, tides are likely to be weak on Kepler-62f, but they could affect its rotation period (Heller et al., 2011), and would certainly be an important consideration for potentially habitable planets orbiting even closer to their stars. Tidal effects can lead to changes in orbital parameters, and may induce capture into resonances in spin-orbit period, depending on the planet's eccentricity and its equatorial ellipticity (the equilibrium shape attained as a result of the gravitational interaction between the planet and the host star, Rodríguez et al., 2012). Our work here exploring the extreme case of spin-orbit resonance—synchronous rotation—revealed larger cloud cover than with a rotation period similar to the Earth. This large amount of cloud cover can cool a planet. Non-synchronous resonance configurations, such as the 3:2 spin-orbit resonance observed on the planet Mercury (Goldreich & Peale, 1966; Correia & Laskar, 2004) are also possible, and may be sustained on a planet in a non-circular orbit over long timescales (Rodríguez et al., 2012). Such configurations become more likely at larger orbital eccentricities (Malhotra, 1998; Correia & Laskar, 2004). Additionally, a planet with an oscillating eccentricity due to its companions (Mardling, 2007) can bounce chaotically between spin-orbit resonances (Wisdom et al., 1984), which will significantly change the rotation rate of the planet. Exploring the effect of non-synchronous rotation resonances and variable rotation rate on the climate and habitability of multiple-planet systems is a logical next step.

A number of model assumptions made during the course of this work have implications for the results we have presented here. In particular, the lack of ocean heat transport in

our CCSM4 aqua planet simulations likely resulted in snowball states occurring at smaller decreases in instellation than would have been the case if ocean heat transport were included (Poulsen et al., 2001; Pierrehumbert et al., 2011). Additionally, ocean heat transport has been shown to hasten the retreat of global ice cover on planets orbiting M-dwarf stars (Hu & Yang, 2014). The stable post-snowball ice line latitudes generated in our simulations of thawing M-dwarf planets may be higher than we calculated, given the inclusion of ocean heat transport. Comparing our CCSM4 simulations to those with ocean heat transport included—to see how the snowball transition and stable ice lines are affected—would be a useful task.

All of our simulations assumed an aqua planet configuration, with no (GCM) or a very small fraction of (0.01 in our EBM) land. Previous work exploring the habitability of planets composed almost entirely of land and orbiting G-dwarf stars suggest that due to their lower thermal inertia and drier atmospheres, land planets are less susceptible to snowball episodes than aqua planets, requiring 13% less instellation to freeze over entirely (Abe et al., 2011). In Chapter 3 we showed that given that M-dwarf aqua planets require even less instellation than the G-dwarf land planets of Abe *et al.* (2011) to freeze over (73% vs. 77% of the modern solar constant, respectively, Shields et al., 2013), M-dwarf planets may be less susceptible to snowball episodes than G-dwarf planets, regardless of land percentage. The presence of land could certainly affect the silicate weathering rate and atmospheric concentration of CO_2 on a planet. However, Abbot *et al.* (2012) found that climate weathering feedback does not have a strong dependence on land fraction, as long as the land fraction is at least 0.01.

Edson *et al.* (2012) found that the amount of CO_2 that accumulates in the atmosphere of a synchronously-rotating planet could be much greater if the substellar point is located over an ocean-covered area of the planet, where continental weathering is minimal, although atmospheric CO_2 concentration could still be limited by seafloor weathering processes (Edson et al., 2012). Including land in future simulations of a synchronously-rotating Kepler-62f, using a GCM with a carbonate-silicate cycle included (rather than assigning a prescribed atmospheric CO_2 concentration as we have done here) would be a valuable step towards assessing the role of surface type in regulating atmospheric CO_2 inventory on synchronously-

rotating planets. Additionally, exploring the affect of the interaction between stellar SED and surface land albedo, which exhibits unique wavelength-dependent properties (Shields et al., 2013) that could have implications for the climate of planets orbiting different types of stars, is also important future work.

I have explored the influence on climate of the interaction between different types of stars and their orbiting planets, and demonstrated that these unique stellar and planetary interactions have important implications for habitability. The techniques presented here can be applied to planets orbiting stars of any spectral type, with a range of possible atmospheric and surface compositions and dynamical architectures. They can be used to help assess the potential habitability of newly discovered planets for which observational measurements are still limited, and can be easily modified to incorporate new observational data that are acquired for these planets in the future.

BIBLIOGRAPHY

Abbot, D. S., Cowan, N. B., & Ciesla, F. J. 2012, Astroph. J., 756, 178

Abbot, D. S., & Pierrehumbert, R. T. 2010, Journal of Geophysical Research: Atmospheres, 115, D03104

Abbot, D. S. G., Voigt, A., & Koll, D. 2011, J. Geophys. Res., 116, D18103

Abe, Y., Abe-Ouchi, A., Sleep, N. H., & Zahnle, K. J. 2011, Astrobiology, 11, 443

Anglada-Escudé, G., Tuomi, M., Gerlach, E., et al. 2013, A&A, 556, A126

Armstrong, J. C., Barnes, R., Domagal-Goldman, S., et al. 2014, Astrobiology, 14, 277

Bao, H., Fairchild, I. J., Wynn, P. M., & Spˆtl, C. 2009, Science, 323, 119

Barkstrom, B. R., & Hall, J. B. 1982, Journal of Energy, 2, 141

Barnes, R., Jackson, B., Greenberg, R., & Raymond, S. N. 2009, ApJ, 700, L30

Barnes, R., Mullins, K., Goldblatt, C., et al. 2013, Astrobiology, 13, 225

Barnes, R., Raymond, S. N., Jackson, B., & Greenberg, R. 2008, Astrobiology, 8, 557

Batalha, N. M., Borucki, W. J., Bryson, S. T., et al. 2011, Astroph. J., 729, 27

Beaulieu, J.-P., Bennett, D. P., Fouqué, P., et al. 2006, Nature, 439, 437

Berger, A., Gallée, H., Fichefet, T., Marsiat, I., & Tricot, C. 1990, Global and Planetary Change, 3, 125

Berger, A., Loutre, M. F., & Mélice, J. L. 2006, Climate of the Past, 2, 131

Berger, A., Loutre, M.-F., & Tricot, C. 1993, J. Geophys. Res., 98, 10341

Bitz, C. M., Shell, K. M., Gent, P. R., et al. 2012, Journal of Climate, 25, 3053

Bochanski, J. J., Hawley, S. L., Covey, K. R., et al. 2010, Astron. J., 139, 2679

Borucki, W. J., & Summers, A. L. 1984, Icarus, 58, 121

Borucki, W. J., Koch, D., Basri, G., et al. 2006, ISSI Scientific Reports Series, 6, 207

Borucki, W. J., Agol, E., Fressin, F., et al. 2013, Science, 340, 587

Bougher, S. W., Hunten, D. M., & Phillips, R. J., eds. 1997, Venus II

Brandt, R. E., Warren, S. G., Worby, A. P., & Grenfell, T. C. 2005, Journal of Climate, 18, 3606

Briegleb, B. P. 1992, Journal of Geophysical Research: Atmospheres, 97, 7603

Budyko, M. I. 1969, Tellus, 21, 611

Carter, J. A., Agol, E., Chaplin, W. J., et al. 2012, Science, 337, 556

Chance, K., & Kurucz, R. L. 2010, J. Quant. Spec. Radiat. Transf., 111, 1289

Cogley, J. G., & Henderson-Sellers, A. 1984, Monthly weather review, 112, 1017

Correia, A. C. M., Boué, G., & Laskar, J. 2012, ApJ, 744, L23

Correia, A. C. M., & Laskar, J. 2004, Nature, 429, 848

Crisp, D. 1997, Geophys. Res. Lett., 24, 571

Danby, J. M. A., & Burkardt, T. M. 1983, Celestial Mechanics, 31, 95

Des Marais, D. J., Nuth, III., J. A., Allamandola, L. J., et al. 2008, Astrobiology, 8, 715

Dole, S. H. 1964, Habitable Planets for Man (Blaisdell, New York.)

Dressing, C. D., & Charbonneau, D. 2013, Astroph. J., 767, 95

Dressing, C. D., Spiegel, D. S., Scharf, C. A., Menou, K., & Raymond, S. N. 2010, Astroph. J., 721, 1295

Driscoll, P., & Bercovici, D. 2013, Icarus, 226, 1447

Dumusque, X., Bonomo, A. S., Haywood, R. D., et al. 2014, ArXiv e-prints, arXiv:1405.7881

Dunkle, R. V., & Bevans, J. T. 1956, Journal of Meteorology, 13, 212

Edson, A., Lee, S., Bannon, P., Kasting, J. F., & Pollard, D. 2011, Icarus, 212, 1

Edson, A. R., Kasting, J. F., Pollard, D., Lee, S., & Bannon, P. R. 2012, Astrobiology, 12, 562

Farrell, E. F., & Newnham, R. E. 1967, The American Mineralogist, 52, 380

Feulner, G. 2012, Reviews of Geophysics, 50, 2006

Flato, G., Marotzke, J., Abiodun, B., et al. 2013, in Climate Change 2013: The Physical Science Basis. Contribution of Working Group I to the Fifth Assessment Report of the Intergovernmental Panel on Climate Change, ed. T. F. Stocker, D. Qin, G. K. Plattner, M. Tignor, S. K. Allen, J. Boschung, A. Nauels, Y. Xia, V. Bex, & P. M. Midgley (Cambridge University Press), 741–866

Forget, F., & Pierrehumbert, R. T. 1997, Science, 278, 1273

Forget, F., Wordsworth, R., Millour, E., et al. 2013, Icarus, 222, 81

Gent, P. R., Danabasoglu, G., Donner, L. J., et al. 2011, Journal of Climate, 24, 4973

Goldreich, P., & Peale, S. 1966, Astron. J., 71, 425

Goody, R. M., & Yung, Y. L. 1995, Atmospheric Radiation, A Theoretical Basis (Oxford University Press), 46

Gough, D. O. 1981, Sol. Phys., 74, 21

Grenfell, T. C. 2011, in Encyclopedia of Snow and Ice Glaciers, ed. V. P. Singh, P. Singh, & U. K. Haritashya, Vol. XLVI (Springer), 23–35

Grenfell, T. C., Warren, S. G., & Mullen, P. C. 1994, J. Geophys. Res., 99, 18669

Guo, J., Zhang, F., Chen, X., & Han, Z. 2009, Ap&SS, 323, 367

Hart, M. H. 1979, Icarus, 37, 351

Hartmann, H. 1994, Global Physical Climatology (Academic Press), 11

Hatzes, A. P., Fridlund, M., Nachmani, G., et al. 2011, Astroph. J., 743, 75

Hawley, S. L., & Pettersen, B. R. 1991, Astroph. J., 378, 725

Hays, J. D., Imbrie, J., & Shackleton, N. J. 1976, Science, 194, 1121

Heller, R., Barnes, R., & Leconte, J. 2011, Origins of Life and Evolution of the Biosphere, 41, 539

Heng, K., & Kopparla, P. 2012, Astroph. J., 754, 60

Hoehler, T. M. 2007, Astrobiology, 7, 824

Hoffman, P. F., Kaufman, A. J., Halverson, G. P., & Schrag, D. P. 1998, Science, 281, 1342

Hoffman, P. F., & Li, Z.-X. 2009, Palaeogeography, Palaeoclimatology, Palaeoecology, 277, 158

Hoffman, P. F., & Schrag, D. P. 2002, Terra Nova, 14, 129

Holton, J. R. 2004, An Introduction to Dynamic Meteorology (Academic Press), 456

Hourdin, F., Musat, I., Bony, S., et al. 2006, Climate Dynamics, 27, 787

Howard, A. W., Marcy, G. W., Bryson, S. T., et al. 2012, Astroph. J. Suppl., 201, 15

Hu, Y., & Yang, J. 2014, Proceedings of the National Academy of Sciences, 111, 629

Hu, Y., Yang, J., Ding, F., & Peltier, W. R. 2011, Climate of the Past, 7, 17

Hunke, E. C., & Lipscomb, W. H. 2008, CICE: The Los Alamos Sea Ice Model. Documentation and Software User's Manual. Version 4.0. (T-3 Fluid Dynamics Group, Los Alamos National Laboratory, Tech. Rep. LA-CC-06-012.)

Hunt, B. G. 1982, Journal of the Meteorological Society of Japan. Ser. II, 60, 309

Iben, Jr., I. 1967, ARA&A, 5, 571

Ingersoll, A. P. 1969, Journal of Atmospheric Sciences, 26, 1191

Jenkins, G. S. 2000, J. Geophys. Res., 105, 7357

Joseph, J. H., Wiscombe, W. J., & Weinman, J. A. 1976, Journal of Atmospheric Sciences, 33, 2452

Joshi, M. M., & Haberle, R. M. 2012, Astrobiology, 12, 3

Joshi, M. M., Haberle, R. M., & Reynolds, R. T. 1997, Icarus, 129, 450

Kaltenegger, L., Sasselov, D., & Rugheimer, S. 2013, ApJ, 775, L47

Kane, S. R., & Gelino, D. M. 2012, PASP, 124, 323

Kasting, J. F. 1988, Icarus, 74, 472

—. 1991, Icarus, 94, 1

Kasting, J. F., & Ackerman, T. P. 1986, Science, 234, 1383

Kasting, J. F., Whitmire, D. P., & Reynolds, R. T. 1993, Icarus, 101, 108

Kiehl, J. T., & Trenberth, K. E. 1997, Bull. Amer. Meteor. Soc., 78, 197

Kirschvink, J. 1992, Late Proterozoic Low-Latitude Global Glaciation: the Snowball Earth, ed. J. Schopf, Vol. The Proterozoic Biosphere: A Multidisciplinary Study (Cambridge University Press), 51–52

Kopparapu, R. K. 2013, ApJ, 767, L8

Kopparapu, R. K., Ramirez, R. M., SchottelKotte, J., et al. 2014, ApJ, 787, L29

Kopparapu, R. K., Ramirez, R., Kasting, J. F., et al. 2013a, Astroph. J., 770, 82

—. 2013b, Astroph. J., 765, 131

Kukla, G. 1979, Sea Level, Ice, and Climatic Change (Proceedings of the Canberra Symposium), 131, 79

Kushner, D. 1981, in Comets and the Origin of Life, ed. C. Ponnamperuma, 241–248

Laughlin, G., Bodenheimer, P., & Adams, F. C. 1997, Astroph. J., 482, 420

Le Hir, G., Donnadieu, Y., Krinner, G., & Ramstein, G. 2010, Climate Dynamics, 35, 285

Le Hir, G., Ramstein, G., Donnadieu, Y., & GoddÈris, Y. 2008, Geology, 36, 47

Leconte, J., Forget, F., Charnay, B., et al. 2013, A&A, 554, A69

Lewis, J. P., Weaver, A. J., & Eby, M. 2006, Geophys. Res. Lett., 33, doi:10.1029/2006GL027774

Lindzen, R. S., & Farrell, B. 1977, Journal of Atmospheric Science, 34, 1487

Lissauer, J. J., Marcy, G. W., Rowe, J. F., et al. 2012, Astroph. J., 750, 112

Lissauer, J. J., Marcy, G. W., Bryson, S. T., et al. 2014, Astroph. J., 784, 44

Lopez, E. D., & Fortney, J. J. 2013, ArXiv e-prints, arXiv:1311.0329

Malhotra, R. 1998, in Astronomical Society of the Pacific Conference Series, Vol. 149, Solar System Formation and Evolution, ed. D. Lazzaro, R. Vieira Martins, S. Ferraz-Mello, & J. Fernandez, 37

Marcy, G. W., Butler, R. P., Williams, E., et al. 1997, Astroph. J., 481, 926

Marcy, G. W., Isaacson, H., Howard, A. W., et al. 2014, Astroph. J. Suppl., 210, 20

Mardling, R. A. 2007, MNRAS, 382, 1768

Mayor, M., & Queloz, D. 1995, Nature, 378, 355

Mazur, P. 1980, Origins of Life, 10, 137

McGuffie, K., & Henderson-Sellers, A. 2005, A History of and Introduction to Climate Models (John Wiley and Sons, Ltd), 47–79

McKay, C. P. 1991, Icarus, 91, 93

Meadows, V. S., & Crisp, D. 1996, Journal of Geophysical Research (Planets), 101, 4595

Merlis, T. M., & Schneider, T. 2010, Journal of Advances in Modeling Earth Systems, 2, 1

Mernild, S. H., Liston, G. E., Hiemstra, C. A., & Christensen, J. H. 2010, Journal of Hydrometeorology, 11, 3

Muirhead, P. S., Johnson, J. A., Apps, K., et al. 2012, Astroph. J., 747, 144

Murray, C. D., & Dermott, S. F. 2000, Solar System Dynamics (Cambridge University Press)

Newman, M. J., & Rood, R. T. 1977, Science, 198, 1035

North, G. R., & Coakley, J. A. 1979, Journal of the Atmospheric Sciences, 36, 1189

Oreopoulos, L., & Khairoutdinov, M. 2003, Journal of Geohpysical Research, 108, 4479

Parkinson, W. H., Rufus, J., & Yohino, K. 2003, Chemical Physics, 290, 251

Pickles, A. J. 1998, PASP, 110, 863

Pierrehumbert, R. 2005, Journal of Geophysical Research: Atmospheres, 110, 2156

—. 2010, Principles of Planetary Climate (Cambridge University Press)

Pierrehumbert, R. T. 2004, Nature, 429, 646

Pierrehumbert, R. T. 2011, ApJ, 726, L8

Pierrehumbert, R. T., Abbot, D. S., Voigt, A., & Koll, D. 2011, Annual Review of Earth and Planetary Sciences, 39, 417

Planavsky, N. J., Rouxel, O. J., Bekker, A., et al. 2010, Nature, 467, 1088

Pollard, D., & Kasting, J. F. 2005, Journal of Geohpysical Research, 110

Poulsen, C. J., Pierrehumbert, R. T., & Jacob, R. L. 2001, Geophys. Res. Lett., 28, 1575

Quintana, E. V., Barclay, T., Raymond, S. N., et al. 2014, Science, 344, 277

Rauch, K. P., & Hamilton, D. P. 2002, in Bulletin of the American Astronomical Society, Vol. 34, AAS/Division of Dynamical Astronomy Meeting #33, 938

Reid, I. N., Hawley, S. L., & Gizis, J. E. 1995, Astron. J., 110, 1838

Ricker, G. R., Latham, D. W., Vanderspek, R. K., et al. 2009, in Bulletin of the American Astronomical Society, Vol. 41, American Astronomical Society Meeting Abstracts No. 213, 403.01

Ricker, G. R., Winn, J. N., Vanderspek, R., et al. 2014, ArXiv e-prints, arXiv:1406.0151

Robinson, T. D., Meadows, V. S., Crisp, D., et al. 2011, Astrobiology, 11, 393

Rodríguez, A., Callegari, N., Michtchenko, T. A., & Hussmann, H. 2012, MNRAS, 427, 2239

Rothman, L. S., Gordon, I. E., Barbe, A., et al. 2009, Journal of Quantitative Spectroscopy and Radiative Transfer, 110, 533

Rowe, J. F., Bryson, S. T., Marcy, G. W., et al. 2014, Astroph. J., 784, 45

Sackmann, I.-J., Boothroyd, A. I., & Kraemer, K. E. 1993, Astroph. J., 418, 457

Sagan, C., & Mullen, G. 1972, Science, 177, 52

Segelstein, D. 1981, Master's thesis, University of Missouri-Kansas City, Department of Physics

Segura, A., Kasting, J. F., Meadows, V., et al. 2005, Astrobiology, 5, 706

Segura, A., Krelove, K., Kasting, J. F., et al. 2003, Astrobiology, 3, 689

Segura, A., Walkowicz, L. M., Meadows, V., Kasting, J., & Hawley, S. 2010, Astrobiology, 10, 751

Seiff, A. 1987, Advances in Space Research, 7, 323

Sellers, W. D. 1969, Journal of Applied Meteorology, 8, 392

Selsis, F., Kasting, J. F., Levrard, B., et al. 2007, A&A, 476, 1373

Shields, A. L., Bitz, C. M., Meadows, V. S., Joshi, M. M., & Robinson, T. D. 2014, ApJ, 785, L9

Shields, A. L., Meadows, V. S., Bitz, C. M., et al. 2013, Astrobiology, 13, 715

Showman, A. P., Cho, J. Y.-K., & Menou, K. 2011, Atmospheric Circulation of Exoplanets, ed. S. Seager, 471–516

Showman, A. P., & Polvani, L. M. 2011, Astroph. J., 738, 71

Showman, A. P., Wordsworth, R. D., Merlis, T. M., & Kaspi, Y. 2013, Atmospheric Circulation of Terrestrial Exoplanets, ed. S. J. Mackwell, A. A. Simon-Miller, J. W. Harder, & M. A. Bullock, 277–326

Spiegel, D. S., Menou, K., & Scharf, C. A. 2009, Astroph. J., 691, 596

Spiegel, D. S., Raymond, S. N., Dressing, C. D., Scharf, C. A., & Mitchell, J. L. 2010, Astroph. J., 721, 1308

Stamnes, K., Tsay, S.-C., Jayaweera, K., & Wiscombe, W. 1988, Appl. Opt., 27, 2502

Sudarsky, D., Burrows, A., Hubeny, I., & Li, A. 2005, Astroph. J., 627, 520

Swift, J. J., Johnson, J. A., Morton, T. D., et al. 2013, Astroph. J., 764, 105

Tajika, E. 2008, ApJ, 680, L53

Tarter, J. C., Backus, P. R., Mancinelli, R. L., et al. 2007, Astrobiology, 7, 30

Thornthwaite, C. W. 1948, Geographical Review, 38, pp. 55

Toon, O. B., McKay, C. P., Ackerman, T. P., & Santhanam, K. 1989, J. Geophys. Res., 94, 16287

Underwood, D. R., Jones, B. W., & Sleep, P. N. 2003, International Journal of Astrobiology, 2, 289

Vogt, S. S., Butler, R. P., Rivera, E. J., et al. 2010, Astroph. J., 723, 954

Walker, J. C. G., Hays, P. B., & Kasting, J. F. 1981, J. Geophys. Res., 86, 9776

Ward, W. R. 1974, J. Geophys. Res., 79, 3375

Warren, S. G., Brandt, R. E., Grenfell, T. C., & McKay, C. P. 2002, Journal of Geophysical Research, 107, 3167

Warren, S. G., & Hahn, C. J. 2002, Encyclopedia of Atmospheric Sciences, 476

Weiss, L. M., & Marcy, G. W. 2014, ApJ, 783, L6

Williams, D. M., & Kasting, J. F. 1997, Icarus, 129, 254

Williams, D. M., & Pollard, D. 2002, International Journal of Astrobiology, 1, 61

—. 2003, International Journal of Astrobiology, 2, 1

Williams, G. E. 1975, Geological Magazine, 112, 441

Williams, G. P. 1988, Climate Dynamics, 3, 45

Wiscombe, W. J., & Warren, S. G. 1980, Journal of Atmospheric Sciences, 37, 2712

Wisdom, J., & Holman, M. 1991, Astron. J., 102, 1528

Wisdom, J., Peale, S. J., & Mignard, F. 1984, Icarus, 58, 137

Wordsworth, R., Forget, F., & Eymet, V. 2010, Icarus, 210, 992

Wordsworth, R., Forget, F., Millour, E., et al. 2013, Icarus, 222, 1

Wordsworth, R. D., Forget, F., Selsis, F., et al. 2011, ApJ, 733, L48

Wright, J. T., Fakhouri, O., Marcy, G. W., et al. 2011, PASP, 123, 412

Yang, J., Boué, G., Fabrycky, D. C., & Abbot, D. S. 2014, ApJ, 787, L2

Yang, J., Cowan, N. B., & Abbot, D. S. 2013, ApJ, 771, L45

Zsom, A., Kaltenegger, L., & Goldblatt, C. 2012, Icarus, 221, 603

VITA

Aomawa L. Shields

Education

- Ph.D. in Astronomy and Astrobiology, University of Washington (UW) (2014)
- M.Sc. in Astronomy, UW (2011)
- MFA in Acting, University of California, Los Angeles (UCLA) (2001)
- Sc.B. in Earth, Atmospheric and Planetary Sciences, Massachusetts Institute of Technology (MIT) (1997)
- Graduated with High Honors from Phillips Exeter Academy (1993)

Fellowships

- National Science Foundation (NSF) Astronomy and Astrophysics Postdoctoral Fellowship (2014-2017)
- UC President's Postdoctoral Program Fellowship (2014-2015)
- NSF Graduate Research Fellowship (2011-2014)
- NSF Integrative Graduate Education and Research Traineeship (2009-2011)

Honors and Awards

- First Place, Astrobiology Science Conference Student Poster Competition (2012)
- "Audience Choice", US FameLab Astrobiology communication competition (2012)
- Member, Minorities Striving and Pursuing Higher Degrees of Success in Earth System Science Professional Development Program (MS PHD'S PDP) (2011-2013)

- National Aeronautics and Space Administration (NASA) Group Achievement Award, Spitzer Science Operations Planning Team (2010)

- NASA Public Service Group Achievement Award, Spitzer Observatory Planning/Scheduling Team (2009)

Teaching

- Guest Lecturer, ESS 495 "NASA Space Grant Seminar: Rocks-n-Stars", undergraduate lecture entitled "Searching for Life Around Red Dwarf Stars" (2014)

- Guest Lecturer, Engage: The Science Speaker Seminar, graduate lecture entitled "Communicating Science to the Public" (2014)

- Guest Lecturer, Engage: The Science Speaker Seminar, graduate lecture entitled "Theater improvisation, science communication, and FameLab" (2013)

- Teaching Assistant, ASTR 102 "Astronomy" (2011)

- Teaching Assistant, ASTR 101 "Astronomy" (2011)

- Teaching Assistant, ASTR 150 "The Planets" (2010)

- Guest Teacher, two-day workshop on communicating science to the public for California Institute of Technology's Young Engineering and Science Scholars (YESS) program (2007)

Service

- Reviewer for NSF, March 2013

Public Outreach

- *Pacific Science Center/KCTS 9 Science Cafe* presentation at local pub, "Searching for Life Around Red Dwarf Stars" (2014)

- Keynote speaker, "Women Fly!" event at Museum of Flight, presentation entitled "How I Became an Astronomer and Astrobiologist" (2014)

- Featured scientist, Boston Children's Museum traveling exhibit "My Sky" (2014)

- Facilitator, Astronomy and Astrobiology daylong workshop for girls in YWCA program "Girls Without Limits" in Olympia, WA (2013)

- Lakewood High School, "Ice and Climate on Extrasolar Planets" (2013)
- Astronomy Panel, GeekGirlCon, Seattle, WA (2014)
- Participant, job shadow program, Burlington-Edison High school (2013)
- Fab Fems registered role model (2013-Present)
- American Astronomical Society Astronomy Ambassadors Program (2012-Present)
- Planetarium Lecturer, UW (2011-2014)

Press/Media/Television

- "A Warmer Planetary Haven Around Cool Stars, as Ice Warms Rather Than Cools", University of Washington News Release, July 18, 2013
- Guest Scientist, "Sci-Trek: Volcanoes", The Discovery Channel (2009)
- Guest Scientist, "Universe", The History Channel (2007)
- TV Host and Field Reporter, "Wired Science", PBS (2007)

Refereed Publications

- **Shields, A. L.**, Meadows, V. S., Bitz, C. M., Pierrehumbert, R. T., Joshi, M. M., Robinson, T. D. The Effect of Host Star Spectral Energy Distribution and Ice-Albedo Feedback on the Climate of Extrasolar Planets, *Astrobiology*, 13, 8.
- **Shields, A. L.**, Bitz, C. M., Meadows, V. S., Joshi, M. M., Robinson, T. D. Spectrum-driven Planetary Deglaciation Due to Increases in Stellar Luminosity, *ApJ Letters*, 785, 9.
- Cowan, N. B., Robinson, T., Livengood, T. A., Deming, D., Agol, E., A'Hearn, M. F., Charbonneau, D., Lisse, C. M., Meadows, V. S., Seager, S., **Shields, A. L.**, Wellnitz, D. D. Rotational Variability of Earth's Polar Regions: Implications for Detecting Snowball Planets, *ApJ*, 731, 76.
- Hunter, D. A., Elmegreen, B. G., **Baker, A. L.** The Relationship between Gas, Stars, and Star Formation in Irregular Galaxies: A Test of Simple Models, *ApJ*, 493, 595.

Conference Publications (Oral)

- **Shields, A. L.**, Bitz, C. M., Meadows, V. S., Joshi, M. M., Robinson, T. D. "Climate Hysteresis for Planets Orbiting Stars of Different Spectral Type." Division for Planetary Scienes, Denver, CO, October 2013

- **Shields, A. L.**, Meadows, V. S., Bitz, C. M., Pierrehumbert, R. T., Joshi, M. M., Robinson, T. D. "The Effect of Host Star Spectral Energy Distribution and Ice-Albedo Feedback on the Climate of Extrasolar Planets." American Astronomical Society Winter Meeting, January 2013

- **Shields, A. L.**, Meadows, V. S., Bitz, C. M., Pierrehumbert, R. T., Joshi, M. M., Robinson, T. D. "The Effect of Host Star Spectral Energy Distribution and Ice-Albedo Feedback on the Climate of Extrasolar Planets." Astrobiology Graduate Student Conference, Pasadena, CA, August 2012

Conference Publications (Poster)

- **Shields, A. L.**, Bitz, C. M., Meadows, V. S., Joshi, M. M., Robinson, T. D. "Spectrum-driven Planetary Deglaciation Due to Increases in Stellar Luminosity." Exoclimes III, Davos, Switzerland, February 2014

- **Shields, A. L.**, Meadows, V. S., Bitz, C. M., Pierrehumbert, R. T., Joshi, M. M., Robinson, T. D. "The Effect of Host Star Spectral Energy Distribution on Ice Line Latitude in Terrestrial Exoplanetary Systems." Astrobiology Science Conference, Atlanta, GA, April 2012

- **Shields, A. L.**, Abbey, W., Vance, S. "The Effect of Temperature on Fatty Acid Vesicle Formation in Simulated Deep-ocean Conditions." American Geophysical Union, San Francisco, CA, December 2011

- **Shields, A. L.**., Meadows, V. S., Robinson, T., Crisp, D., Deming, D., A'Hearn, M. F., Charbonneau, D., Livengood, T. A., Seager, S., Barry, R. K., Hearty, T., Hewagama, T., Lisse, C. M., McFadden, L., Wellnitz, D. D., EPOXI Earthling Team. "Earth as an Extrasolar Planet: Comparing Polar and Equatorial Views of Modern Day and Snowball Earth." American Astronomical Society Winter Meeting, January 2011

- Scire, E., Chan, B. H. P., Silbermann, N., **Shields, A. L.**. "The Spitzer Bibliography Database: bibliographic statistics." SPIE, San Diego, CA, June 2010

- **Shields, A. L.**., Meadows, V. S., Robinson, T. D., Deming, L. D., A'Hearn, M. F., Charbonneau, D., Hewagama, T., Lisse, C., Livengood, T., McFadden,

L., Seager, S., Welnitz, D. D., EPOXI Earthling Team. "Earth as an Extrasolar Planet: Comparing Polar and Equatorial Views." Astrobiology Science Conference, Houston, TX, April 2010

- **Shields, A. L.**., Nolan, M. C. "Impact Simulations into Ice on Europa." American Astronomical Society Winter Meeting, January 1996

Invited Talks

- "Searching for Life Around Red Dwarf Stars", Panorama Retirement Center, Lacey, WA, June 2014

- "The Effect of Host Star Spectral Energy Distribution and Ice-Albedo Feedback on the Climate of Extrasolar Planets", University of East Anglia, Norwich, UK, February 2014

- "The Effect of Host Star Spectral Energy Distribution and Ice-Albedo Feedback on Planetary Climate", Solar, Stellar, and Planetary Sciences (SSP) seminar, Harvard-Smithsonian Center for Astrophysics, Cambridge, MA, November 2013

- 'The Effect of Host Star Spectral Energy Distribution and Ice-Albedo Feedback on the Climate of Extrasolar Planets", American Association of Physics Teachers Summer Meeting, Portland, OR, July 2013

- "A Career in Astronomy", Career Exploration Workshop, Making Connections Program, UW, Seattle, WA, April 2013.

Academic Seminars

- "The Effect of Host Star Spectrum on Planetary Climate", presentation to NASA Astrobiology Institute's Executive Council, UW, February 2014

- "The Effect of Host Star Spectral Energy Distribution and Ice-Albedo Feedback on the Climate of Extrasolar Planets", Planetary Science seminar, Jet Propulsion Laboratory, Pasadena, CA, November 2013

- "The Runaway Greenhouse", general exam, UW, November 2012

- "The Effect of Host Star Spectral Energy Distribution and Ice-Albedo Feedback on the Climate of Extrasolar Planets", UW Astrobiology Program student orientation talk, UW, September 2012

- "Ownership, Ethics, and Ice", UW Astrobiology In-House Seminar, UW, February 2012

- "Constraining the Effect of Temperature on Fatty Acid Vesicle Formation in Simulated Deep-ocean Conditions", UW Astrobiology Program research rotation talk, November 2011